UNIVERSITY OF CALIFORNIA SAN DIEGO

From Greenland Fjords to the Labrador Sea: Mechanisms of Heat and Freshwater Transport in Mesoscale Eddy Active Ocean/Sea-ice Simulations

A dissertation submitted in partial satisfaction of the
requirements for the degree Doctor of Philosophy

in

Oceanography

by

Theresa Jayne Morrison

Committee in charge:

Julie McClean, Chair
Sarah Gille, Co-Chair
Ian Eisenman
Graham Elliott
Mathew Maltrud

2022

The Dissertation of Theresa Jayne Morrison is approved, and it is acceptable in quality and form for publication on microfilm and electronically.

University of California San Diego

2022

DEDICATION

For the yaks.

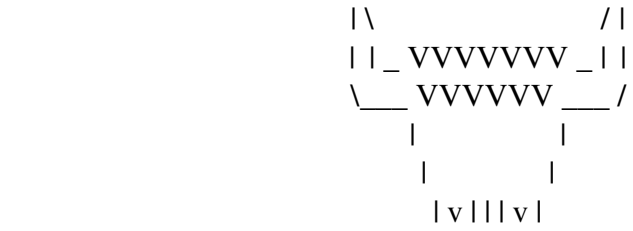

EPIGRAPH

They burnt up a lot of computing time.
Essentially, they showed that there were eddies,
which we knew anyway.

– Klaus Hasselmann, 2021 Nobel Laureate,
in an interview on February 15, 2006.

TABLE OF CONTENTS

LIST OF FIGURES

LIST OF TABLES

ACKNOWLEDGEMENTS

Writing this thesis was only possible with the immeasurable support of my friends and therapist.

I would like to acknowledge the 2016 Physical Oceanography and Climate Science Cohort (AKA "The Yak Pen"): Margaret Lindeman, Jessica Ng, Mike Kovatch, Mike Sierks, Will Chapman, Luke Kachelein, Ratnaksha Lele, and Jacob Morgan. The all the fun times in our shared office and the hours at the chalk board got me through our first year. Thanks also to Katherine Nesbit for all the times she made me dinner and listened. Thanks to the community of students at SIO who were great people to share this daunting process with.

Thanks to Lauren Bobzin and Carl Cordero for sticking with me through the ups and downs. I appreciate the support of my sisters, Sara and Elaine, for their guidance and book recommendations. Thanks to my Uncle Mike for all my desert retreats. Thanks to Margaret, for just about everything.

I would also like to thank André Palóczy for being a great office-mate. Thanks to Robert Sanchez and Donald Slater for always being willing to chat with me about Fjord Box Models.

Chapter 1, in full, has been submitted for publication of the material as it may appear in Journal of Geophysical Research: Oceans, 2022, Morrison, Theresa; Dukhovskoy, Dmitry; McClean, Julie; Gille, Sarah; Chassignet, Eric. The dissertation author was the primary investigator and author of this paper.

Chapter 2, in part is currently being prepared for submission for publication of the material. Morrison, Theresa; McClean, Julie; Gille, Sarah; Maltrud, Mathew; Ivanova, Detelina. The dissertation author was the primary investigator and author of this paper.

Chapter 3, is coauthored with Bryan, Frank; McClean, Julie; Gille, Sarah; Marques, Gustavo. The dissertation author was the primary author of this chapter.

VITA

2016	Bachelor of Science, San Diego State University
2018	Graduate Visitor via the Advanced Study Program at the National Center for Atmospheric Research
2019-2020	Department of Energy Office of Science Graduate Student Research (SCGSR) Program Fellow at Los Alamos National Laboratory
Fall 2021	Teaching Assistant, University of California San Diego
Fall 2022	Doctorate of Philosophy, University of California San Diego

ABSTRACT OF THE DISSERTATION

From Greenland Fjords to the Labrador Sea: Mechanisms of Heat and Freshwater Transport in Mesoscale Eddy Active Ocean/Sea-ice Simulations

by

Theresa Jayne Morrison

Doctor of Philosophy in Oceanography

University of California San Diego, 2022

Julie McClean, Chair
Sarah Gille, Co-Chair

The increased presence of warm Atlantic water on the Greenland continental shelf and within glacial fjords has been connected to the accelerated melting of the Greenland Ice Sheet, particularly in the southwest and southeast continental shelf regions. Meltwater is transported into the Labrador Sea where it may disrupt deep convection, a process that has been linked to the variability of the Atlantic Meridional Overturning Circulation (AMOC). To study the transport of heat onto the continental shelf and freshwater into the Labrador Sea, we use coupled ocean/sea-ice simulations with horizontal resolutions that permit or resolve mesoscale eddies.

We compare the on shelf transport of heat in two mesoscale eddy-permitting simulations.

In both simulations, the region of greatest heat flux onto the shelf is southeast Greenland and south of the Denmark strait, where there is a seasonally persistent pattern of multi-day variability in the cross-shelf heat flux. This high-frequency variability is associated with Denmark Strait Overflow eddies propagating along the shelfbreak.

Using mesoscale eddy-resolving simulations to compare the off-shelf transport of meltwater and impacts on the West Greenland Current, we find that vertically distributed meltwater results in an increase in total freshwater flux into the Labrador Sea. Eddy kinetic energy and baroclinic conversion in the West Greenland Current along the continental shelf break also increase with the addition of vertically distributed meltwater.

Finally, we derive and test a box model to represent the mixing within fjords. This Fjord Box Model merges buoyant plume theory with the estuarine mixing that occurs along fjords. The Fjord Box Model provides a more realistic boundary condition for meltwater forcing in ocean models that cannot resolve fjords.

Introduction

Mass loss of the Greenland Ice Sheet (GIS) has accelerated from relative stability in the early nineties with an estimated loss of 3,902$\pm$342 billion tonnes of ice occurring from 1992-2018 (The IMBIE Team, 2020). This mass loss has resulted in 10.8$\pm$0.9 millimetres of global mean sea level rise (SLR). The GIS is projected to be the major contributor to SLR over the next century, despite the large uncertainty in these estimates (Pattyn et al., 2018; Meehl et al., 2007). Mass loss is roughly equally partitioned between changes to the surface mass balance (accumulation and melting) and dynamic ice loss (solid ice discharge) (The IMBIE Team, 2020). Freshwater enters the ocean as liquid runoff, via submarine melting or iceberg calving. Representing these fluxes in ocean models is essential for realistic projections of the changing circulation of the Subpolar North Atlantic (SPNA) Ocean. In this thesis, we explore the mechanisms governing heat flux onto and freshwater flux off of the continental shelf around Greenland and an improved method for representing meltwater fluxes from the GIS. This work contributes to our understanding of the ocean's role in driving further melting and the impacts of increasing meltwater on the circulation of the SPNA.

Warm water from the Subtropical Atlantic Ocean is the primary source of oceanic heat that drives the melting of the GIS. The southeast portion of the GIS is especially vulnerable to ocean driven melting because of the many tidewater glaciers in Greenland fjords and the Atlantic-originated water that intrudes onto the Greenland continental shelf (Millan et al., 2018; Slater et al., 2022). Glacial fjords are long (50-100 km), narrow (5-10 km), and deep (100s m) estuaries that connect the ocean and the ice sheet (Straneo and Cenedese, 2015a; Carroll et al., 2016). Greenland fjords are remote and challenging to observe, but Atlantic water has been observed

reaching the glacier termini in them (Sutherland et al., 2013; Straneo et al., 2012; Christoffersen et al., 2012; Holland et al., 2008; Jackson et al., 2014). Warming of ocean temperatures within fjords has been connected to mass loss of glaciers (Luthcke et al., 2006; van den Broeke et al., 2009; Wouters et al., 2008; Howat et al., 2008), but it is difficult to separate contributions from oceanic and atmospheric warming (Straneo et al., 2013; Hanna et al., 2013). The rapid retreat at specific glacial fjords has been preceded by anomalously warm ocean temperatures (Christoffersen et al., 2012; Holland et al., 2008). Therefore, for some portions of the GIS, heat from the ocean may be an important contributor to ice sheet mass loss.

Across the surface of the GIS atmospheric melting produces liquid runoff which is redirected to the base of tidewater terminating glaciers and enters the ocean forming buoyant plumes (Chu, 2014; Slater et al., 2016). These subglacial discharge plumes dilute runoff and drive an exchange circulation within fjords (Carroll et al., 2017; Beaird et al., 2018a; Muilwijk et al., 2022). Within fjords, tidal mixing, internal waves, and shear driven mixing further modify and transform glacial runoff before it is exported onto the shelf (Straneo and Cenedese, 2015a). Because of their small size, fjords are not resolved in the simulations typically used for long term projections of the climate (such as those used in the Climate Model Intercomparison Project 6 (Griffies et al., 2016)). As a result, there is a need to parameterize the mixing within fjords that modifies glacial meltwater in ocean models (Straneo et al., 2019).

Accurate representation of the meltwater fluxes from the GIS is critical because of the possibility that freshening of the Subpolar North Atlantic could disrupt deep convection and the Atlantic Meridional Overturning Circulation (AMOC). The AMOC transports heat northward in the upper ocean and southward in the deep ocean; this northward heat transport maintains the moderate climate of the Northern Hemisphere (Lohmann et al., 2014; Marshall and Schott, 1999). Deep convection occurs during winter when cooling of high salinity surface waters results in the formation of very deep mixed layers which are rapidly restratified in the subsequent spring. Deep convection has been observed in the Labrador, Irminger, and Nordic Seas (Yashayaev and Loder, 2017; Petit et al., 2020; Chafik and Rossby, 2019; Desbruyères et al., 2019). The

water masses formed in each region contribute to the formation of North Atlantic Deep Water (NADW) which is transported south in the lower limb of the AMOC. Anomalous freshening associated with an increase in melt from the GIS could disrupt this process by preventing deep convection (Weijer et al., 2019). Results of the Overturning in the Subpolar North Atlantic Program (O-SNAP) (Lozier et al., 2019; Desbruyères et al., 2019) and other recent observations (Chafik and Rossby, 2019) suggest that overturning occurs primarily in the Irminger and Iceland basins rather than the Labrador Sea. However, results from multi-decadal and multi-centennial climate simulations have shown thatdeep convection in the Labrador Sea is a contributor to AMOC variability (Yeager et al., 2021).

Ocean models have a long history of being used to study the impact of SPNA freshening on the AMOC through what are often referred to as "hosing" experiments. In many of these studies, when freshwater is added, there is an associated decline in AMOC strength (Rahmstorf, 1995; Stouffer et al., 2006; Weijer et al., 2012; Toom et al., 2014; Gierz et al., 2015; Lenaerts et al., 2015; Bakker et al., 2016; Yu et al., 2016; Brunnabend and Dijkstra, 2017; Jackson and Wood, 2018; Berk et al., 2021). However, the total volume of meltwater from the GIS remains low compared to the theoretical or projected values used in many studies that show an AMOC decline (Bamber et al., 2018).

Previous studies have shown that the AMOC response to hosing from the GIS depends on whether the simulated ocean dynamics include mesoscale eddies (Toom et al., 2014; Böning et al., 2016). The AMOC is a global-scale feature of the ocean, but the process of deepwater formation is influenced by mesoscale eddies. In the Labrador Sea, the Rossby radius is 8 km (Nurser and Bacon, 2014; Funk et al., 2009). In general, anticyclones will deepen the mixed layer and cyclones make it shallower (Gaube et al., 2019). Mesoscale eddies influence the production of deep water in the Labrador Sea, and modeling studies suggest that resolving (rather than parameterizing) mesoscale eddies results in a decline in deep convection (Chanut et al., 2008; Tagklis et al., 2020; Pennelly and Myers, 2020).

In this thesis, we explore the connection between GIS and the ocean using results from

high-resolution simulations. These simulations either permit or resolve mesoscale eddies in the SPNA. Because we use a global domain, the results are not influenced by our choice of lateral boundary conditions (e.g, the representation of remote oceanic forcing). First, we find that mesoscale eddies are important in driving the on-shelf transport of heat near the Denmark Strait. In the the next chapter, we use a mesoscale eddy-resolving simulation to study the impacts of GIS meltwater on the off-shelf transport of freshwater. We find that the vertical dilution of meltwater increases eddy activity and the transport of freshwater into the Labrador Sea. Finally, we present a parameterization for the mixing within fjords to better represent the dilution of meltwater.

Chapter 1

Mechanisms of Heat Flux Across the Southern Greenland Continental Shelf in 1/10° and 1/12° Ocean/Sea ice Simulations

1.1 Introduction

The Greenland Ice Sheet (GIS) is losing mass at an increasing rate, from 51 ± 17 GT yr^{-1} in the 1980s to 286 ± 20 GT yr^{-1} in the 2010s (Mouginot et al., 2019). From 1972 to 2018, this mass loss has contributed 13.7 ± 1.1 mm to global sea level rise (Mouginot et al., 2019). Recently Smith et al. (2020) reported a total mass loss of 200 ± 12GT yr^{-1} from 2003 to 2019. Projections of sea level rise due to ice sheet mass loss emphasize the short-term (next 100 years) importance of the GIS contribution as oceanic and atmospheric temperatures rise (Meehl et al., 2007). The lack of representation of both ice sheet dynamics and ice-sheet connections to the ocean and atmosphere in climate models contributes significantly to the uncertainty of these projections. An estimated $15-25\%$ of total mass loss from the GIS is from melting marine terminating glaciers, with an additional $15-25\%$ from calving fluxes (Benn et al., 2017).

The margin of the GIS is comprised of both land-terminating and marine-terminating glaciers. The marine-terminating glaciers are the primary connection between the ocean and the GIS via the circulation in the deep narrow fjords where they are located. Warm salty water, mainly of subtropical North Atlantic origin, is thought to provide the source of heat needed for

ocean-driven melting (Straneo and Heimbach, 2013; Rignot et al., 2012). Marine-terminating glaciers in the southeastern portion of the GIS are particularly vulnerable to ocean-driven melting as they are in closest proximity to the location where Atlantic-originated water intrudes onto the continental shelf (Millan et al., 2018). Over the southeast portion of the GIS, the observed mass loss (Luthcke et al., 2006; van den Broeke et al., 2009; Wouters et al., 2008) is, in part, attributed to warming ocean conditions (Howat et al., 2008), but it is difficult to separate these effects from those of atmospheric warming (Straneo et al., 2013; Hanna et al., 2013). The presence of warm water on the southwest shelf has also been reported (Sutherland et al., 2013; Straneo et al., 2012). Observations from specific glacial fjords have shown warming of ocean water preceding glacial retreat events (Christoffersen et al., 2012; Holland et al., 2008), implying that in some regions heat from the ocean may be the leading driver of ice sheet mass loss. Within fjords, observations have provided estimates of the penetration of warm water to the front of glaciers (Jackson et al., 2014) given the presence of Atlantic-sourced water on the continental shelf.

The Greenland continental shelf is impacted by the fresh and cold water masses exported from the Arctic Ocean as well as the warm and salty water masses advected from the North Atlantic (Figure 1.1, redrawn based on Holliday et al. (2018)). Warm water from the subtropical gyre is advected into the subpolar gyre by the North Atlantic Current (NAC), an extension of the Gulf Stream. The NAC consists of multiple northward branches; eastward branches enter the Nordic seas, while those to the west retroflect to enter the Irminger Current (Holliday et al., 2018). Just south of the Denmark Strait, the Irminger Current retroflects, and its primary branch heads southward along the Greenland continental shelf break. On the Greenland continental shelf, from Fram Strait to Cape Farewell, the East Greenland Current (EGC) flows southward, advecting cold fresh water from the Arctic and seasonal sea ice melt. The weaker and narrower East Greenland Coastal Current (EGCC) is present onshore of the EGC both north and south of the Denmark Strait (Håvik et al., 2017; Sutherland and Pickart, 2008; Foukal et al., 2020).

The transport at the Denmark Strait across the sill has multi-day variability associated with boluses and pulses of overflow water (Appen et al., 2017). Downstream, mesoscale variability

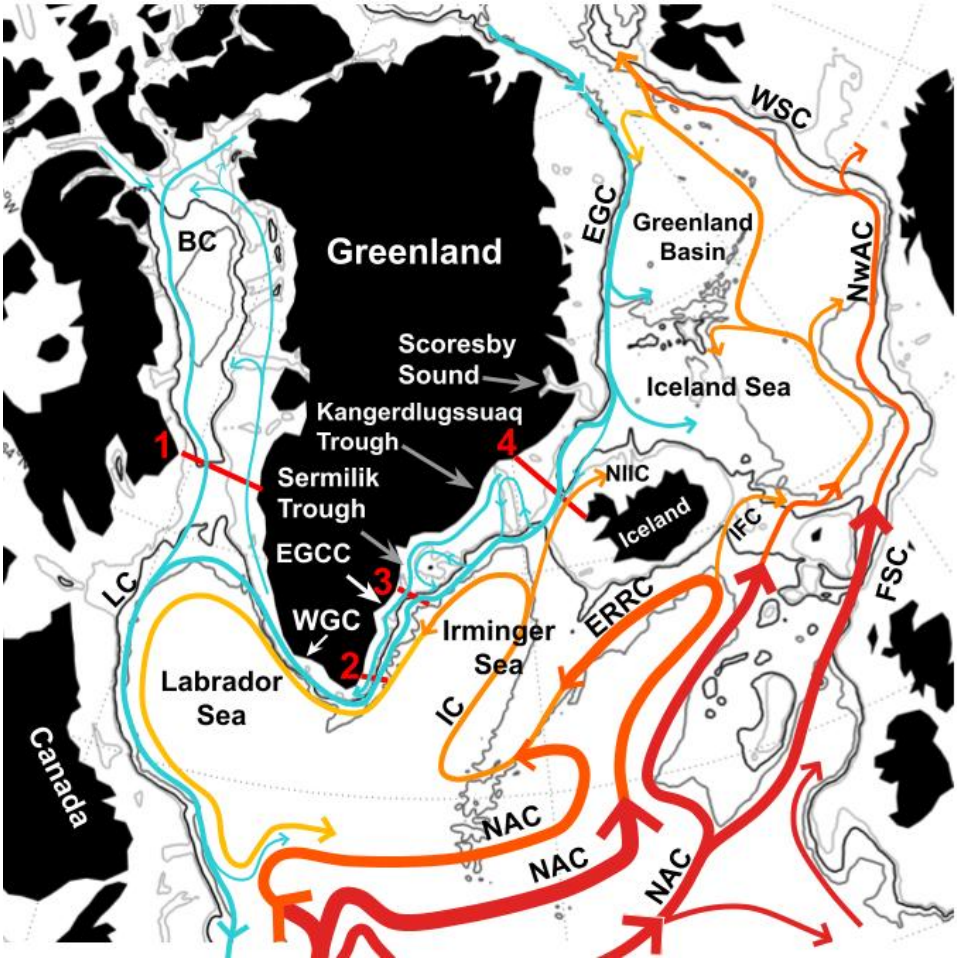

Figure 1.1. Schematic of circulation in the Subpolar North Atlantic, isobaths are plotted at 400, 800, and 2000 m. Major currents are labeled: North Atlantic Current (NAC), East Reykjavik Ridge Current (ERRC), Irminger Current (IC), East Greenland Current (EGC), East Greenland Coastal Current (EGCC), West Greenland Current (WGC), Labrador Current (LC), Baffin Current (BC), North Icelandic Irminger Current (NIIC), Iceland-Faroe Current (IFC), Faroe-Shetland Current (FSC), Norwegian Atlantic Current (NwAC), and West Spitsbergen Current (WSC). The major transects used to divide the regions on the shelf are labeled 1-6: (1) Davis Strait, (2) Cape Farewell Gate, (3) Sermilik Gate, (4) Denmark Strait. After Holliday et al. (2018) with additions from (Sutherland and Pickart, 2008; Håvik et al., 2017; Saini et al., 2020; Furevik and Nilsen, 2005; Rossby et al., 2018).

is dominated by Denmark Strait Overflow eddies (DSO eddies), sometimes described as DSO cyclones. These eddies have been studied in observations (Moritz et al., 2019; Appen et al., 2014) and models (Almansi et al., 2020, 2017). Spall and Price (1998) used an idealized model to show that DSO eddies form south of the Denmark Strait as a result of the potential vorticity anomaly associated with the transport of overflow water across the sill. They further showed that these eddies propagate along the shelf break with the phase speed of a topographic Rossby wave. This was shown to be consistent with observations of DSO eddies at a mooring array 280 km downstream of the Denmark Strait by Appen et al. (2014).

The role of ocean heat in melting the Greenland Ice Sheet has motivated many studies that focus on how warm water reaches the glacial face. Key questions asked include what mechanisms are responsible for property transport from the shelf into fjords (Jackson et al., 2014, 2018; Fraser and Inall, 2018) or towards the ice sheet within specific troughs (Christoffersen et al., 2011; Gelderloos et al., 2017). Gillard et al. (2020) took a comprehensive approach to studying the heat fluxes into specific troughs in east and west Greenland. They found that the seasonal peak in the heat content of the troughs was linked to the distance from the Irminger Sea, indicating the importance of Irminger Water as a source of heat for west Greenland troughs as well as east Greenland troughs. In comparing simulations with and without storms, they found that without storms there was greater heat flux into the Helheim Glacier trough (located on the Southeast Continental Shelf). This study expands on the underlying theory of Gillard et al. (2020) by looking not just at specific troughs but the entire southern Greenland continental shelf.

Our study focuses on two mechanisms of cross-shelf heat flux as depicted by two forced coupled ocean–sea ice simulations performed with 1/10° and 1/12° configurations of the Parallel Ocean Program (POP) and the HYbrid Coordinate Ocean Model (HYCOM), respectively. By comparing temperature on the shelf and the cross-shelf heat flux in the two simulations, we are able to gain insight into the dominant mechanisms of shelf–basin exchange. The two simulations are configured differently and use different atmospheric forcing and therefore are independent experiments in which the mechanisms that drive on-shelf heat flux and shelf–basin exchange are

explored. Robust processes are expected to be found in both simulations.

In Section 1.2, we begin with a description of the model configurations and a definition of the cross-shelf fluxes. Next, we define the shelf control volume and examine the spatial patterns of temperature and cross-shelf heat flux in southern Greenland. In Section 1.2.4, the temperature and velocity from the simulations are compared, with relevant observations included for context. In Section 1.3, we examine the mean heat flux and daily variability, we identify a high-frequency propagating signal that is consistent with DSO eddies. In Section 1.4, we find that the contribution of the high-frequency signal to the cross-shelf heat flux differs between the simulations.

1.2 Methods

1.2.1 Model Descriptions

The two coupled ocean–sea ice models that we compare have horizontal resolutions that are comparable to the first baroclinic Rossby radius of deformation (λ_1) in this region (6–8 km in the deep ocean). The effective grid spacing in this region in POP is $\sim$5–6 km and $\sim$4-5 km in HYCOM. Models with this resolution are classified as "eddy-permitting" (Dukhovskoy et al., 2016a; Nurser and Bacon, 2014) since their grid spacings are greater than half the size of λ_1 (Hallberg, 2013). The first baroclinic Rossby radius is even smaller on the continental shelf (2-4 km Nurser and Bacon, 2014); therefore, both models have limited ability to capture small (less than $\sim$10 km) mesoscale shelf processes. Each model is forced by a different set of atmospheric observations, and neither assimilates data. This allows each model to act as an independent representation of the dynamics in this region. Both models are coupled to the same version of the sea ice model and do not include any representation of freshwater from GIS melt.

0.1° Global POP - CICE 4

We use results from a global 62-year (1948-2009) simulation of POP version 2 (Dukowicz and Smith, 1994) and the Community Ice Code version 4 (CICE4; Hunke et al., 2010) coupled

together in the Community Earth System Model (CESM; Hurrell et al., 2013) version 1.2 framework (McClean et al., 2018). For further details on this simulation, see Wang et al. (2018, 2021); Palóczy et al. (2018, 2020); Castillo-Trujillo et al. (2021); Arzeno-Soltero et al. (2021). This simulation is referred to as POP from here on in the text.

The ocean and sea ice models are on a 0.1° tripolar grid. POP has 42 non-uniformly spaced vertical levels; they range from having 10-m spacing at the surface to 250 m in the deep ocean. The bathmyetry is based on ETOPO2 with minor modifications in the Arctic (more details are given by McClean et al. (2011)). Partial bottom cells are used to more smoothly represent the bathymetry. The ocean model has an implicit free surface and is globally volume conserving.

The atmospheric forcing is given by the Coordinated Ocean-ice Reference Experiment–II (CORE-II) corrected interannually varying fluxes (CIAF; Large and Yeager, 2009)) and has a horizontal resolution of $\sim 1.9°$. Ocean surface evaporation and precipitation fluxes and runoff are implemented using virtual salt fluxes; for this simulation, a surface salinity restoring condition with an effective timescale of about four years limits model drift. Daily-averaged output, obtained by first accumulating quantities at every model time step, was used in our analyses for the period 2005 to 2009; the output includes the total heat flux covariance terms (see Equation 1.3).

0.08° Arctic Ocean HYCOM - CICE 4

The second model used in this study results from numerical experiments by Dukhovskoy et al. (2019) conducted using regional 0.08° Arctic Ocean (Bleck, 2002; Chassignet et al., 2003, 2007) coupled to CICE4. This simulation is referred to as HYCOM in the text.

The model domain is a subset of the 0.08° global HYCOM (Chassignet et al., 2009; Metzger et al., 2014) north of 38°N. The computational grid of the 0.08° HYCOM-CICE is a Mercator projection from the southern boundary to 47°N. North of 47°N, it employs an orthogonal curvilinear Arctic dipole grid (Murray, 1996). The model has effective spacing of ∼4-5 km in the Subpolar North Atlantic. The model topography is derived from the Naval Research Laboratory Digital Bathymetry Data Base 2-minute resolution (NRL DBDB2). In the

current configuration, HYCOM employs a vertical grid with 41 hybrid layers that provide higher resolution in the upper 1500 m. HYCOM vertical hybrid grid is not fixed in time nor in space; the vertical grid transitions from isopycnal or geopotential coordinates to terrain-following vertical grid over the shelves. In this configuration, 10 layers are distributed in the upper 38 m, and 20 layers in the upper 125 m. This simulation is one-way nested within the 0.08° Global HYCOM +Navy Coupled Ocean Data Assimilation (NCODA) 3.0 reanalysis (Metzger et al., 2014) (for 1993–2005) and Global Ocean Forecasting System (GOFS) 3.1 analysis (for 2006–2016).

Atmospheric forcing fields are obtained from the National Centers for Environmental Prediction (NCEP) Climate Forecast System Reanalysis (CFSR, horizontal resolution of 38 km) (Saha et al., 2010) for 1993–2011 and CFSv2 (Saha et al., 2014) for 2012–2016. More details on the model configuration and computational grid as well as model validation and analysis of the model experiments are given by Dukhovskoy et al. (2019, 2021). We use daily-averaged output from 2005 to 2009 for our analysis; unlike in POP the total heat flux covariance term was not saved.

1.2.2 Volume and Heat Flux Definitions

Both volume and heat fluxes integrated along a transect and over depth are calculated using daily means of velocity from the two models. When calculating the total flux through a strait or into a control volume, we consider the flux to be a transport. Transects extend along the continental shelf break in sections that are delineated by cross-shelf “gates". The net volume flux across the shelf break is defined as

$$V_{SB} = \int_H^0 \int_0^L \hat{v}\, d\hat{x}\, dz, \tag{1.1}$$

where $\hat{x}$ is the along-boundary direction and $\hat{v}$ is the velocity component perpendicular to the transect, H is the depth of the transect, and L is the length of the transect. In the case of the shelf break transect, the positive normal direction, n, is defined such that $\hat{v} = \mathbf{v} \cdot \mathbf{n} > 0$ is onto the

shelf. In the case of the gates, the volume flux is calculated similarly, but the normal direction is northward. This allows us both to look at the overall volume flux onto the shelf and to construct budgets for the individual shelf regions by considering whether the gate is at the northern or southern boundary of the region. If the gate is the northern boundary, the normal direction must be reversed to point into the box.

Heat flux is calculated using daily means of potential temperature and velocity from both models. For the heat flux across the shelf break we define

$$\Phi_{SB} = \int_H^0 \int_0^L \rho c_p (\theta - \theta_{ref}) \hat{v} \, d\hat{x} \, dz, \tag{1.2}$$

where ρ is the density of seawater, c_p is the specific heat capacity of seawater, θ is the potential temperature at the shelf break and θ_{ref} is the reference potential temperature. We have used a reference temperature $\theta_{ref} = -1.8°\text{C}$, which is the salinity-independent freezing temperature in POP (Smith and Gent, 2002). This definition is used both for the flux across the shelf break (Φ_{SB}), and through the various gates (Φ_G). As with the volume flux, positive heat flux is onto the shelf, and gate fluxes are positive in the northern and eastern directions. The choice of reference temperature does not change the net heat transport into an enclosed region (Bacon and Fofonoff, 1996; Schauer and Beszczynska-Möller, 2009).

We can decompose the heat flux into mean and eddy components through a Reynolds decomposition

$$\overline{v\theta} = \overline{v}\,\overline{\theta} + \overline{v'\theta'} \tag{1.3}$$

where $\overline{v}$ is the monthly average velocity and $v' = v - \overline{v}$. With this decomposition, we can quantify the contribution to shoreward heat flux from processes with timescales less than one month, such as mesoscale eddies or topographic Rossby waves. In POP, the covariance term $(v\theta)$ is calculated at every model time step and saved as a monthly average. In HYCOM, this term is not saved, thus we must approximate this term from daily averages.

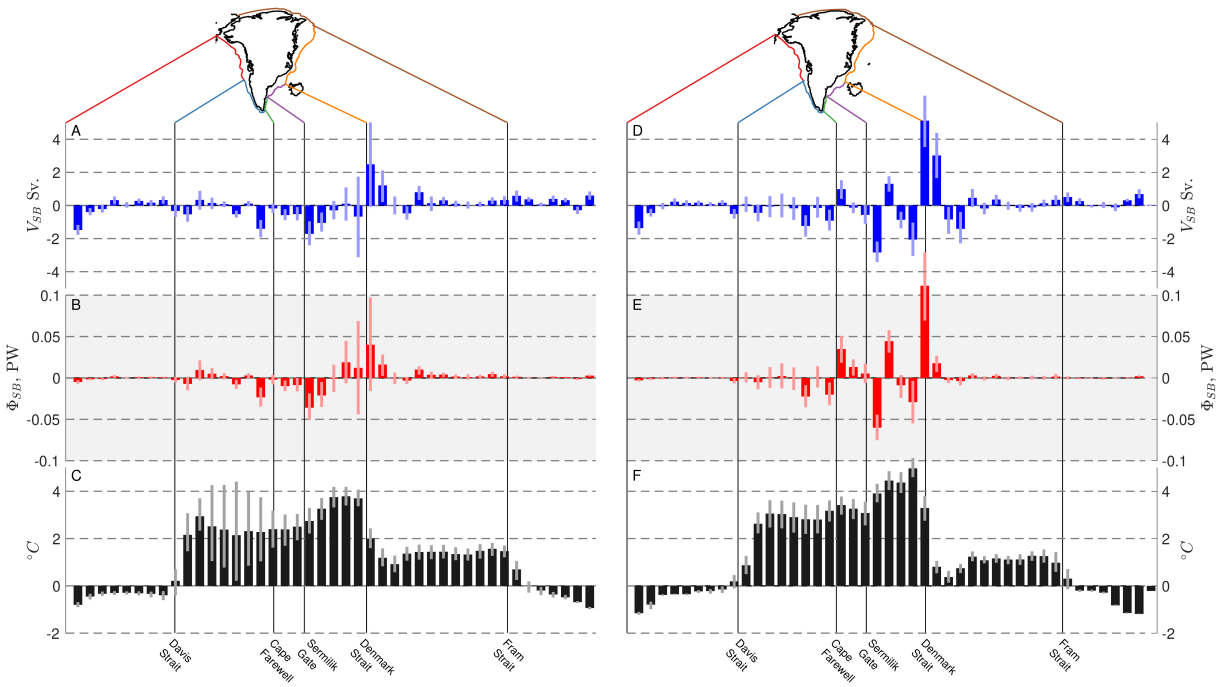

Figure 1.2. Bar graphs of net volume fluxes (Sv, blue), net heat fluxes (PW, red), and average temperature (°C, black) for every 100 km section of the transect encircling Greenland for POP (A-C) and HYCOM (D-F). For both volume and heat fluxes, positive values indicate flux onto the continental shelf. Dark bars are the five-year averages from 2005-2009, with light bars representing the 20th and 80th percentile range. In both models, the strongest on-shelf fluxes are near the Denmark Strait. In POP this maximum is associated with strong variability; in HYCOM the heat flux is consistently onto the shelf at this location.

Figure 1.2 shows the five-year average of the vertically-integrated volume (A for POP and D for HYCOM) and heat (B for POP and E for HYCOM) fluxes from each simulation for every 100 km section of the shelf break transect encircling Greenland. Along the transect, key locations are indicated to show which regions have the strongest fluxes and warmest temperatures. The average temperature at the shelf break in each section is shown in Figure 1.2C (POP) and 1.2F (HYCOM). In both simulations, the strongest on-shelf flux is near the Denmark Strait to its south, with weak on-shelf flux north of the strait and mostly off-shelf flux over the West Greenland shelf break. The magnitudes of the fluxes and their variability differ between the two simulations. From the Denmark Strait to the Davis Strait, HYCOM has warmer water (Figure 1.2F) at the shelf break, with less variability in temperature compared to POP (Figure 1.2C). Combined with stronger volume fluxes in HYCOM (Figure 1.2D vs 1.2A) the result is greater magnitude heat fluxes in HYCOM (Figure 1.2E vs 1.2B). While the HYCOM simulation does not have the same temporal variability as POP, there is along-transect variability where regions of strong off-shelf flux are adjacent to those with strong on-shelf flux. In POP, the temporal variability (shown here by the 20th to 80th percentile range) is large relative to the mean between Sermilik Gate and the Denmark Strait. Eddies traveling along the shelf break in this region could explain some of this variability, as discussed further in Section 1.3.2.

The models do not agree on the sign of volume or heat flux across the shelf in each 100 km section. This is likely the result of differences in the modeled circulation, and sensitivity of these results to the particular part of the continental shelf break sampled.

1.2.3 Continental Shelf Control Volumes

To understand how warm salty Atlantic water crosses onto the shelf and where it is present, the shelf and shelf break must be clearly defined. Shallow straits and deep troughs make choosing a single isobath to represent the shelf break challenging. Based on Figure 1.2, we limit our focus to the southern shelf break, extending from Davis Strait to Denmark Strait (see Figure 1.3A–B), where the strongest on- and off-shelf heat and volume fluxes occur. The exact depths

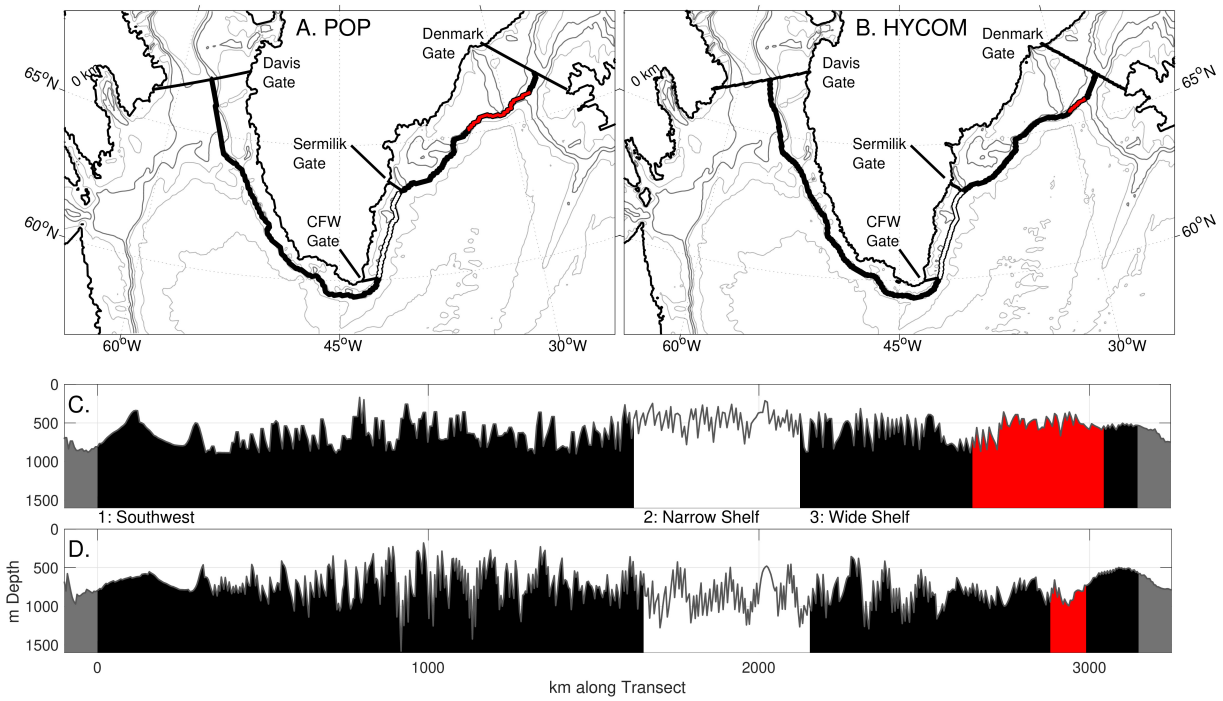

Figure 1.3. Map of shelf break transects in (A) POP and (B) HYCOM, subdivided at the major straits and gates and plotted over the regions' bathymetries. The the exact depth along the transect plotted for (C) POP and (D) HYCOM with the regions numbered. Shelf regions are: (1) Southwest, (2) Narrow Shelf, and (3) Wide Shelf. The color of the transect in each region corresponds to the bathymetry plotted for that region. The red line highlights the region of the shelf where we observe the propagating high-frequency signal discussed in section 1.3.2. A regional map of the Southeast region directly comparing the two bathymetries is provided in the Supplemental Materials Figure 1.

of the shelf break transect in each model (see Figure 1.3C–D) show how the bathymetry of the two simulations differs. See Supplemental Materials Figure 1 for a detailed map of the Southeast region highlighting the troughs and small scale bathymetry.

In addition to the shelf break, we define three control volumes to examine spatial differences in cross-isobath fluxes and properties on the shelf. The contour begins at the Davis Strait (0 km), and the along-transect distance used in this paper is measured from that point counterclockwise, first south along western Greenland then north along eastern Greenland. We subdivide the shelf break into three regions: from Davis Strait to Cape Farewell, Cape Farewell to the Sermilik Gate, and the Sermilik Gate to the Denmark Strait. The gates are labeled in Figure 1.3A–B, and span the shelf from the coast to the shelf-break contour. Between these gates we define the regional control volumes of the continental shelf as: (1) Southwest, (2) Narrow Shelf, and (3) Wide Shelf. The Southeast region has been subdivided into the Narrow and Wide sections because of differences in the cross-shelf exchange that we calculated along the shelf break. The Cape Farewell Gate is located at the same position as the Overturning in the Subpolar North Atlantic Program (OSNAP) mooring array at 60°N (Le Bras et al., 2018).

1.2.4 Model Intercomparison: Velocity and Temperature

Before focusing on the heat fluxes across the shelf, we compare the velocity and temperature around the Greenland continental shelf in the two simulations. The goal of comparing velocity and temperature is to provide context for the differences in cross-shelf fluxes between the two simulations. We refer to observations to provide context or show the possible model biases but the goal of this section is not to validate either simulation. To calculate the differences, both the POP and HYCOM outputs are interpolated onto a uniform 1/10° degree grid.

The mean surface circulation for 2005-2009 is shown for both models in Figure 1.4A–B; depth-averaged velocity over the upper 50 m of the water column is considered to be the surface flow. Both models show the observed structure of the East Greenland/Irminger Current merging at Cape Farewell (Le Bras et al., 2018). On the shelf, the complex structure of the East Greenland

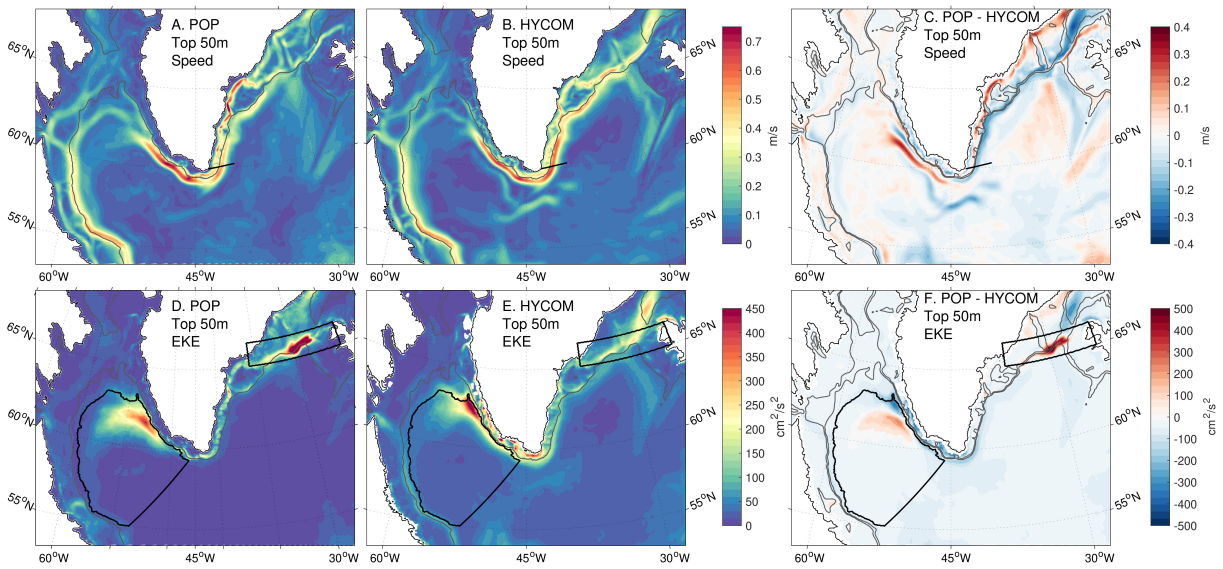

Figure 1.4. Average speed in the top 50 m over 2005-2009 for POP (A), HYCOM (B), and POP-HYCOM (C). Average Eddy Kinetic Energy over the same period in the top 50 m over 2005-2009 for POP (D), HYCOM (E), and POP-HYCOM (F). In (A,B,C) the black line shows the transect at 60°N. In (D,E,F) the boundary of two control volumes are shown in black: the interior Labrador Sea defined by the 2,000 m isobath and a box at the Denmark Strait.

Coastal Current is better represented in POP (Bacon et al., 2014; Sutherland and Pickart, 2008). At 60°N, at the Cape Farewell Gate, the black line in Figure 1.4A–B, the peak velocity in HYCOM is 64 cm s^{-1} at a position 120 km from the coast. In POP there are two peaks in the surface speed: 35 cm s^{-1} located 97 km from the coast and 42 cm s^{-1} located 155 km from the coast. The average velocity along the shelf at the Cape Farewell Gate is included in the Supplemental Materials Figure 2. This difference in current structure contributes to the difference in net transport onto the shelf between the two models (Figure 1.5A–B). In POP, the coastal currents are stronger and the shelf slope currents are weaker in the southeast region (Figure 1.4C). However, the West Greenland Current has a stronger core that is shifted farther of the shelf in POP compared to HYCOM.

We calculate the EKE from the daily averages of model velocity. We define EKE as:

$$\mathrm{EKE} = \frac{u'^2 + v'^2}{2} \tag{1.4}$$

with $u' = u - \overline{u}$, where u is the daily average velocity and $\overline{u}$ is the monthly average of velocity. This formulation defines eddies as anomalies that have a period between two days and one month. We use only the depth averaged velocity in the top 50 m. The 2005-2009 average is plotted in Figure 1.4D–E. In both models, west of Greenland there is an expanse of elevated EKE extending into the central Labrador Sea (outlined in black in Figure 1.4D–E). The region of elevated EKE in the Labrador Sea in the POP simulation does not extend onto the Southwest Shelf; in contrast the HYCOM simulation has elevated EKE on and off the shelf, possibly indicating a difference in the cross-shelf exchange between the two models in this region. EKE estimated from TOPEX/Poseidon satellite altimetry (Brandt et al., 2004) and surface drifters (Fratantoni, 2001) in this region shows a similar pattern of elevated EKE in the eastern Labrador Sea; though neither observation-derived estimate is directly comparable to the EKE calculated from the simulations. The surface EKE from Brandt et al. (2004) in the West Greenland Current ranges from 400 to 800 $cm^2\ s^{-2}$ for the period 1997-2001. Altimeter-based estimates are generally higher than those in either simulation, but are calculated from sea-surface height gradients and the resulting geostrophic velocities, while the model EKE includes both geostrophic and ageostrophic velocities. Estimates of EKE from 15 m drogued satellite-tracked surface drifter paths from 1990-1999 are 400 to 500 $cm^2\ s^{-2}$, which is consistent with the maximum EKE of both models within the defined interior Labrador Sea control volume (shown in black in Figure 1.4D–E) calculated from the depth average velocity in the top 50 m. In the Labrador Sea, the maximum EKE in POP is 432 $cm^2\ s^{-2}$, while in HYCOM it is 527 $cm^2\ s^{-2}$. The average EKE in HYCOM is 53.2 $cm^2\ s^{-2}$, with the 20th to 80th percentiles ranging from 20.0 to 62.9 $cm^2\ s^{-2}$. POP values are similar: mean EKE is 51.1 $cm^2\ s^{-2}$, with 20th to 80th percentiles from 10.1 to 82.0 $cm^2\ s^{-2}$. The EKE fields depicted by the two simulations have similar magnitudes and patterns as those observed in the Labrador Sea.

There is a second region of elevated EKE where the Irminger Current retroflects south of the Denmark Strait. This corresponds to a region of large sea surface height anomalies observed by AVISO (Trodahl and Isachsen, 2018). Heightened EKE near the Denmark Strait is also

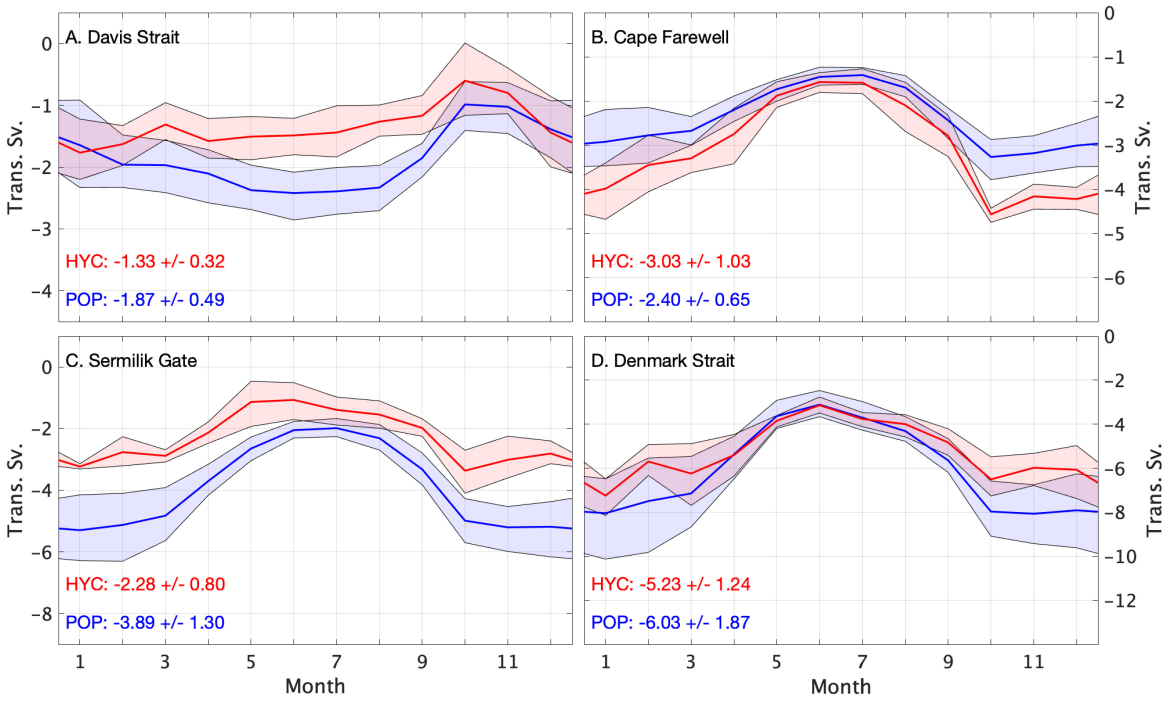

Figure 1.5. Volume transports through straits defined in Figure 1.3 from POP (blue) and HYCOM (red) and with the shaded region showing the 20th-80th percentile range; the annual mean and standard deviation are included on each plot. Transports are from (A) Davis Strait (B) Cape Farewell Gate (C) Sermilik Gate (D) Denmark Strait; here strait refers to the entire transect between two land masses and gate refers to the area between the Greenland coast and the defined shelf break. Negative transrport is southward.

consistent with observations of mesoscale eddies and boluses formed at the Denmark Strait overflow (Moritz et al., 2019). The average EKE in the defined box just south of the Denmark Strait (outlined in red in Figure 1.4C–D) is higher in POP (133 $cm^2\ s^{-2}$) compared to HYCOM (80.7 $cm^2\ s^{-2}$), and the maximum EKE in POP (958 $cm^2\ s^{-2}$) is twice the maximum in HYCOM (429 $cm^2\ s^{-2}$). In the POP field there is a particularly strong band of EKE just south of the strait at the shelf break, while in the HYCOM field the maximum is broader and is located to the north of the strait.

In addition, we compare the transport through key straits to further understand differences in the simulated oceans. The 2005-2009 average of transport for each month is plotted in Figure 1.5 for: Davis Strait (Figure 1.5A, from Canada to Greenland), Cape Farewell Gate

(Figure 1.5B, Greenland to the shelf break contour), Sermilik Gate (Figure 1.5 C, Greenland to the shelf break contour), and Denmark Strait (Figure 1.5D, Greenland to Iceland). Here, “strait" refers to the entire transect between two land masses, and “gate" refers to the area between the Greenland coast and the defined shelf break. At the Davis Strait, the average volume transport for 2005–2009 in HYCOM is $V_{DS} = -1.33 \pm 0.23$ (1 Sv = 10^6 $m^3 s^{-1}$), and in POP $V_{DS} = -1.87 \pm 0.49$. Curry et al. (2014) found the Davis Straight volume transport to be -1.6$\pm$ 0.5 Sv from observations for 2004-2010. On the shelf, the 5-year average volume flux at Cape Farewell is $V_{G:CFW} = -3.03 \pm 1.03$ in HYCOM and $V_{G:CFW} = -2.40 \pm 0.65$ in POP. At the Cape Farewell Gate the winter maximum volume transport in HYCOM is 1 Sv greater than the maximum in POP. Observations from the OSNAP east array, the same location as the Cape Farewell Gate, showed the average transport of the East Greenland Current from 2014-2016 to be -3.5$\pm$0.5 Sv (Le Bras et al., 2018). The 5-year average transport at the Sermilik Gate in HYCOM is $V_{G:SG} = -2.28 \pm 0.80$ and is $V_{G:SG} = -3.89 \pm 1.03$ in POP. The winter maximum at Sermilik gate is weaker in HYCOM compared to POP by roughly 2 Sv, but the difference in the summer minimum is less than 1 Sv. The observations of Bacon et al. (2014) of the East Greenland Coastal Current are taken at a similar location as the Sermilik Gate; a February maximum transport of 3.8 Sv and an August minimum transport of 1.9 Sv are reported. The 5-year average net transport through the Denmark Strait is $V_{Dmk} = -5.23 \pm 1.24$ in HYCOM and $V_{Dmk} = -6.03 \pm 1.87$ in POP. The summer transport through the Denmark Strait is very similar between the two simulations, but the winter maximum transport can be 1 to 2 Sv greater in POP. The net transport through the Denmark Strait as estimated by Østerhus et al. (2019) is 4.3 Sv southward.

To validate the temperature on the shelf we use temperature measurements from animal-borne instruments from the Marine Mammals Exploring the Oceans Pole to Pole (MEOP) project (Treasure et al., 2017). The data used for comparison are vertical profiles of temperature collected during the upward transit of the instrumented animal. We compare them to model temperature profiles between 60° N to 70° N and 45° W to 27° W. Between 2005 and 2008, a total of 3,382

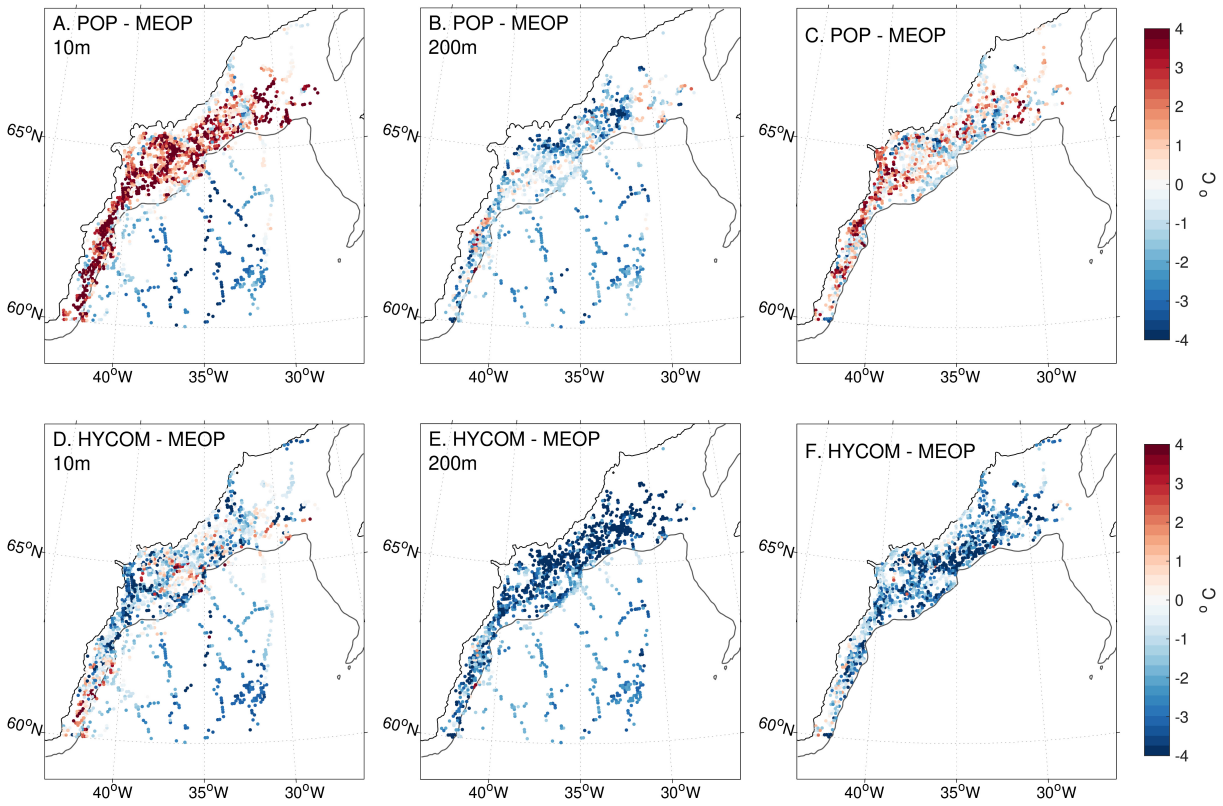

Figure 1.6. Comparisons of temperature from MEOP profiles and either the HYCOM or POP simulations over the southeast Greenland shelf and the Irminger Sea: (A) difference (POP-MEOP) in surface temperature (10m), (B) difference (POP-MEOP) in temperature at 200m, and (C) vertically integrated difference (POP-MEOP) in temperature over the continental shelf, (D) difference (HYCOM-MEOP) in surface temperature (10m), (E) difference (HYCOM-MEOP) in temperature at 200m, and (F) vertically integrated difference (HYCOM-MEOP) in temperature over the continental shelf.

observational profiles were recorded in our defined volume. For each MEOP profile, we sample the concurrent monthly average temperature field from each simulation at the closest model grid point to where the profile was taken.

At the surface, POP is warmer than MEOP on the shelf and cooler in the Irminger Sea (Figure 1.6 A). However, at 200m, POP is generally cooler everywhere (Figure 1.6 B). The vertically averaged difference in temperature shows the warm bias at the surface is greater than the cold bias at depth (Figure 1.6 C). Over the Wide Shelf, POP is 0.31°C warmer than MEOP; over the Narrow Shelf, the warm bias is 0.86°C. HYCOM is colder than MEOP profiles over all (Figure 1.6D–F), but shows some warm biases in the surface layer (Figure 1.6A). The bias over the Wide Shelf is -2.5°C, and over the Narrow Shelf the bias is -1.5°C.

This deviation of shelf temperature in the simulations from observations is likely related to biases both in the ocean heat transport and surface heat fluxes. In POP, the temperature bias is used to calculate a bias in heat content of 1.3 and 3.5 MJ in the Wide and Narrow Shelf regions respectively. In HYCOM, the difference in temperature results in an on-shelf heat content that is -6.0 and -10.1 MJ lower than expected from observations in the Wide and Narrow Shelf regions, respectively. If these biases are entirely from misrepresentations of ocean heat transport, we conclude that the heat transport is likely too strong in POP and too weak in HYCOM.

Direct comparison of the heat content on the shelf in the two simulations is shown in Figure 1.7 for the southwest shelf (A), the Narrow Shelf (B), and the Wide Shelf (C). In all panels of Figure 1.7, the POP results are plotted in blue and the HYCOM results in red. The dark lines show the 2005-2009 average of heat content with the shaded regions showing the 20th-80th percentile range. The printed values in each panel are the averages over 2005-2009 and one standard deviation. In the Southwest Region (Figure 1.7 A), the average heat content on the shelf is similar between the two simulations for most of the year, except from August-November when the heat content on the shelf is greater in POP. The heat content maxima in both models agrees with observations, which have shown the warmest water being present on the shelf between September and January (Grist et al., 2014). Over the Narrow Shelf (Figure 1.7B), the average heat

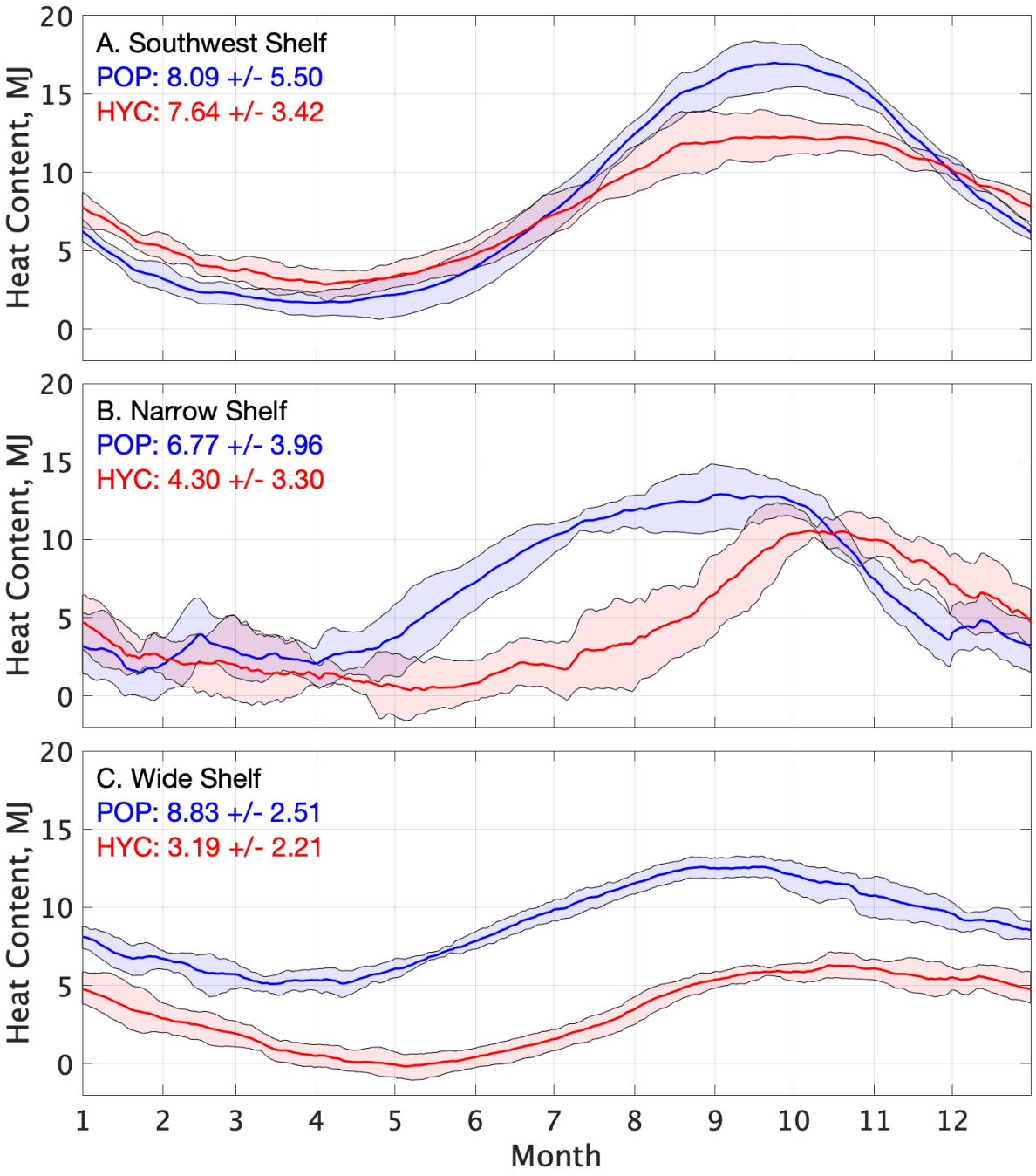

Figure 1.7. Heat content (MJ) on the shelf in the control volumes for the southwest shelf (A), the Narrow Shelf (B), and the Wide Shelf (C) for POP (blue) and HYCOM (red). The dark lines are the average of daily means from 2005-2009 with the shaded region showing the 20th-80th percentile range. The average from 2005-2009 and one standard deviation is listed in every panel.

content in POP is 2.47 MJ greater than the average in HYCOM. On the Wide Shelf (Figure 1.7C), the heat content in the two simulations differs by 5.64 MJ on average, but has a similar seasonal range and standard deviation. The maximum heat content in the Wide Shelf region occurs in September in both simulations; this is in general agreement with Gillard et al. (2020) who found the summer months (July-August) to be the warmest time of year in the Helheim Troughs (near the Sermilik Troughs) and the fall months (September-November) to be the warmest time of year in Kangerdlugssuaq trough.

For both the Narrow and Wide shelf, the difference in the annual average heat content between POP and HYCOM is less than what was found based on the MEOP profiles alone. This is likely because the MEOP data have a seasonal bias; 49% of the profiles used for comparison were collected in June, July or August. During these months, the difference in heat content on the Narrow Shelf in POP and HYCOM is comparable to the difference expected from the comparison to the MEOP data. Direct calculation of the heat content on the shelf is consistent with the conclusion that the Southeast shelf is too warm in POP and too cold in HYCOM.

In general, the mean currents are stronger along the shelf break in HYCOM compared to POP. The EKE shows more energy in POP, particularly near the Denmark Strait. There is not a comparable value to difference with the model. The transport through the straits and gates do not show one simulation to be closer to observations than the other. There is also a stronger cross-shelf temperature gradient in HYCOM. The bias in temperature is smaller in POP compared to HYCOM, and where the shelf is too warm in POP, it is too cold in HYCOM.

1.3 Results

1.3.1 Average fluxes onto the Greenland Shelf

Net volume and heat fluxes through each section and gate around Southern Greenland are listed in Table 1.1. In POP the only region of net heat flux onto the shelf is along the Wide Shelf. In HYCOM there is net heat flux onto the shelf over both the Wide and Narrow Shelf

Table 1.1. Summary of key volume and heat fluxes and control volume temperatures. Cross-shelf heat and volume fluxes (Southwest Shelf, Narrow Shelf, and Wide Shelf) are positive onto the shelf. Gate heat and volume fluxes (Davis Gate, Cape Farewell Gate, Sermilik Gate, and Denmark Gate) are positive northward; note that for gates we consider only flux between the coast and the continental shelf break. Columns 1 and 2 are the length of each section in POP and HYCOM. Columns 3-6 are the 2005-2009 average volume and heat fluxes with an uncertainty of one standard deviation for POP and HYCOM. Columns 7 and 8 are the 2005-2009 volume average temperature of each on shelf control volume.

Section	Length (km) POP	Length (km) HYCOM	V (Sv) POP	V (Sv) HYCOM	Φ (TW) POP	Φ (TW) HYCOM	T_avg (°C) POP	T_avg (°C) HYCOM
Davis Gate	166	192	0.25±0.74	-0.27±0.59	8.52±13.2	-7.85±9.73	-	-
Southwest Shelf	1,622	1,651	-2.40±0.79	-2.15±0.84	-29.9±10.4	-16.6±16.0	1.96±1.36	1.96±0.84
Cape Farewell Gate	77	62	-2.62±0.75	-2.45±0.85	-38.7±19.8	-33.4±18.6	-	-
Narrow Shelf	503	503	-1.13±0.62	-0.59±0.45	-18.0±13.9	28.2±15.7	1.65±1.02	1.41±0.81
Sermilik Gate	74	87	-3.53±1.20	-3.03±1.12	-53.2±21.6	-39.5±21.9	-	-
Wide Shelf	1,021	994	-0.90±0.66	0.77±0.76	16.4±13.8	55.0±23.3	2.15±0.64	0.95±0.55
Denmark Gate	257	361	-4.07±1.42	-2.28±0.95	-33.2±18.9	-13.0±8.43	-	-

regions. This is consistent with Figure 1.2B and E. In both POP and HYCOM, there is less heat flux at Cape Farewell than at the Sermilik Gate indicating that the Narrow Shelf is a region of heat loss, despite it being a region of net on-shelf heat flux in HYCOM.

Along the west Greenland slope, we expect to see off-shelf volume and heat flux in agreement with previous studies (e.g., Dukhovskoy et al., 2019; Böning et al., 2016; Schulze Chretien and Frajka-Williams, 2018; Myers et al., 2009). Cross-isobath heat flux is negative in the Southwest region, consistent with the source of heat to this region originating from southward heat flux at Cape Farewell or surface heat fluxes. Both simulations are consistent in this region, with weak seasonal cycles of heat and volume flux. The volume-averaged shelf temperature of the Southwest region is highly variable, and the fall peak is the warmest volume-average temperature of any region. The presence of warm ocean water in this region is consistent with observations of ocean-driven melting of the ice sheet in west Greenland. (See Straneo and Cenedese, 2015b, for an overview.) Correlation between the heat flux at the Cape Farewell Gate and heat content in the Southwest region is 0.87 in POP and 0.74 in HYCOM; both are significant at a 0.05 significance level. Using the surface heat flux time series saved from the POP simulation, we find that the net surface heat flux and heat content in the Southwest region are out of phase, resulting in a low correlation. In both models, heat flux through the Cape Farewell Gate (Figure 1.5B) as well as the shelf temperature (Figure 1.7A) peak in the fall; in POP the net surface heat flux is highest in the summer.

1.3.2 Daily Variability of flux south of the Denmark Strait

Heat fluxes across the shelf along the southern transect display variability on time scales of several days. Figures 1.8A and 1.9A show five-month-long Hovmöller diagrams of temperature at 200 m in 2005 for each model at the shelf break, illustrating the seasonal progression of warm water from the Denmark Strait to Davis Strait. To reduce noise in all variables from currents meandering across the isobath, a 50 km boxcar filter is applied. Hovmöller diagrams of 200 m temperature for the full five-year period are included in the Supplemental Materials Figures 3

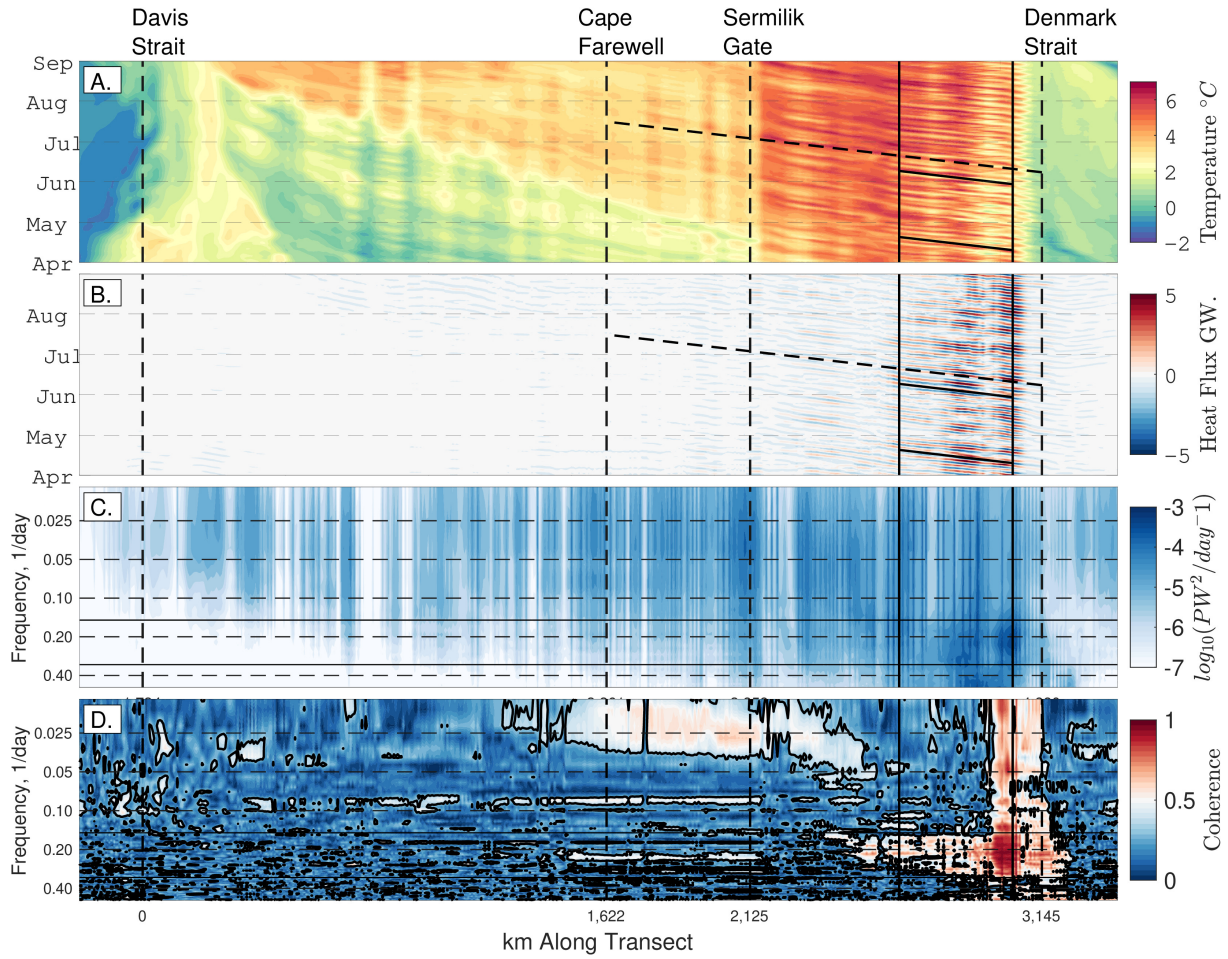

Figure 1.8. POP results showing:(A) Hovmöller diagrams from April to September 2005 of temperature at 200 m, (B) vertically integrated heat flux with a 3-7 day band pass filter, (C) spectra of heat flux at each location along the contour with horizontal lines showing the frequency band that was used to produce (B), and (D) coherence between heat flux at every location and 102 km south of the Denmark Strait. Vertical dashed lines show the locations of the gates, and solid vertical lines show the region of the propagating signal from 102 to 499 km south of the Denmark Strait, highlighted in red in Figure 1.3. The black contour in (D) is the threshold for coherence at the 0.10 significance level $\gamma^2_{XY} = 0.35$. Error for the spectra are estimated using a χ^2 distribution with a 0.05 significance level such that the range between high and low error estimates is $\log_{10}(0.6)$.

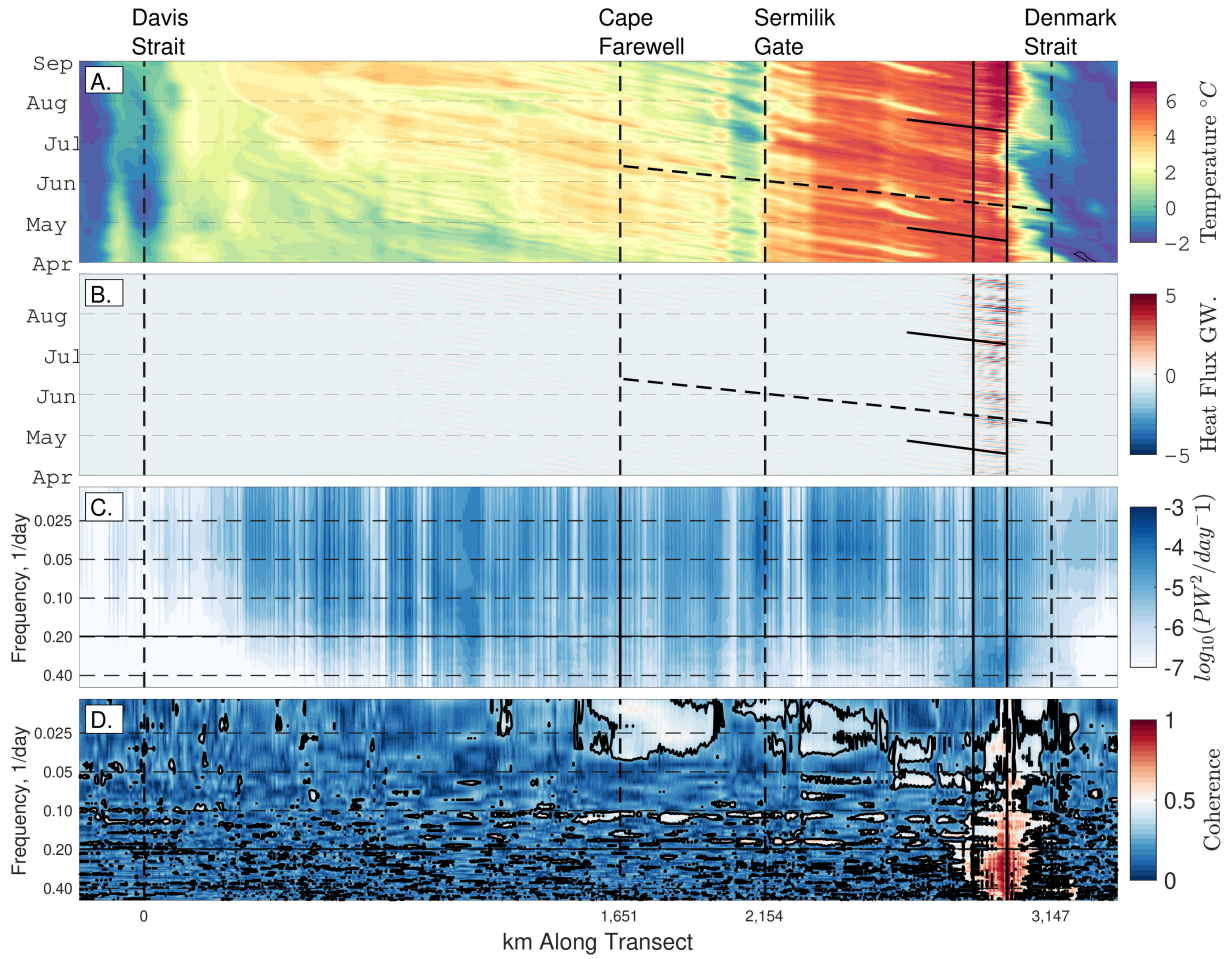

Figure 1.9. As in Figure 1.8. HYCOM results showing:(A) Hovmöller diagrams from April to September 2005 of temperature at 200 m, (B) vertically integrated heat flux with a 2-5 day band pass filter, (C) spectra of heat flux at each location along the contour with horizontal lines showing the frequency band that was used to produce (B), (D) coherence between heat flux at every location and 154 km south of the Denmark Strait, and (E) the associated phase. Vertical dashed lines show the locations of the gates, and solid vertical lines show the region of the propagating signal from 154 to 271 km south of the Denmark Strait, highlighted in red in Figure 1.3. The black contour in (D) is the threshold for coherence at the 0.10 significance level $\gamma^2_{XY} = 0.35$. Error for the spectra are estimated using a χ^2 distribution with a 0.05 significance level such that the range between high and low error estimates is $\log_{10}(0.6)$.

and 4.

At the Denmark Strait there is a front between the cold water to the north and the warm Atlantic water in the Irminger Current in both models (Figures 1.8A and 1.9A), but the water north of the front is much colder in HYCOM (Figure 1.9A) consistent with the average shelf temperatures in both simulations (-0.62±0.17°C compared to 0.11±0.37°C in POP, see Table 1.1). The warmest water at the shelf break in both models is along the Wide Shelf region (between the Denmark and Sermilik Gates). In POP between Sermilik Gate and Cape Farewell seasonal warming occurs in May (Figure 1.8A). However, in HYCOM (Figure 1.9A), the temperature over this portion of the shelf break shows more high-frequency variability than seasonal change. These differences are consistent with the annual cycles of temperature in the Southwest region and heat flux through the Cape Farewell and Davis Gates. The seasonal timing of warming along the western shelf break is consistent with the results of Grist et al. (2014), who showed the warmest waters in that region from September to January.

In both models, there is a high-frequency signal generated at or intersecting the shelf break south of the Denmark Strait in roughly the same location as the cold-warm front (Figures 1.8A and 1.9A). In POP (Figure 1.8A), the origin of these signals is consistently 102 km south of the Denmark Strait. In HYCOM (Figure 1.9A), the position of the cold-warm front meanders and changes in strength over the months shown. These high-frequency signals are generated regularly throughout the year, see supplemental Figures 3 and 4 for the Hovmöller diagrams over the entire 5 year record. As these signals propagate along the transect they result in extreme on- and off-shore heat fluxes.

Figures 1.8B and 1.9B show the band-pass filtered vertically integrated heat flux, and Figures 1.8C and 1.9C show the spectra of the vertically integrated heat flux. In Figures 1.8B and 1.9B, lines are plotted with phase speeds of $c_p = 0.47$ m/s for POP and $c_p = 0.45$ m/s for HYCOM. In both models the heat flux spectra have peaks at high frequency south of the Denmark Strait. In POP (Figure 1.8C), there are three localized regions of high-frequency variability, two with a frequency of about 0.30 day^{-1}, and one around 0.50 day^{-1}, the Nyquist frequency. In

HYCOM (Figure 1.9C) the high-frequency peak is more localized ranging from 0.24 day^{-1} to 0.50 day^{-1}. Therefore, to isolate the heat flux associated with these propagating signals, the models were band-pass filtered with different ranges: for POP the range is a period of 3-7 days, and for HYCOM the range is 2-5 days. The band-pass filtered heat flux in both models (Figures 1.8B and 1.9B) shows a propagating signal, though the signal travels only 116 km in HYCOM, while in POP it continues for 397 km. The location where the signal dissipates in HYCOM (Figure 1.9B) coincides with the mouth of Kangerdlugssuaq Trough. In POP (Figure 1.8B) the signal dissipates on the north end of the Sermilik Troughs. See Figure 1.3, where the portion of the shelf where the propagating signal is strongest is shown in red. In both cases the dissipation or on/off-shelf shifting of the signal occurs where there is a change in bathymetry. In both models (Figures 1.8C and 1.9C), the high-frequency energy in the spectra of vertically integrated heat flux decays southward along the shelf.

The band-pass filtered vertically integrated heat flux is not best way to see the propagation of the eddies. Since the topographic Rossby wave phase velocity changes along the shelf break features due to changes in stratification and bottom slope, so will the frequency of the eddy. In Figures 1.8A and 1.9A, the propagating signal is apparent in the 200m temperature much farther from the Denmark Strait than in the filtered heat flux. In the spectra, Figures 1.8C and 1.9C, there is energy in this high-frequency band along nearly the entire southeast shelf break. The magnitude of the impact on the vertically integrated heat flux is strongest from 102 to 499 km south of the Denmark Strait in POP and 154 to 271 km south of the Denmark Strait in HYCOM.

The coherence of heat flux time series at each location along the transect and the heat flux at the location where the signal originates is shown in Figures 1.8D and 1.9D. The 0.10 confidence level for the coherence squared is $\gamma^2_{XY} = 0.35$, the black contour in both plots. These results are sensitive to the choice of the location where the signal originates due to the high grid-point to grid-point variability in the flux. For both models, there are regions of strong coherence both north (upstream, closer to the Denmark Strait) and south (downstream, farther from the Denmark Strait). The upstream coherence shows the possible origin of the signal. In

HYCOM (Figure 1.9D), the coherence is not significant north of the Denmark Strait in the same narrow high-frequency band (0.24-0.5 day^{-1}). In POP (Figure 1.8D), the coherence is significant north of the Denmark Strait across most frequencies in the 3-7 day band. In both models, where the coherence is significant south of the Denmark Strait, the phase (not plotted) shows evidence of a propagating signal. In both POP and HYCOM, there is also significant coherence at a lower frequency (f=0.1 day^{-1}) extending along the shelf to Cape Farewell beyond the defined regions of propagation. This could be associated with a shift in the speed of the eddies as they travel along the shelf. Both POP and HYCOM show a coherent signal at $f > 0.025$ day^{-1} along the Narrow Shelf region indicating that a lower frequency signal also connects these two shelf regions.

From the phase we can estimate the phase velocity of the propagating signal (Münchow et al., 2020; Pickart and Watts, 1990). A middle frequency of each band of coherence was used: f_{POP}=0.21 day^{-1} for POP and f_{HYCOM}=0.34 day^{-1} for HYCOM. A location was chosen along the transect near where the coherence at that frequency is no longer significant, 499 km south of the Denmark Strait in POP, 271 km in HYCOM; the distance between the two locations is D. At that frequency and location, the phase is $\Theta_{XY} = 80^\circ$ in POP and $\Theta_{XY} = 34^\circ$ in HYCOM. We calculate the phase speed as $c_p = f(360/\Theta_{XY})(D/\cos\Delta)$, where Δ is the angle between the wavenumber vector and the direction of the shelf break, the estimate of Δ is the greatest source of uncertainty in this estimate. For POP, the resulting phase velocity is $c_p = 4.5$ m/s and wavelength $\lambda = 1,796$ km; for HYCOM, the resulting phase velocity is $c_p = 5.2$ m/s and wavelength $\lambda = 1,334$ km. The spectra, coherence, and phase used for estimating the phase velocity are shown in the Supplemental Materials Figure 5. These phase velocities differ greatly, $\sim$10 times greater than the speed associated with the lines on the Hovmöller diagrams in Figures 1.8B and 1.9B.

We use the dispersion relation for topographic Rossby waves

$$\omega(K) = \frac{-N\alpha\sin(\phi)}{\tanh(KL_D)}, \tag{1.5}$$

where N in the stability frequency, α is the bottom slope, and L_D is the internal Rossby radius of deformation (Gill, 1982; Rhines, 1970). The orientation of the wavenumber vector is $\sin(\phi) = k/K$ where $\vec{k} = (k,l)$ and $K = \sqrt{k^2+l^2}$. The stability frequency N is estimated from profiles of the 5-year average stratification in this region of the shelf: $N = 0.003$ s^{-1} in POP and 0.002 s^{-1} in HYCOM. The average bottom slope estimated from the change in local bathymetry is $\alpha = 0.02$ for both POP and HYCOM. The Rossby radius of deformation $L_D = ND/f$, calculated at each point along the contour using the local depth and Coriolis parameter, has an average value of $L_D = 12$ km in this region of both models. For POP, using this equation and the estimated wavelength from the phase analysis, the value of $\phi = 1^\circ$, compared to the orientation of the current ellipse at the shelf break $\theta = -6^\circ$. In HYCOM, the angle of the wavenumber vector is $\phi = 2.6^\circ$, and the average direction orientation of the current ellipse is $\theta = 12^\circ$.

Phase speed alone is not sufficient to differentiate between TRWs and DSO eddies (Spall and Price, 1998). Coherent eddies can be identified by their high relative vorticity, a measure of the local rotation of a water parcel. A comparison of the magnitude of strain and relative vorticity in a flow, the Okubo–Weiss parameter, is widely used to track coherent eddies (Okubo, 1970; Weiss, 1991). In POP, where the signal is strongest, we calculated the relative vorticity, $\zeta = \partial v/\partial x - \partial u/\partial y$, where u is the zonal velocity and v is the meridional velocity and divide by the Coriolis parameter, f, to define the nondimensional relative vorticity. Along the shelf break, at 200 m this quantity is positive (indicating cyclones) off the shelf, and negative (indicating anti-cyclones) on the shelf, consistent with Almansi et al. (2020) (see Supplemental Material Figure 6). Combined with the location, the frequency, the propagation speed along the shelf break, and the spatial pattern of the average nondimensional relative vorticity, we conclude that the high frequency variability in the heat flux across the shelf break is associated with the DSO

eddies. In POP, the region where the high frequency signal is observed extends farther along the shelf than the region typically associated with DSO eddies; it is possible that the DSO eddies are generating TRWs in this simulation, but this mechanism has not been explored.

1.4 Discussion

In the Hovmöller diagrams (Figures 1.8A and 1.9A) we observed high-frequency signals that emanated from a location south of the Denmark Strait. These signals are comparable to the topographically trapped Rossby waves (Münchow et al., 2020) in a trough near the Fram Strait, to the cyclonic eddies formed at the Denmark Strait (Moritz et al., 2019), and to the coastally trapped shelf waves in this region (Gelderloos et al., 2021). A relative vorticity calculation shows, this high-frequency variability is consistent with DSO eddies traveling along the shelf break. We find that on average there is net on-shelf heat flux in POP and off-shelf heat flux in HYCOM, in the region where the eddies are present.

1.4.1 Eddy Contribution to Heat Flux

Using Equation 1.3, we can decompose the heat flux across the isobath into the total, mean, and eddy components. In this context, the “eddy" portion is the contribution to the total heat flux from processes with time scales between 2-30 days. In POP, the 2005-2009 average total heat flux onto the shelf in the DSO eddy region, from 102 to 499 km south of the Denmark Strait, is 58$\pm$14 PW. This is compared to 46$\pm$13 PW of total heat flux across the entire Wide Shelf region in POP. The eddy component of the heat flux in the DSO eddy region is 29$\pm$6 PW and 39$\pm$10 PW in the entire Wide Shelf; which corresponds to 51% and 85% of the total heat flux in both regions. In POP along the Wide Shelf the eddy component of the heat flux is significant and brings heat onto the shelf. This indicated that these high-frequency signals are an important component of the heat budget in this region.

In HYCOM, the 2005-2009 average total heat flux onto the shelf in the DSO eddy region, from 154 to 271 km south of the Denmark Strait, is -19 PW. Over the entire wide shelf region

the total heat flux is onto the shelf, 8.3 PW. The eddy contribution to the heat flux in the DSO eddy region is -2.5 PW which is just 13% of the total off shelf heat flux in that region. Along the entire Wide Shelf, the eddy heat flux is -8.0 PW, which opposes the mean heat flux and is similar in magnitude to the total heat flux onto the shelf. The DSO eddy signal is weaker in HYCOM and manifests itself in a smaller section of the shelf, which could be one reason the eddies do not result in the same contribution to cross-shelf heat flux as seen in POP.

The greater contribution of the mean flow to the total heat flux in HYCOM along the Wide Shelf region is consistent with the differences in surface speed and EKE (Figure 1.4C and F). Along the Southeast shelf, the core of the East Greenland current along the shelf break is stronger and less variable in HYCOM compared to POP. The high EKE region that corresponds to DSO eddy region is much stronger in POP, consistent with the eddies and associated impact on the heat flux being greater. Overall, on shelf heat fluxes in HYCOM along the Wide Shelf are associated with the mean flow, and in POP on shelf heat fluxes are the result the eddying flow.

Because there is a warm bias in the Wide Shelf temperature in POP, and a cold bias in HYCOM, it is possible that the POP simulation is over-representing the heat flux from the DSO eddies, and this process is being under-represented in HYCOM. These simulations do not have the resolution needed to fully resolve mesoscale eddies, and the role that these eddies play in cross-shelf heat flux may be clarified as they are better resolved. Advances in high-resolution modeling have shown that resolving these small-scale processes is important for understanding cross-shelf fluxes (Pennelly et al., 2019; Pennelly and Myers, 2020).

1.5 Conclusion

In order to assess the heat flux onto the Greenland Continental Shelf, we compared two eddy-permitting coupled ocean-sea ice simulations that employed different ocean components and atmospheric forcing. Using a continental shelf control volume subdivided into three regions, we determine not only how much heat crosses onto the shelf but also the patterns of transport on

the shelf. The region of greatest heat flux onto the shelf is between the Denmark Strait and the Sermilik Troughs in southeast Greenland, where the average heat flux is 16.4±13.8 TW in POP and 55.0±23.3 TW in HYCOM. Currents on the shelf are important in spreading warm water to different shelf regions; in both models the primary source of heat on the southwest continental shelf is from southward flux through the Cape Farewell Gate.

South of the Denmark Strait in both simulations we find a propagating signal in the vertically integrated heat flux with a periods of 3-7 days. This signal contributes to the on-shelf heat flux in this region in POP and the off-shelf heat flux in HYCOM. The location and frequency are consistent with DSO eddies, and the signal propagates along the shelf at the phase speed of a topographic Rossby wave. The section of the shelf along which the impact is most apparent in the heat flux is similar to the portion of the shelf where DSO eddies have been found in previous modeling studies. Further study of the formation of DSO eddies in these simulations is needed. The resolutions of both the 1/10° and 1/12° simulations limit the representation of the eddies. The difference in the strength and period of the eddies could be the result of the many differences in model configuration, such as: atmospheric forcing, bathymetry, or vertical coordinate systems. This study cannot fully separate those differences, but emphasizes the need for continued model intercomparison. The cross-shelf heat flux is just one component of volume budget for the continental shelf. We find the shelf is too cold in HYCOM and too warm in POP compared to observations from the MEOP program. Further study using higher resolution simulations that could better resolve the dynamics on the shelf could address the bias in on-shelf heat content.

One aspect of the dynamics of the Greenland continental shelf that has been neglected in this study is the role of ice sheet meltwater in these cross-shelf exchange mechanisms. Neither simulation includes a representation of GIS meltwater, which has implications for heat fluxes onto the shelf, as was explored by Gillard et al. (2020). The addition of meltwater from the ice sheet has been shown to strengthen currents and increase heat content on the West Greenland shelf within Baffin Bay (Castro de la Guardia et al., 2015; Grivault et al., 2017). Further simulations are needed to explore the implications of accelerated melting on shelf warming. In addition,

our study has shown that mesoscale processes contribute to on-shelf heat flux. High-resolution studies in this region are needed to better understand these processes. Such high-resolution studies could also address the dynamics between the shelf break and the ice sheets that bring the warm water we observe crossing the shelf to the front of glaciers where it drives melting.

Acknowledgments

T.J. Morrison, J.L. McClean and S.T. Gille were funded by DOE Office of Science grants: DE-SC0014440 and DE-SC0020073. D. Dukhovskoy and E.Chassignet were funded by the DOE award DE-SC0014378 and HYCOM NOPP (award N00014-15-1-2594). The HYCOM-CICE simulations were supported by a grant of computer time from the DoD High-Performance Computing Modernization Program at NRL SSC. The POP/CICE simulation was run with a National Center for Atmospheric Research Climate Simulation Laboratory (CSL) allocation on Yellowstone (ark:/85065/d7wd3xhc), sponsored by the National Science Foundation. Some POP/CICE analyses were carried out using Rhea in the Oak Ridge Leadership Computing Facility at the Oak Ridge National Laboratory. The marine mammal data were collected and made freely available by the International MEOP Consortium and the national programs that contribute to it. (http://www.meop.net). We thank Mathew Maltrud (LANL) for preparing the sea ice initial condition used in the POP/CICE simulation. We thank André Palóczy for advice on the calculation of heat fluxes in POP. We also thank the anonymous reviewers for their recommendations.

Chapter 1, in full, has been submitted for publication of the material as it may appear in Journal of Geophysical Research: Oceans, 2022, Morrison, Theresa; Dukhovskoy, Dmitry; McClean, Julie; Gille, Sarah; Chassignet, Eric. The dissertation author was the primary investigator and author of this paper.

Chapter 2

Sensitivities of the West Greenland Current and Central Labrador Sea to Greenland Ice Sheet Meltwater in a Mesoscale Ocean/Sea ice Model

2.1 Introduction

Mass loss from the Greenland Ice Sheet (GIS) has been a major contributor to sea level rise and is projected to continue for the next century (Pattyn et al., 2018). Between 1992 and 2018 the GIS lost 3,902$\pm$342 billion tonnes of ice (The IMBIE Team, 2020); roughly half of that loss is attributed to increased atmospheric driven melting that produces freshwater runoff. Glacial fjords connect the GIS to the continental shelf and are locations where both solid discharge and liquid runoff can enter the ocean. In general fjords are long (50-100 km), narrow (5-10 km), and deep (100s m), but each has a unique geometry that is important for its dynamics (Straneo and Cenedese, 2015a; Carroll et al., 2016; Zhao et al., 2021). In some fjords, buoyant plumes form where subglacial discharge enters the ocean at the base of glaciers entraining the ambient water masses within the fjord producing "glacially modified water". Observations from Beaird et al. (2018b) found that the glacially modified water that was exported from Sermilik fjord was comprised of 88% Atlantic Water (See also, Beaird et al., 2015, 2017). Icebergs that calve off the front of the glacier terminus also distribute meltwater at depth within fjords (Moon et al.,

2018). As a result of the multitude of mixing processes within fjords, ice sheet runoff is modified before it is exported out of the fjord.

The transport of meltwater into the Labrador Sea is of particular interest because the region is one location where deep convection occurs in the Subpolar North Atlantic (SPNA). In the winter, cooling of saline surface water results in convective instabilities and the development of very deep mixed layers; in the spring, the upper water column rapidly restratifies. Winter winds also contribute to convection by destabilizing the boundary currents (Straneo et al., 2002; Cuny et al., 2005). Buoyancy advection by the wind can be one-third the size of the surface buoyancy fluxes in the Labrador Current, indicating that this contribution to deep water formation should not be neglected (Straneo et al., 2002). Deep convection has also been observed in the Irminger and Nordic Seas (Petit et al., 2020; Chafik and Rossby, 2019; Desbruyères et al., 2019). The deep convection in the Labrador Sea is thought to contribute to the variability of the Atlantic Meridional Overturning Circulation (AMOC) (Lohmann et al., 2014; Marshall and Schott, 1999) which transports heat northward in the upper ocean and southward in the deep ocean. The northward heat transport of the AMOC is critical to maintaining the climate of the Northern Hemisphere. Projections of the future climate under anthropogenic forcing have indicated the potential for a decline in AMOC strength; see Weijer et al. (2019) for a review of this topic. The shift away from the paradigm of deep convection and NADW formation occurring primarily in the Labrador Sea has been furthered by the results of the Overturning in the Subpolar North Atlantic Program (O-SNAP) (Lozier et al., 2019; Desbruyères et al., 2019) and other recent observations (Chafik and Rossby, 2019). These observations cover a relatively short period considering the long timescales associated with AMOC variability and stand in contrast to ocean modeling studies that show deep convection in the Labrador Sea contributes to AMOC variability (Yeager et al., 2021). This work is motivated by the potential role of GIS meltwater in reducing deep convection in the Labrador Sea and subsequently weakening the AMOC.

The regional circulation of the SPNA is defined by the confluence of warm salty water masses from the Subtropics and cold fresh water masses from the Arctic. Warm, saline water

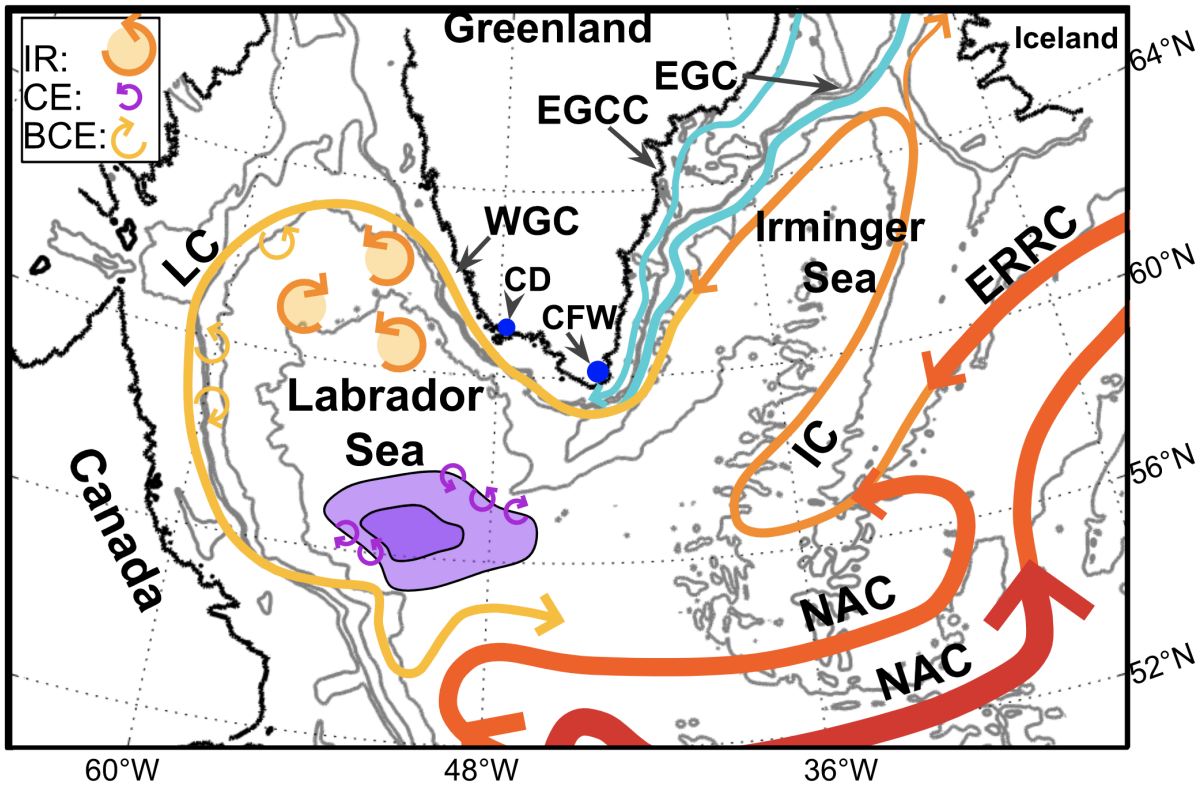

Figure 2.1. Schematic of circulation in the Subpolar North Atlantic Ocean; isobaths are plotted at 400, 800, 2000, and 3000 m. Major currents are labeled: North Atlantic Current (NAC), East Reykjavik Ridge Current (ERRC), Irminger Current (IC), East Greenland Current (EGC), East Greenland Coastal Current (EGCC), West Greenland Current (WGC), and Labrador Current (LC). The deep convection region is shown in purple. Cape Farewell (CFW) and Cape Desolation (CD) are indicated by blue dots. The approximate locations of Irminger Rings (IR), Convective Eddies (CE), and Boundary Current Eddies (BCE) are indicated. Holliday et al. (2018, After) with additions from Sutherland and Pickart (2008); Håvik et al. (2017); Rossby et al. (2018); Rieck et al. (2019)

from the subtropics is advected northward from the Gulf Stream in the North Atlantic Current (NAC). The eastern branches of the NAC extend into the Nordic Seas, and the western branches form the Irminger Current (IC) (Holliday et al., 2018). The IC retroflects south of the Denmark Strait and flows south along the Greenland continental shelf break. The East Greenland Current (EGC) flows southward along the shelf break from Fram Strait to Cape Farewell (CFW in Figure 2.1) transporting relatively cold fresh water and sea ice from the Arctic. The weaker and narrower East Greenland Coastal Current (EGCC) is present onshore of the EGC both north and south of the Denmark Strait (Håvik et al., 2017; Sutherland and Pickart, 2008; Foukal et al., 2020). South of the Denmark Strait, the EGC is inshore of the IC; at Cape Farewell, the EGC and IC merge and turn northward to flow along the western Greenland shelf, forming the West Greenland Current (WGC). The EGCC remains farther on-shore and becomes the West Greenland Coastal Current (Pacini et al., 2020). The WGC meanders and produces eddies near Cape Desolation (CD in Figure 2.1) (Pacini and Pickart, 2022). As the WGC approaches the Davis Strait, the shelf slope flattens, and there is a region of high eddy activity.

Within the Labrador Sea, mesoscale eddies are generally subdivided into three categories: Irminger Rings, Boundary Current Eddies, and Convective Eddies. Irminger Rings (IR) are large (30-60 km), long-lived (1-2 years) eddies that transport warm Irminger Sea water (Lilly et al., 2003). IRs are shed from the WGC near Cape Desolation where steep bathymetry produces instabilities (Eden and Böning, 2002; Chanut et al., 2008). These eddies are thought to have a restratifying effect on the Labrador Sea (Chanut et al., 2008), though it is possible that they do not travel far enough south to interact with the convective region (Rieck et al., 2019). Boundary Current Eddies (BCE) form in the boundary currents, namely the WGC and LC (Eden and Böning, 2002; Brandt et al., 2004; Chanut et al., 2008). BCEs are the result of baroclinic instabilities and are surface intensified. These eddies are smaller than IRs (10 km) and do not tend to propagate into the central Labrador Sea. Convective Eddies (CE) are small eddies (10-35 km) that form at the margin of the convective region where horizontal density gradients are strong (Marshall and Schott, 1999; Rieck et al., 2019). CEs are thought to play a role in the

rapid restratification of the convective area through lateral buoyancy fluxes (Jones and Marshall, 1997; Rieck et al., 2019). Mesoscale eddy processes have been shown to modify deep convection with the Labrador Sea in ocean simulations that resolve eddies (Chanut et al., 2008; Tagklis et al., 2020; Pennelly and Myers, 2020). In particular, Tagklis et al. (2020) found that by increasing the horizontal resolution of the model to be first mesoscale resolving and then submesoscale resolving, the convection volume was reduced by 50% and by 80%, respectively.

The transport of freshwater off the southwest Greenland continental shelf has been linked to the winds (Luo et al., 2016; Schulze Chretien and Frajka-Williams, 2018) and eddies (Bracco et al., 2008; De Jong et al., 2014; Katsman et al., 2004) in both modeling and observational-based studies. A comparison of ocean eddying (1/12°) and non-eddying (1/4°) simulations found that polar water is exported out of the boundary current system along the West Greenland Shelf, suggesting that this is the location where meltwater from the GIS will enter the interior basin regardless of where along the continent it enters the ocean (Pennelly et al., 2019). Schulze Chretien and Frajka-Williams (2018), using a Lagrangian approach, showed that the majority of upper ocean (0-100 m) freshwater ($S_{ref} = 34.95$) enters the Labrador Sea in the upper 30 m; transports inferred from simulated salinity profiles at the shelf break showed 1.5 mSv ($S_{ref} = 34.95$) entering the basin over this depth range. Similarly, in an eddying (2.5 km) ocean model, winds drove the off-shelf transport of meltwater at the shelf break (500-1000 m), while the large-scale circulation and eddies advected the meltwater farther into the basin (Castelao et al., 2019). Late summer and early fall have been identified in several studies as the peak period of off-shelf freshwater transport (Castelao et al., 2019; Gou et al., 2021; Majumder et al., 2021).

The pathways and spread of meltwater in the SPNA have been explored with models using passive tracers. Chassignet et al. (2016) tracked Greenland meltwater in a pair of ocean simulations where mesoscale eddies were either explicitly resolved or parameterized; they found that in the lower resolution simulation the transport of meltwater into the interior basin was weaker. Gillard et al. (2016), using an 1/12° eddy-permitting ocean model, found that meltwater from West Greenland tends to enter Baffin Bay, while melt from East Greenland generally enters

the Labrador Sea. Further, Luo et al. (2016) estimate that 50-60% of runoff from southeast Greenland enters the northern Labrador Sea in a 2.5 km eddy-resolving ocean model. Similarly, results from a non-eddying 2.4° ocean model showed that the AMOC was most sensitive to the addition of meltwater in East Greenland waters (Yu et al., 2016).

We investigate the impact of GIS meltwater on freshwater transport into the Labrador Sea because freshening of the Labrador Sea could inhibit deep convection which, in turn, could potentially weaken the AMOC. We compare global coupled ocean/sea-ice simulations that do or do not resolve the mesoscale dynamics of the Labrador Sea. The inclusion of mesoscale eddies in the Labrador Sea shifts the deep convection zone southward and closer to the Labrador shelf break. We use the mesoscale eddying model to investigate the off-shelf transport of freshwater at the southwest Greenland shelf break. We find that vertically diluted GIS meltwater amplifies overall off-shelf freshwater transport implying that the Labrador Sea freshwater content may be more sensitive to GIS meltwater than previously suggested.

In this chapter we present a comparison of four coupled ocean/sea-ice simulations. A description of the model setup, GIS meltwater forcing, and transport definitions is given in Section 2.2. In Section 2.3.1 we compare the lower and high resolution simulations. In Section 2.3.2 we compare the impact of the GIS meltwater forcing schemes. The changes in energy conversion are discussed in Section 2.3.3.

2.2 Methods

2.2.1 Model Description

In this study, we present results from four global couple ocean/sea-ice simulations forced with atmospheric reanalysis. All four simulations use the same ocean and sea-ice model code and the same atmospheric forcing. The suite of simulations includes a pair where both the horizontal and vertical resolution is higher in one grid relative to the other and neither has a representation of land ice melt. The other two simulations are configured on the higher resolution grid and have

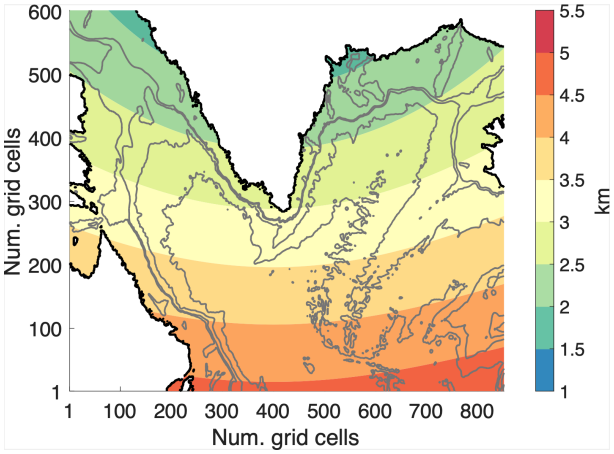

Figure 2.2. Map of model bathymetry (400, 800, 2000, and 3000 m isobaths) within our region of interest plotted on the native model grid. The number of grid points are shown on the x and y axes. The square root of the grid cell area (km) at each point is shown in color.

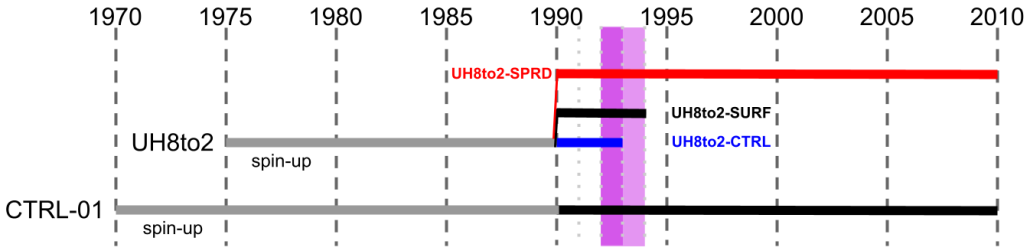

Figure 2.3. Diagram showing the timeline of the four model runs: CTRL-01, UH8to2-CTRL, UH8to2-SPRD, and UH8to2-SURF. The solid gray line indicates the spin-up period for each simulation. The purple area represents the UH8to2-SPRD and UH8to2-SURF comparison period, the dark purple highlighting 1992 which is the year all four simulations can be compared.

different representations, but the same total volume, of land ice melt. With these simulations we can assess the impact of increased horizontal and vertical resolution on the Southwest Greenland Shelf-break region and the sensitivity to the vertical dilution of meltwater.

All four simulations used in this study were produced using the Energy Exascale Earth System v0-HiLat (E3SMv0-HiLAT ; Hecht et al., 2019) model which utilizes the Parallel Ocean Program 2 (POP2; Dukowicz and Smith, 1994) for the ocean component and the Community Ice Code version 5 (CICE5; Hunke et al., 2010) for the sea ice component. The HiLat code is a derivative of the Community Earth System Model version 1 (Hurrell et al., 2013). The corrected interannually varying Coordinated Ocean-ice Reference Experiment-II (CORE-II CIAF; Large and Yeager, 2009) forcing from 1970-2009 was used as the atmospheric forcing. The 30-arc second General Bathymetric Chart of the Oceans (GEBCO; Weatherall et al., 2015) product was used for the model bathymetry.

Three of the four simulations were configured to be globally mesoscale eddy resolving in the basins by using an "ultra-high" horizontal resolution tri-polar grid that has horizontal spacing of 8 km at the equator and 2 km at the poles; thus it is referred to as the UH8to2 grid. The Northern Hemisphere poles are located in Siberia and Greenland, hence the horizontal resolution is $\sim$2–3 km in the western SPNA (Figure 2.2). POP2 uses z-level coordinates; the UH8to2 consists of 60 vertical levels that are non-uniformly spaced with 10 m resolution in the upper 160 m and 250 m resolution close to the ocean floor; the maximum depth is 5500 m. Partial bottom cells (PBCs) are used to more smoothly represent the bathymetry.

The fourth simulation is an analogous E3SMv0-HiLAT simulation on a 0.1° tri-polar grid, with a horizontal resolution of $\sim$5–6 km in the western SPNA. Unlike the UH8to2, the 0.1° tri-polar grid does not have a pole in Greenland instead the poles are in North America and Asia. This simulation has 42 non-uniform vertical levels with 10 m resolution at the surface and 250 m at depth, and PBCs are used.

The ocean component of the UH8to2 simulations was initialized from a two-month stand-alone POP integration, which, in turn, was initialized from rest using potential temperature

and salinity from the Polar science center Hydrographic Climatology 0.3 (PHC 0.3; Steele et al., 2001). The sea ice state was initialized using a 2 m uniformly thick region of sea ice, with the ice edge defined by the January climatological mean from satellite (Special Sensor Microwave/Imager) observations. The 0.1° configuration is spun up from 1970-1990 while the UH8to2 configuration is spun up from 1975-1990, see Figure 2.3. The simulations begin in different years in part because of the enormous computational cost of running the UH8to2 simulation.

The CORE-II CIAF forcing does not include an explicit representation of the meltwater from the Greenland or Antarctic Ice Sheets. In the Southern Ocean, the multi-year mean climatology of ice sheet melting, iceberg calving and tracking, and river runoff from Hammond and Jones (2016) is used to represent the fluxes from the Antarctic Ice Sheet. It is distributed over the Antarctic shelf and slope and the interior deep basin, based on observed trajectories of large icebergs. We utilize the estimates of freshwater fluxes from the GIS reported by Bamber et al. (2018). These fluxes are monthly varying and are on a 5 km grid. We consider the solid discharge and liquid runoff from the GIS to be the meltwater and treat the terms in the same way. Additionally, we mask any river runoff from the CORE-II CIAF forcing over Greenland (Dai and Trenberth, 2002) and replace it with the tundra runoff component from Bamber et al. (2018). During the spin-up period, neither meltwater nor tundra runoff were added to the ocean model. Meltwater is added via a virtual salt flux and has no associated thermal forcing. A dye tracer is added proportionally to the volume of meltwater added and is used to track the spread of runoff throughout the simulation.

Our study focuses on the simulation of results from 1992 and 1993 (Figure 2.3). Daily averages of the model fields were saved during 1992. The choice of the comparison period was primarily the result of the constraints imposed by the huge computational cost of running these simulations. Both years are in the early 1990s, when runoff from the GIS was relatively low, see Bamber et al. (2018). Furthermore, both the winters of 1992/93 and 1993/94 are during the relatively strong positive phases of the North Atlantic Oscillation (NAO) (Pickart et al.,

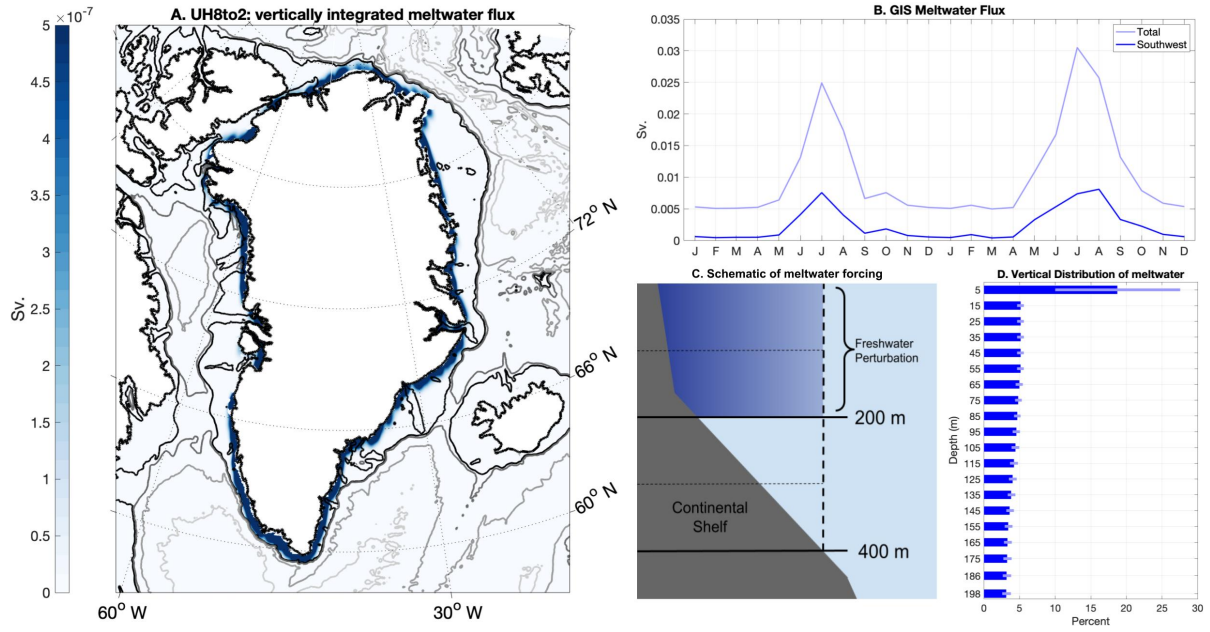

Figure 2.4. (A) Vertically integrated meltwater forcing for July 1992 showing the spatial pattern on the UH8to2 grid. (B) Time series of meltwater flux for the entire GIS (light blue) and the southwest shelf (dark blue, shown in Figure 2.7). (C) Schematic showing the vertical and cross-shelf structure of the meltwater forcing. (D) Average percentage of meltwater added to each model layer, depth indicates the midpoint of each model layer. Light blue bars are the 20th-80th percentile range over the period 1991-1999.

2002). However, as we are comparing simulations with the same atmospheric forcing we think this limitation is acceptable to understand the sensitivity of the ocean to the vertical dilution of meltwater.

2.2.2 Greenland Meltwater Forcing Description

We perform three experiments with the UH8to2 grid to assess the sensitivity to the vertical dilution of meltwater from the GIS within glacial fjords. The fourth experiment is performed on the 0.1° grid, includes no meltwater, and is referred to as the CTRL-01. Together these experiments allow us to assess both the impacts of resolving the mesoscale and the dilution of meltwater within fjords. Figure 2.3 provides a summary of the four case configurations.

The primary simulation in the UH8to2 sensitivity suite is the "Spread Case" or UH8to2-SPRD which is run from 1990-2004 (will be run through 2009) after being branched off the

UH8to2 spin-up (1975-1990), see Figure 2.3. In the UH8to2-SPRD simulation, meltwater from the GIS is vertically distributed over the upper 200 m of the water column. This is motivated by the observations of Beaird et al. (2018b) that showed using noble gas samples that meltwater from the GIS could be found at depth in a glacial fjord. Figure 2.4B shows a schematic of the method for distributing meltwater vertically and Figure 2.4C shows the percentage of the total melt added to each model level for August 1992. In contrast, the "Surface Case" or UH8to2-SURF, also branched off the UH8to2 spinup, is run from 1990-1993, and, as in previous Greenland meltwater perturbation studies, all meltwater is added to the surface layer of the model (10 m). In both the UH8to2-SPRD and UH8to2-SURF simulations, the tundra runoff is added to the surface layer of the model. The UH8to2 spin-up run is continued from 1990-1992 with no meltwater added; it is referred to as the UH8to2 Control (UH8to2-CTRL) simulation.

For the two meltwater perturbation experiments, the meltwater fluxes from the Bamber et al. (2018) data are remapped point-by-point onto the nearest ocean grid point on the UH8to2 grid. At every location, a horizontal Gaussian filter with a length scale of $\sim$14 km is applied to distribute the meltwater horizontally. However, a mask is used to ensure that meltwater is not added to areas deeper than 400 m in order to keep the meltwater confined to the shelf. Figure 2.4A shows a map of the August 1992 meltwater forcing on the UH8to2 grid with the Gaussian smoothing applied. For the adjustment period 1990-1991 the total runoff from the GIS added to the model is 1,649 km^3; in the comparison period, 1,383 km^3 of meltwater are added.

2.2.3 Water mass metrics: Comparison to AR07 Line

Limited observations are available for comparison from 1992 or 1993 to assess the relative accuracy of the UH8to2-SURF and UH8to2-SPRD cases. We compare our simulations to the World Ocean Circulation Experiment (WOCE) AR07W data collected in June 1993 (Jones and Lazier, 2007). Potential temperature and salinity profiles were extracted from the June 1993 monthly average at the model grid cell closest to where the observation was collected. The simulation is warmer than the observations throughout the transect. The WGC and LC are more

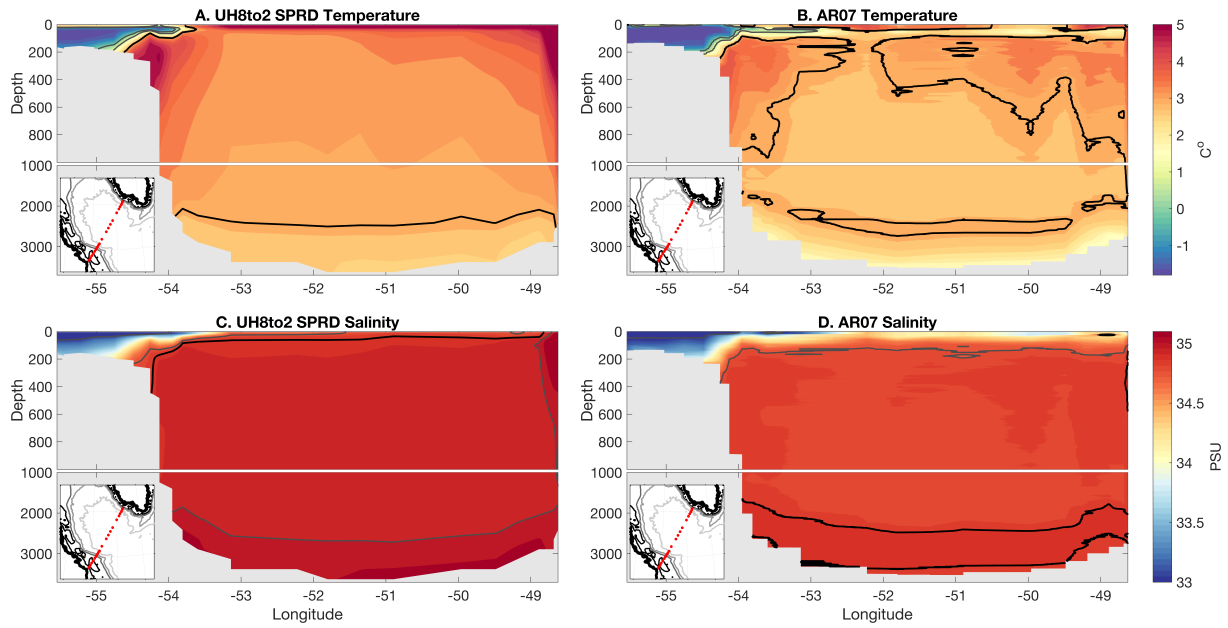

Figure 2.5. Sections of potential temperature (A and B) and salinity (C and D) for the UH8to2-SPRD (A and C) and the AR07W line (B and D). In set maps show where observations were collected. The 0°, 1°, and 3°C isotherms are in gray; the 5°C isotherm is in black. The 33, 34.8, 35 isohalines are in gray; the 34.9 isohaline is in black.

than 2°C warmer in the UH8to2 simulation. In the Labrador basin, beneath the surface layer, the difference in model and observations is less than 1°C. The WGC and LC are similarly more saline in the simulations (roughly 0.5 PSU) compared to observations.

2.2.4 Energy conversion and cross-shelf transport formulations

We compare our suite of four simulations to investigate the combined effect of resolving mesoscale eddies and GIS meltwater on the Labrador Sea. With the lower (CTRL-01) and higher (UH8to2) resolution simulations described above, we examine the impact of increased horizontal resolution on deep convection and eddy generation along the Southwest Greenland shelf break. With the three higher (UH8to2) resolution simulations we compare deep convection, eddy generation, and off-shelf transport of freshwater under the two Greenland meltwater forcing representations. In this section, the definitions used for the energy conversion terms and cross isobath transports are given.

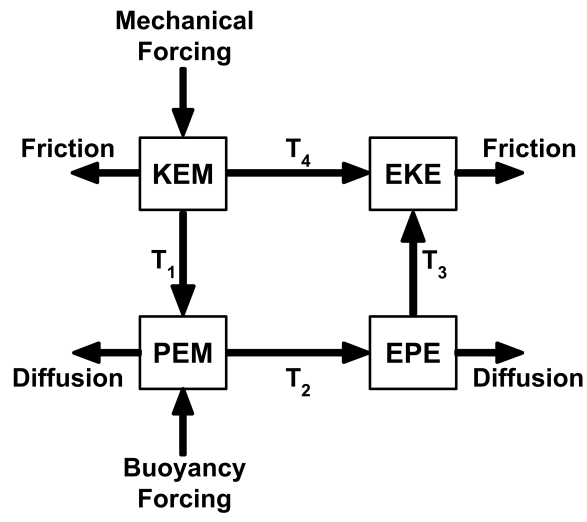

Figure 2.6. Diagram showing the components of the oceanic energy budget. After Böning and Budich (1992)

We consider changes to the eddy generation terms of the ocean energy budget both in the context of enhanced resolution and meltwater forcing. Following the approach of (Böning and Budich, 1992), the terms of the energy budget are defined assuming that horizontal density gradients are much less than the stratification and that the contribution of the vertical velocity can be neglected. This decomposition of the energy budget has been used for ocean models of varying complexity (see Eden and Böning, 2002; Trodahl and Isachsen, 2018; Rieck et al., 2019; Stewart et al., 2019, and others) A diagram of the ocean energy cycle is shown in Figure 2.6 which illustrates the sources (mechanical and buoyancy forcing) and sinks (friction and diffusion) as well as the conversions between mean and eddy components. Buoyancy forcing influences the mean available potential energy (PEM) which can be converted to eddy available potential energy (EPE) through baroclinic instability. The mean kinetic energy (KEM) is converted to EKE through barotropic instability; the transfer between these two terms more generally represents the work of the Reynolds stresses against the mean shear (Böning and Budich, 1992).

The EKE is defined as:

$$EKE = \frac{1}{2}\overline{\left(u'^2 + v'^2\right)}. \tag{2.1}$$

where the daily averages of the zonal and meridional velocity are u and v, respectively. The eddy component is defined as $u' = u - \overline{u}$, where $\overline{u}$ is the annual average of u, similarly for the meridional velocity. Eddies are identified by closed contours of relative vorticity, $\zeta = \partial v/\partial x - \partial u/\partial y$ which maybe nondimensionalized by dividing by the Coriolis parameter f. The absolute value of the non-dimensional relative vorticity is the Rossby number. The EPE is defined as:

$$EPE = \frac{1}{2}\frac{\overline{(\rho'^2)}}{N}. \tag{2.2}$$

For a closed volume, we can quantify these transfer terms; the baroclinic conversion is:

$$T_2 = -\rho_0 \left(\frac{g}{N\rho_0}\right)^2 \left(\overline{u'\rho'}\frac{\partial \overline{\rho}}{\partial x} + \overline{v'\rho'}\frac{\partial \overline{\rho}}{\partial y}\right) \tag{2.3}$$

where ρ_0 is the reference density and N^2 is an annual mean Brunt-Väisälä frequency (Rieck et al., 2019). The anomalies in velocity and density are deviations of the daily average from the annual mean, as described above. The barotropic transfer term is given by:

$$T_4 = -\rho_0 \left(\overline{u'^2}\frac{\partial \overline{u}}{\partial x} + \overline{u'v'}\left(\frac{\partial \overline{u}}{\partial y} + \frac{\partial \overline{v}}{\partial x}\right) + \overline{v'^2}\frac{\partial \overline{v}}{\partial y}\right). \tag{2.4}$$

Without a complete energy budget, these terms can provide only a qualitative insight into the energy conversion.

We define two sections along the Southwest Greenland continental shelf break to quantify the cross-shelf transport. Figure 2.7 shows the bathymetry and southwest shelf control volume. The intention behind subdividing the shelf in this way it to separate the higher and lower eddy active zones. The shelf break contour is located roughly along the 500 m isobath.

We define the volume transport as

$$V = \int_H^0 \int_0^L \hat{v}\, dx\, dz, \tag{2.5}$$

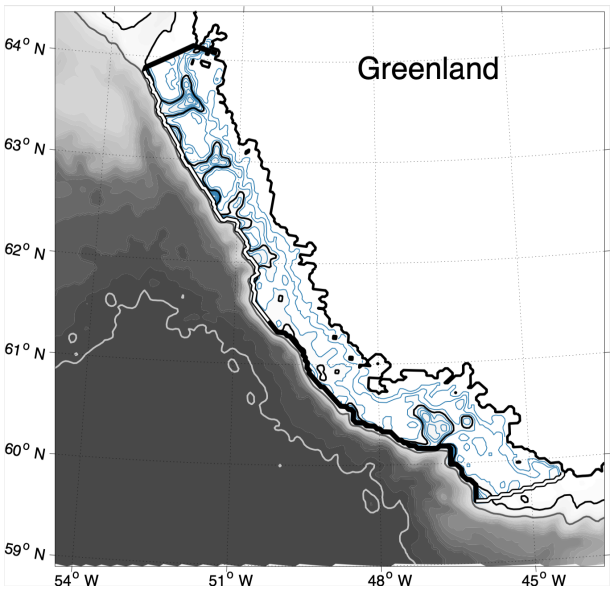

Figure 2.7. The Southwest Greenland Shelf with the control volume region indicated by blue contours. The southern part of the shelf break is in black, the northern part of the shelf break is in white.

where x is the along-shelf direction and $\hat{v}$ is the cross shelf velocity, H is the depth, and L is the length along the shelf break. The positive direction is defined as into the basin; positive fluxes indicate volume flux into the Labrador Sea.

The freshwater transport is

$$FWT = \int_H^0 \int_0^L \frac{(S - S_{ref})}{S_{ref}} \hat{v}\, dx\, dz, \tag{2.6}$$

where $S_{ref} = 34.7$, which is the reference salinity used in POP.

A dye tracer is added proportionally to the virtual salt flux and has units of g/kg. We can calculate the transport of this tracer as

$$MWT = \int_H^0 \int_0^L \mu(x,z,t)\hat{v}\, d\hat{x}\, dz, \tag{2.7}$$

where μ is the dye tracer concentration. Dye tracer concentration can be converted to meltwater volume by reversing the conversion of meltwater volume flux to virtual salt flux. Meltwater

content (MWC) is

$$MWC = \frac{\mu}{\rho_{FW} S_{ref} \mathrm{FWF}_{factor}} \tag{2.8}$$

where ρ_{FW} is the density of freshwater (1 g/cm^3) and $\mathrm{FWF}_{factor} = 1 \times 10^{-4}$ (cm/s) (msu/psu) / (kg/m^2/s). Meltwater content represents the fraction of meltwater in a given grid cell and is integrated to find the meltwater volume.

2.3 Results

We start our analysis by comparing the large-scale upper-ocean mean current structure and eddy kinetic energy (EKE) patterns of the Labrador Sea in our lower (CTRL-01) and higher (UH8to2) resolution simulations. As well, winter (January February, March) mixed layer depth (MLD) is calculated for the four simulations (Large et al., 1997). We calculate eddy conversion terms to understand how both enhanced horizontal resolution and vertical dilution of meltwater may contribute to a change in eddy production. Finally, the transports of volume, freshwater, and dye tracer (a proxy for meltwater) are calculated across an along-shelf section of the southwest Greenland continental shelf.

2.3.1 Comparison to Eddy Permitting Resolution

Speed and Eddy Kinetic Energy

Current speed in the upper 50 m of both the UH8to2-CTRL and CTRL-01 simulations is shown in Figure 2.8A and B. In both simulations, the EGCC and EGC/IC are visible along the southeast continental shelf break. As these currents round Cape Farewell they form the WGCC and WGC and remain as distinct currents as they approach Cape Desolation, similarly to observations (Pacini et al. (2020)). The cores of the EGC/IC and WGC (north of Cape Desolation) are narrower in the UH8to2 simulation compared to the CTRL-01. Figure 2.9 shows these thinner cores on either side of Cape Farewell; additionally, they are located further onshore of those in the CTRL-01. Sections of the 1992 annual mean model speed in the upper 50 m

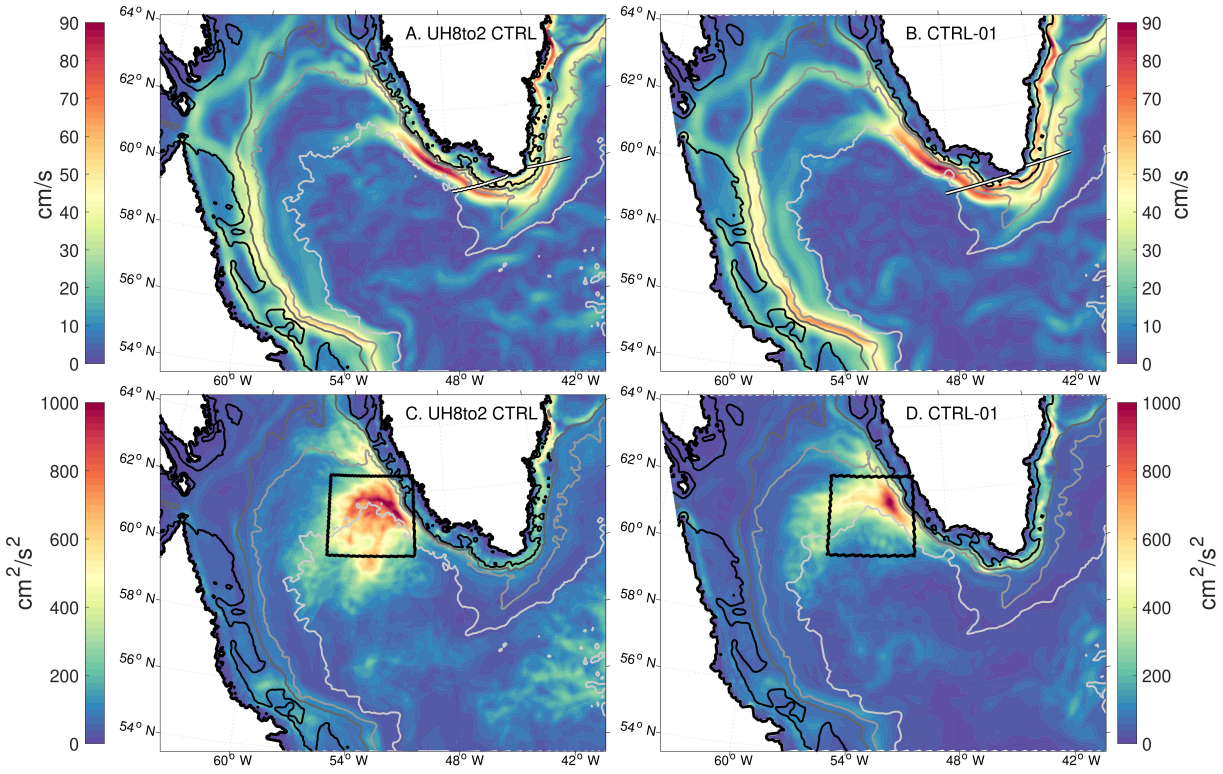

Figure 2.8. Average (1992) speed (cm/s) in the top 50m for the UH8to2-CTRL (A) and CTRL-01 (B) cases, average (1992) EKE (cm^2/s^2) in the top 50m for the UH8to2-CTRL (C) and CTRL-01 (D) cases. The 400, 800, 2000, and 3000 m isobaths are plotted from dark to light gray. At Cape Farewell, white lines indicate the cross-shelf transects through the EGC and WGC, the black box indicates the high EKE region.

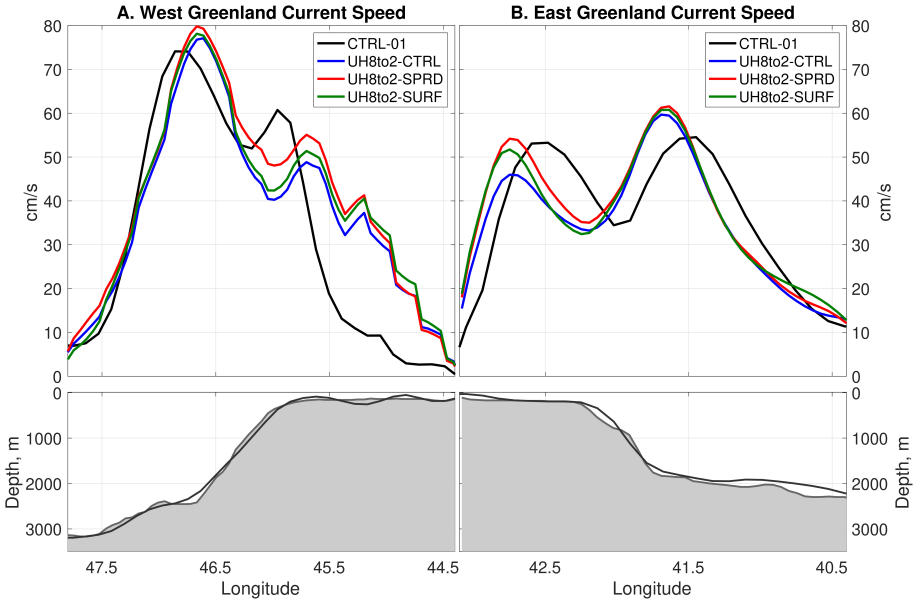

Figure 2.9. Average (1992) speed (cm/s) in the top 50m and model bathymetry along the cross-shelf transects shown in Figure 2.8. The left column is across the West Greenland shelf and the right column is for the East Greenland shelf. All four simulation results are represented: CTRL-01 (black), UH8to2-CTRL (blue), UH8to2-SPRD (red), and UH8to2-SURF (green). In the lower row, the UH8to2 bathymetry is shaded in gray with the CTRL-01 bathymetry plotted as black line.

are compared across the four simulations; the local shelf slope bathymetry is also plotted. The EGCC and EGC/IC have roughly the same speed in the CTRL-01 simulations, but the EGC/IC is ∼5-15 cm/s faster than the EGCC in the UH8to2 simulations. The speeds of the EGCC and EGC/IC in all simulations are similar to observations from (Le Bras et al., 2018). The EGCC and EGC/IC difference is smallest in the UH8to2-SPRD since the EGCC and WGCC are accelerated in the cases with freshwater forcing. The distinction between the WGCC and WGC is less clear than the EGCC and EGC/IC separation. The WGCC is fastest in the UH8to2-SPRD case, indicating an acceleration with the addition of meltwater. The speed of these currents is greater than those reported by Pacini et al. (2020), but we note that their velocity is rotated into the along-shelf direction while the model velocities are oriented zonally and meridionaly.

The 1992 average EKE in the upper 50 m of the UH8to2-CTRL and CTRL-01 simulations is plotted in Figure 2.8 C and D. The black box encloses the area of high EKE between 60°-62.5°N and 50°-55.5°W in both models. In the CTRL-01 simulation, the locus of high EKE is close to the shelf break between the 2,000 m and 3,000 m isobaths. The area of elevated EKE does not extend south into the interior Labrador Sea (deeper than the 3,000 m isobath) but extends farther west. In the UH8to2-CTRL case the area of EKE above 600 cm^2/s^2 is more expansive and fills the box. The southward extension of high EKE in the UH8to2 simulation is qualitatively similar to estimates of EKE from altimetry (Brandt et al., 2004; Lilly et al., 2003). The average EKE within the defined box in the CTRL-01 simulation (Figure 2.8D) is 328 cm^2/s^2 compared to 525 cm^2/s^2 in the UH8to2-CTRL case. This amounts to a 60% increase in the average EKE in that region when using the UH8to2 grid. The UH8to2-SURF and UH8to2-SPRD cases have an average EKE of 557 cm^2/s^2 and 571 cm^2/s^2, respectively (not shown). The second region of elevated EKE along the West Greenland shelf break, between 62.5°-64°N is also more energetic in the UH8to2-CTRL simulation compared to the CTRL-01 (Figure 2.8C and D).

Informed by the map of average EKE for the UH8to2-SPRD simulation, we focus on the properties of a single eddy that we classify as an IR; it is located at approximately 60.7°N and 55°W, which is near the western edge of the elevated EKE box. Figure 2.10 shows the

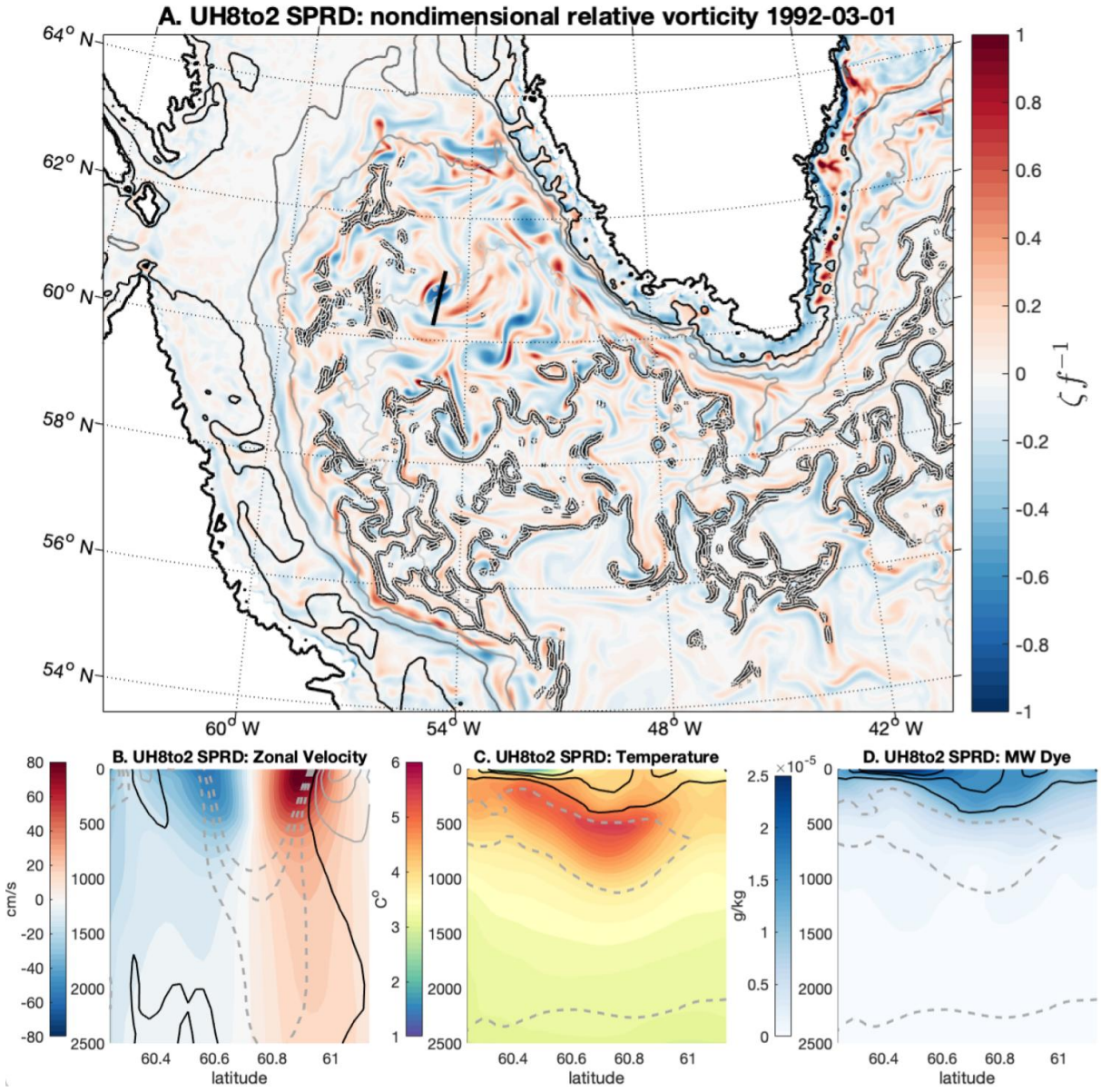

Figure 2.10. (A) Non-dimensional relative vorticity at 50 m for the UH8to2-SPRD simulation from the daily averaged velocity from 1992-03-01. The 1500 m contour of mixed layer depth is plotted in white and outlined in black while the 400, 800, 2000, and 3000 m isobaths are plotted from dark to light gray. The black line in the northern Labrador Sea shows where the cross eddy transect panels (B-D). Panel B shows the zonal velocity with contours of non-dimensional relative vorticity in 0.1 intervals from -0.3 to 0.3 (gray dashed less than zero), $\zeta f^{-1} = 0$ is the black contour. Panel C shows the potential temperature (°C) and contours of salinity (black: 34.7,34.8,34.9; gray: 35, 35.1, 35.2, 35.3). Panel D shows the dye tracer concentration (g/kg $\times$ 10^{-5}) in the eddy with the same salinity contours as Panel C

nondimensional relative vorticity and properties of this example IR. Other large cyclonic features can be identified in the northern Labrador Sea. The 1,500 m mixed layer depth contour from the same day is also plotted in Figure 2.10A and the small features near its edge are indicative of CEs. Sections through the eddy show the associated zonal velocity (Figure 2.10B), temperature (Figure 2.10C), and meltwater dye tracer Figure (2.10D). The structure of this IR is similar to the simulated eddy of Rieck et al. (2019) and observations (Hátún et al., 2007; De Jong et al., 2014). The warm core is located at 500 m and has a maximum temperature of about 5° C. The eddy is somewhat asymmetrical with the fresh cap located south of the deep warm core. The meltwater dye tracer is primarily located in water fresher than 34.9 and is closely linked to salinity. The 34.9 isohaline is deepest in the core of the eddy, about 400 m, and similarly there is a greater concentration of the meltwater dye tracer at depth within the eddy compared to the surrounding water. This finding indicates that IRs transport meltwater into the interior of the Labrador Sea.

A comparison of the baroclinic and barotropic conversion terms in the UH8to2-CTRL and CTRL-01 can provide insight into what processes result in the difference in EKE between the two simulations. Figure 2.11 shows the 1992 average of the T_2 and T_4 terms in the upper 230 m of both simulations. Since we do not formally close the energy budget, these terms should only be interpreted as an approximation of the transfer of energy from mean to eddy components. In the UH8to2-CTRL case over the continental shelf, T_2 is the dominant term. The strength of the baroclinic conversion is nonuniform and indicates a strong dependence on bathymetry. There are three "hot-spots" of barotropic conversion off the shelf. These patches are oriented parallel to the shelf break and extend from $\sim$60°-61.5°N, $\sim$62°-63°N, and $\sim$63°-64°N. The southernmost patch is the strongest and falls along the eastern edge of the high EKE box. In the CTRL-01, the baroclinic conversion term is strongly negative along the shelf break in contrast to the UH8to2-CTRL. Negative values of T_2 indicate energy flux from EPE to PEM. However, the isolated patches of strong baroclinic conversion suggests this process does occur in the CTRL-01 simulation. Barotropic conversion in the CTRL-01 has a similar spatial pattern to the UH8to2-CTRL case but is weaker overall. In the WGC eddy shedding zone T_4 more than

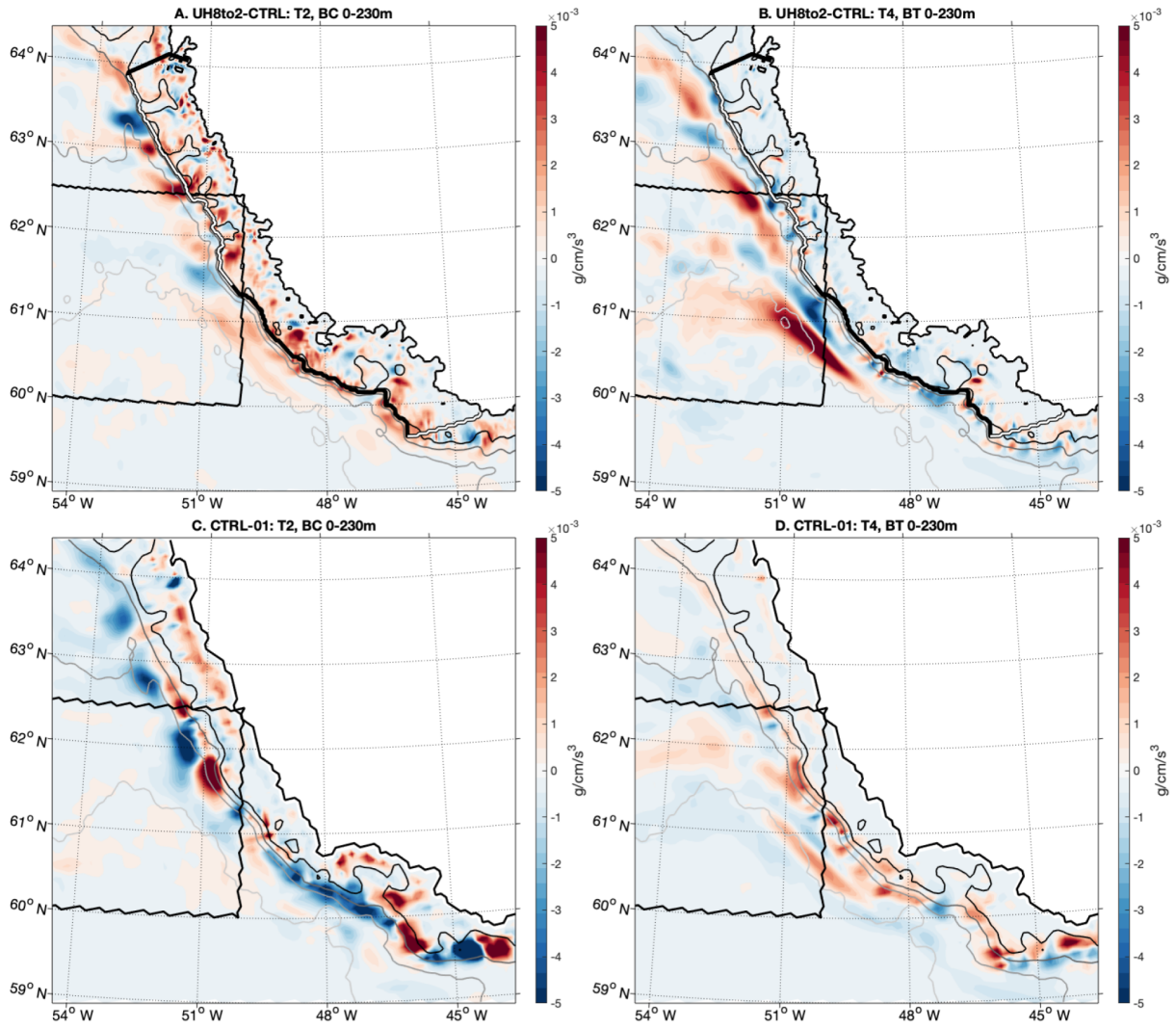

Figure 2.11. Baroclinic (T_2, BC) and barotropic (T_4, BT) conversion terms (g/cm/s^3) in the UH8to2-CTRL (A,B) and CTRL-01 (C,D) simulations averaged over the upper 230m. In Panels A and B, the shelf break contour is shown by the black (South Section) and white (North section) lines. The 400, 800, 2000, and 3000 m isobaths are plotted from dark to light gray. The black box indicates the high EKE region as in Figure 2.8.

doubles when resolution increases from the 0.1° grid to the UH8to2 grid. The freshwater forcing experiments exhibit T_4 conversion fluxes similar to those of the UH8to2-CTRL. With the addition of vertically diluted meltwater in the UH8to2-SPRD case, baroclinic conversion increases by approximately 20% over the shelf. This change is discussed in more detail in Section 2.3.3.

The eddy conversion terms from the UH8to2 show that both baroclinic and barotropic conversion contribute to the generation of eddies in this region. This result compares favorably with findings from other studies, despite differences in methodology. Rieck et al. (2019) find contributions from both baroclinic and barotropic instabilities in a 1/20° ocean model (a resolution that is comparable to the UH8to2 in the Labrador Sea). Modeling studies with lower resolution that are dynamically similar to the CTRL-01 grid also show that IRs are generated by baroclinic and barotropic instabilities in both idealized (Katsman et al., 2004) and realistic (Zhu et al., 2014) configurations. Eddy-permitting simulations have also shown that baroclinic instabilities are the primary contribution to eddy generation (Luo et al., 2016; Saenko et al., 2014). On the other hand, (Eden and Böning, 2002) concluded that barotropic instabilities are the dominant mechanism. Across these studies, the model setup, choice of eddy timescale, and portion of the water column and shelf break to be considered all factor into the difference in energy conversion terms. A full energy budget of the West Greenland Current is beyond the scope of this study but would be needed to clarify these discrepancies.

Deep Convection and Mixed Layer Depth

MLD is calculated by the model based on the definition of Large et al. (1997). The MLD is the shallowest depth at which the density difference from the surface equals the maximum stratification in the water column. A common alternative to the threshold definition for MLD is derived from the vertical gradient in temperature and salinity (Holte and Talley, 2009). The definition of MLD certainly plays a role the deviation between our results and other simulations which use the method from (Holte and Talley, 2009).

The March 1992 average MLD is plotted for the UH8to2-CTRL and CTRL-01 cases in

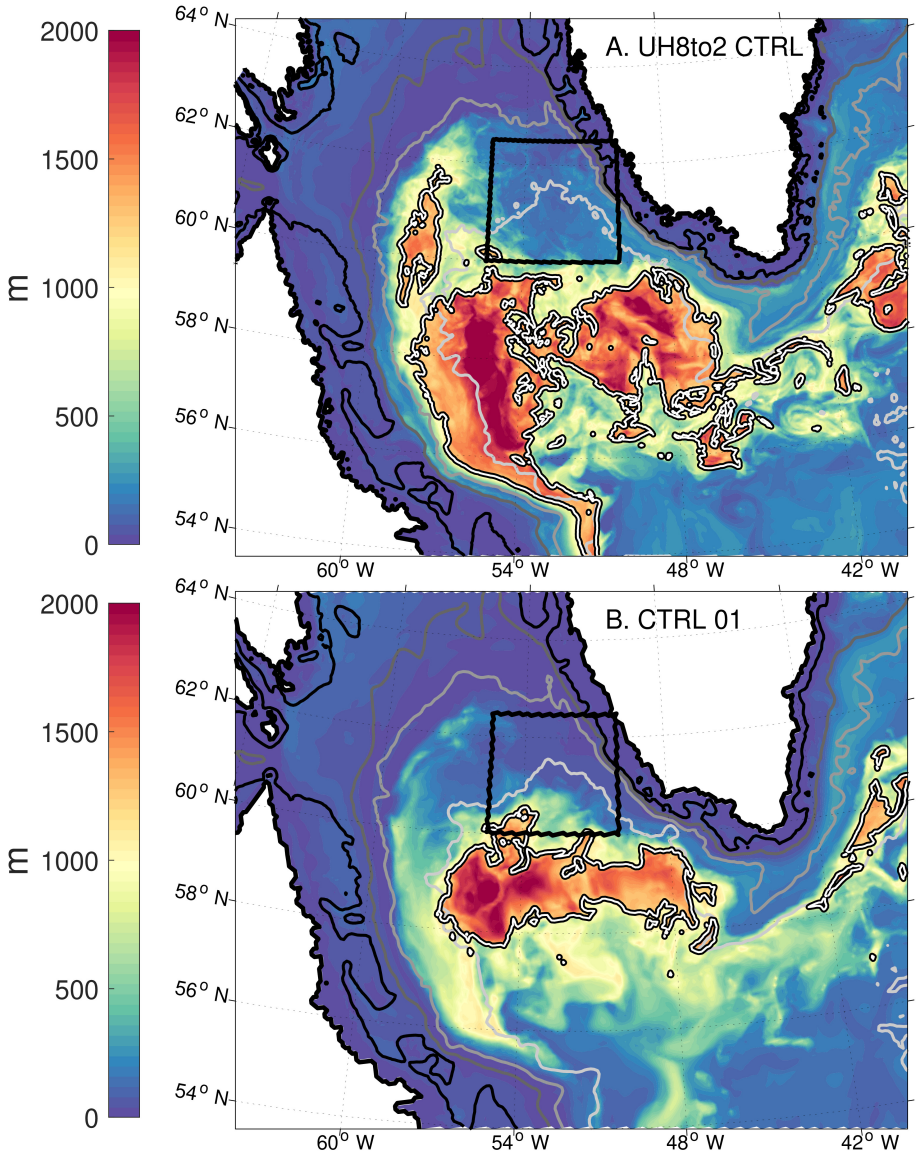

Figure 2.12. March 1992 average MLD (m) from the UH8to2-CTRL simulation (A) and the CTRL-01 simulation (B). The 1500 m MLD contour is outlined in both (A) and (B). The 400, 800, 2000, and 3000 m isobaths are plotted from dark to light grey. The black box is the same as in Figure 2.8.

Figure 2.12. We classify the areas where the mixed layer is deeper than 1,500 m to be the deep convection zones. The total area with MLD>1,500 m in the UH8to2-CTRL case is 117,300 km^3 and 45,244 km^3 in the CTRL-01 case. With the addition of meltwater, the convective area in the UH8to2-SPRD simulations is reduced to $\sim$81,000 km^3.

In both model configurations, deep convection occurs in the Irminger Sea. With higher resolution, there is a southward shift in the deep convection zone in the Labrador Sea and a region of deep MLD along the Labrador Shelf. This southward shift is similar to the changes in MLD with resolution as noted by (Pennelly and Myers, 2020) when increasing resolution from 1/12° to 1/60°. The increase in resolution from the CTRL-01 to UH8to2-CTRL case does not show the same reduction in MLD as in their simulations, but the increase in resolution is not as significant ($\sim$5 km grid spacing in the CTRL-01 to $\sim$3 km UH8to2). The deep mixed layer in the boundary current has a similar structure to other high resolution simulations that use atmospheric reanalysis forcing (Pennelly and Myers, 2020; Rieck et al., 2019). Another study found that increasing resolution to be mesoscale resolving reduced the convection volume by 50% (Tagklis et al., 2020). The MLD is much deeper in the UH8to2 simulations, which could be because of interannual variability of convection in the Labrador Sea. Simulated results from comparable resolution studies: Pennelly and Myers (2020) and Rieck et al. (2019) use atmospheric forcing from 2004-2009 and 2000-2009, respectively. Observations from 1996 also show a similar structure but shallower mixed layer depths. However, the NAO phase had shifted dramatically by 1996 (Pickart et al., 2002). Observations from 2012-2016, a period during which the winter NAO had a strong positive phase similar to what occurred in the early 1990s, showed maximum mixed-layer depths in agreement with our simulations (1800 m in 2014, with a maximum of 2,100 m) (Yashayaev and Loder, 2017). The deep mixed layer along the Labrador Shelf Break is consistent with observations of convection occurring in that region (Cuny et al., 2005).

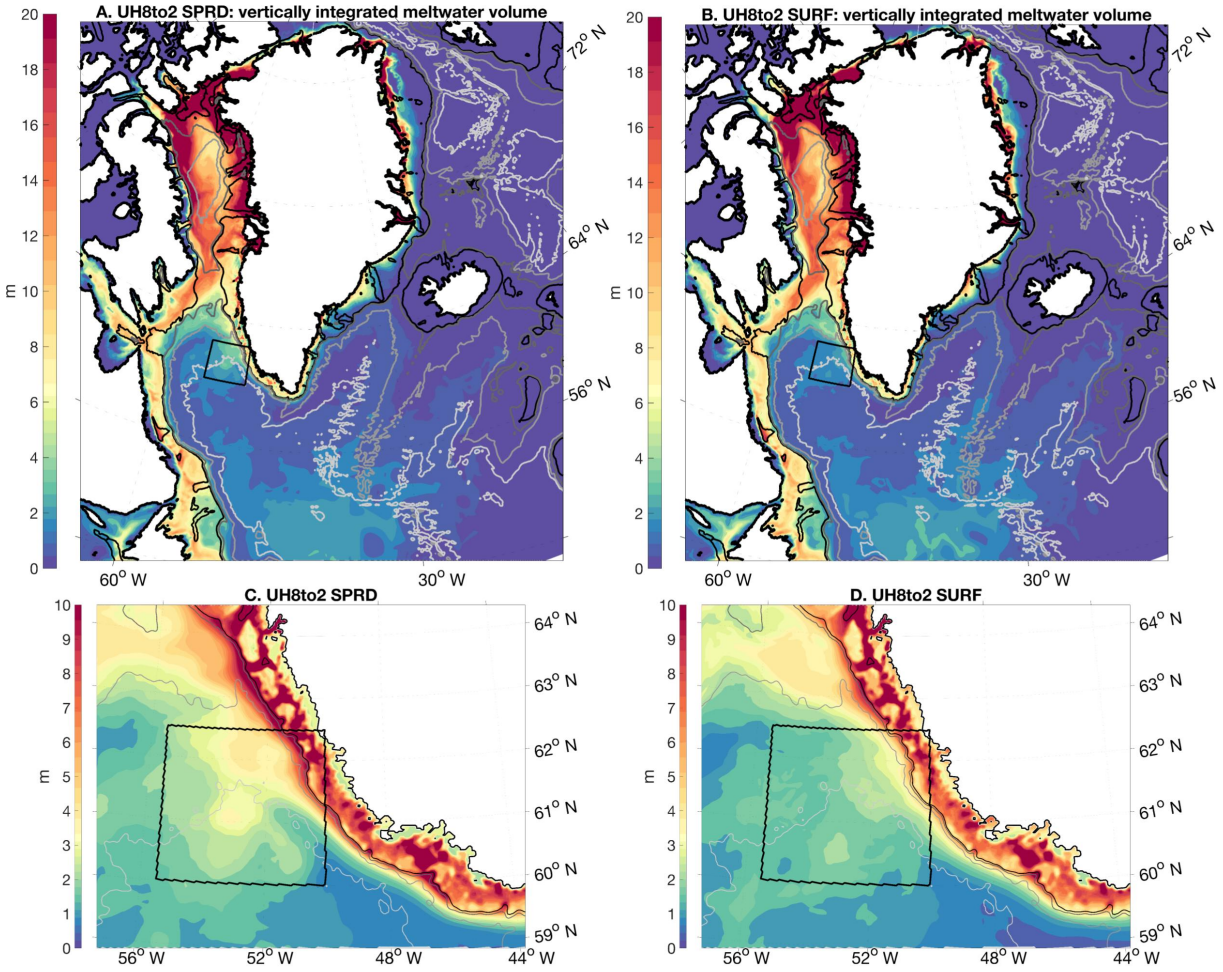

Figure 2.13. Vertically integrated meltwater content (m) calculated from the monthly average dye concentration in 1993-12 for the (A) UH8to2-SPRD and (B) UH8to2-SURF cases. Panels (C) and (D) show the meltwater content in the WGC eddy shedding region, note the difference in color scale from (A-B). The 400, 800, 2000, and 3000 m isobaths are plotted from dark to light gray. The black box indicates the high EKE region as in Figure 2.8

2.3.2 Comparison of UH8to2 SPRD and SURF

Meltwater Pathways

The meltwater pathways of the UH8to2-SPRD and UH8to2-SURF can be directly compared using the dye tracer added proportionally to the meltwater forcing. Figure 2.13 shows the vertically integrated meltwater content (Equation 2.8) for December 1993 at the end of the meltwater forcing experiment comparison period. There are many similarities between the two cases. As has been shown in many modeling experiments, both simulations show an accumulation of meltwater in Baffin Bay (Gillard et al., 2016). Spreading of meltwater into the Subpolar gyre occurs near the Flemish Cap, similar to the high-resolution results of (Böning et al., 2016).

A notable difference between the simulations is in the MWC (Equation 2.13) of the Labrador Sea, particularly in the highly eddy active region (Figure 2.13C, black box). In the UH8t02-SPRD there is 255 km^3 of meltwater, compared to 188 km^3 in the UH8to2-SURF case. The difference between the two simulations is not constant throughout the year, with the MWV being the same in April 1993 (145 km^3). From August to December the MWV in the control volume increases by 118 km^3 in the UH8to2-SPRD case and 78 km^3 in the UH8to2-SURF case. This is consistent with the off-shelf transport of dye tracer discussed in the following section. While this region is not an area where convection occurs, the difference in MWV indicates an increase in the transport of meltwater into the Labrador Sea when it is vertically distributed.

Off-shelf transport

The transport of meltwater from the continental shelf into the Labrador Sea occurs in southwest Greenland. Thus, we focus on the transport in this region to understand the impact of vertical dilution on the off-shelf transport of melt water. From daily averages of velocity, salinity, and dye tracer concentration, the cross-shelf transports are calculated. Both models are eddying; therefore we must account for the internal variability of the system. To do this, daily time series of the transports, are averaged for each month. This monthly average transport includes both

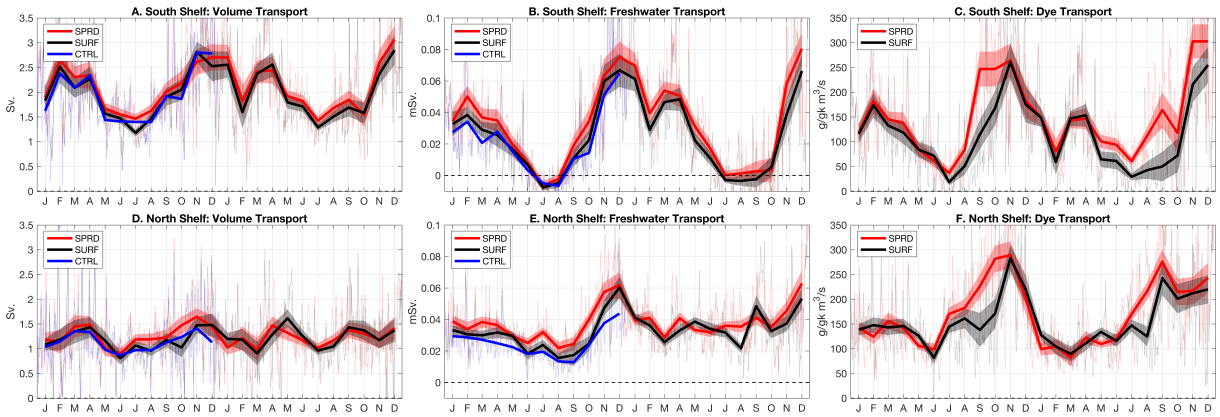

Figure 2.14. Net volume (Sv.), freshwater (mSv.), and dye tracer (g/kg m^3/s) transports off the Greenland Continental Shelf for 1992-1993. Panels A-C show the net transports for the southern section of the shelf, panels D-F show fluxes for the Northern Section of the shelf, see Figure 2.7. The thin lines are the transports calculated from the daily averages, the thick lines are the average of the daily transports for each month, and the shaded region shows the standard error of the mean of the transports. The UH8to2-SPRD is shown in red, the UH8to2-SURF is shown in black, and the UH8to2-CTRL is shown in blue (1992 only).

mean and eddy processes.

In the southern section of the shelf break, the seasonal cycle of the volume and freshwater transport off the shelf is apparent. This is consistent with previous studies, which have shown the link between the winds and the off-shelf transport of freshwater. In the summer (June, July, and August), when the winds are weak there is little off-shelf transport. During the winter months, along-shore winds are upwelling favorable and drive off-shelf transport (Castelao et al., 2019). In the northern section of the shelf, there is a fall/winter (October to January) increase in the off-shelf freshwater transport, but the volume transport does not exhibit a clear seasonal cycle.

The seasonality of the dye tracer transport (or meltwater transport) off the shelf is controlled both by the seasonal strengthening of the winds and the timing of the addition of the Greenland meltwater. The dye tracer transport peaks in the fall/winter and is weakest in the summer. For the months August, September, and October (ASO) there is more dye tracer transport off the shelf in the UH8to2-SPRD case compared to the UH8to2-SURF. This indicates a potential difference in the timing of a potential stratifying impact of Greenland meltwater on the Labrador Sea.

The UH8to2-SPRD case shows the most off-shelf transport of freshwater compared to either the UH8to2-SURF or UH8to2-CTRL cases. This difference is clearest in the southern section of the shelf, but is also true for the northern section of the shelf. The increase in transport is greater that the standard-error-of-the-mean estimate for both simulations in 1992-1993 for 14 months (Southern Shelf) and 17 months (North Shelf). The total amount of meltwater added to the UH8to2 simulations is the same. This increase in freshwater transport off the shelf could be indicative of more meltwater being transported off the shelf in the UH8to2-SPRD case (compared to the UH8to2-SURF). However, because the volume of meltwater is small and the difference in dye tracer transport does not indicate an overall greater transport of meltwater off the shelf in the UH8to2-SPRD case, we conclude that the increase in off-shelf transport of freshwater cannot be from meltwater alone.

Outside of the ASO period, the amount of dye tracer (meltwater) transport off the shelf is not statistically significantly greater in the UH8to2-SPRD case. This indicates that the increased freshwater flux is not simply an increase in off-shelf transport of meltwater. Over the period 1992-1993, the average difference between the UH8to2-SPRD and UH8to2-SURF freshwater transport is 6.6 mSv in the South Shelf and 4.8 mSv across the North Shelf. Integrated over the period 1992-1993, a total of 417 km^3 (South Shelf) and 300 km^3 (North Shelf) more freshwater is transported into the Labrador Sea in the UH8to2-SPRD case compared to the UH8to2-SURF. In the year 1992 the freshwater transport across the shelf break in the UH8to2-SPRD case is 40% greater than the UH8to2-CTRL case compared to a 20% increase in the UH8to2-SURF case. The increase in off-shelf freshwater flux is therefore sensitive to the vertical dilution of meltwater.

2.3.3 Eddy Generation Mechanisms

To understand the mechanism that drives the difference in the off-shelf transport of freshwater when meltwater is vertically diluted or concentrated at the surface, we focus on the period from September to November. Vertical profiles of the transport, EKE, horizontal density

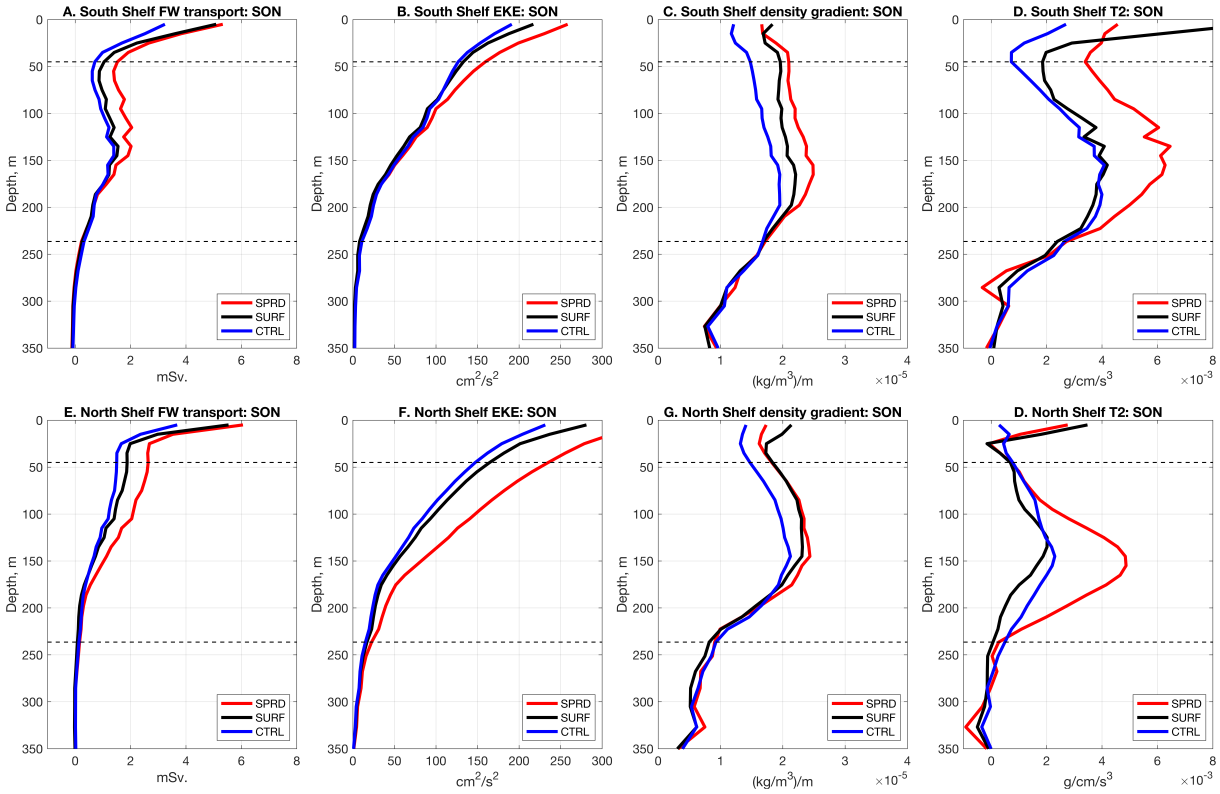

Figure 2.15. Vertical profiles for the South Shelf (A-D) and North Shelf (E-H) averaged over the months of September, October, and November for 1992. Results from the three UH8to2 cases are shown. (A,E) Net freshwater transport (mSv) across the shelf, (B,F) average EKE (cm^2/s^2) along the section, (C,G) average magnitude in the density gradient along the section ($kg/m^3/m$), and (D,H) average baroclinic conversion (T_2, $g/cm/s^3$) along the section.

gradient magnitude, and baroclinic conversion are compared across the three UH8to2 cases in Figure 2.15. We find that the UH8to2-SPRD case has enhanced baroclinic conversion compared to the other simulations.

The vertical structure of the freshwater transport reveals a two-layer structure. In the surface layer Ekman transport drives the off-shelf transport of freshwater (Schulze Chretien and Frajka-Williams, 2018). Both the UH8to2-SPRD and UH8to2-SURF cases exhibit a similar increase in off-shelf freshwater transport in this layer compared to the UH8to2-CTRL. Across the Southern Shelf, there is also a subsurface maximum in the freshwater transport into the basin at $\sim$150 m in all cases. The UH8to2-SPRD case has the greatest freshwater transport at depth. The freshwater transport across the Northern Shelf has a maximum in the surface layer (0-30 m), with a steady decrease between 30-150 m. The UH8to2-SPRD case exhibits the most off-shelf freshwater in both sections below the Ekman layer. Thus we conclude that the increase in off-shelf transport of freshwater in the UH8to2-SPRD case is not related to changes in the wind-driven Ekman transport of freshwater off the shelf.

The EKE is also elevated in the UH8to2-SPRD case compared to the UH8to2-SURF and UH8to2-CTRL. There is little change in the EKE between the UH8to2-SURF and UH8to2-CTRL cases during this period. In the UH8to2-SPRD the average EKE along the Northern Shelf increases more broadly in depth, from 0-230 m, compared to along the Southern Shelf, 0-100 m.

We examine the magnitude of the horizontal density gradient in an attempt to understand how the contribution to the baroclinic conversion term, T_2. Our focus is on T_2 because it is the dominant eddy conversion term in this region (see Figure 2.11) and the meltwater forcing impacts the PEM. The vertical structure of the magnitude of the horizontal density gradient is similar between the three cases. Along the entire shelf, the maximum gradient is at $\sim$150 m. Both the freshwater forcing experiments exhibit stronger horizontal density gradients compared to the UH8to2-CTRL; the UH8to2-SPRD case has the highest density gradient along the southern shelf.

The baroclinic conversion term is greatest at depth (between 50-230 m) in the UH8to2-

SPRD. Along the Southern Shelf, the maximum increases from $\sim$4 g/cm/s^2 in the UH8to2-SURF to $\sim$6 g/cm/s^2 in the UH8to2-SPRD. Along the Northern Shelf, the maximum in baroclinic conversion at 150 m in the UH8to2-SPRD is twice the maximum in the UH8to2-SURF. Notably, in the UH8to2-SURF the baroclinic conversion in the upper 30 m is significantly greater than the baroclinic conversion in any other part of any other simulation.

We do not expect EKE or baroclinic conversion to be directly correlated to off-shelf transport of freshwater. However, eddies do transport freshwater from the shelf into the basin (Castelao et al., 2019). The results of the UH8to2 simulations suggest that by vertically distributing meltwater we can excite baroclinic instabilities at the continental shelf break. This process varies seasonally, and the impact is greatest between September-November. This is also the period when there is a divergence in the off-shelf transport of dye tracer in the UH8to2-SURF and UH8to2-SPRD case.

2.4 Conclusions

Using four coupled ocean/sea-ice simulations, we investigate the impact of GIS meltwater on the transport of freshwater into the Labrador Sea. Using simulations that resolve mesoscale eddies and two meltwater forcing schemes we focus on the transport of freshwater into the Labrador Sea because of the influence of deep convection in that basin has on AMOC variability. We find that with increased resolution (CTRL-01 to UH8to2-CTRL) there is an increase in EKE in the basin and the deep convection zone shifts south in the basin. Increases in both barotropic and baroclinic conversion contribute to the greater EKE. Barotropic conversion along the Southwest Greenland shelf-break also maintains a similar spatial pattern and increases with model resolution. There is limited baroclinic conversion in the lower resolution (CTRL-01) simulation but at high resolution (UH8to2) the magnitude is equal to or greater than the barotropic conversion.

Using the higher resolution (UH8to2) mesoscale eddy-resolving simulations, we test

the response to two GIS meltwater forcing schemes. We find that when meltwater is vertically distributed, the total freshwater transport into the Labrador Sea is amplified compared to cases with no meltwater and meltwater concentrated in the surface layer. This is important when considering the potential impact of anomalous freshwater on deep convection and AMOC variability. If GIS meltwater modifies shelf dynamics to increase transport of freshwater into the basin, then it may have disproportionate impact on freshening of the Labrador Sea. Examining the multi-year variability of meltwater transport into the Labrador Sea and deep convection is further work that can be done with the UH8to2-SPRD simulation presented in this study.

The proposed mechanism for amplifying off-shelf transport of freshwater requires sufficiently high vertical and horizontal resolution to resolve baroclinic instabilities. The baroclinic conversion term in the 1/10° 42 z-level simulation, while very high in isolated locations, was not the dominant term along the shelf break as in the UH8to2 simulations. If a vertically distributed meltwater forcing in a lower resolution model, where the transfer of energy from PEM to EPE is not fully resolved, did not display the same enhanced off-shelf freshwater transport that would be further evidence that it is the result of baroclinic eddies.

The increase in EKE and surface current speed with the addition of GIS meltwater is consistent with studies that suggest the ocean is accelerating under climate change (Peng et al., 2022; Martínez-Moreno et al., 2021). An increase in EKE of 2-5% at high latitudes has been observed in satellite altimetery (Martínez-Moreno et al., 2021). In simulations, the acceleration is attributed to increased stratification, due to surface warming (Peng et al., 2022). Sea surface salinity changes, primarily from Arctic sea-ice melt, decelerate the circulation of the Subpolar North Atlantic and AMOC in the same study (Peng et al., 2022). We find that GIS meltwater accelerates shelf break currents and increases EKE, particularly when it is diluted vertically, reducing the impact on stratification. Further analysis of the multi-year trend in current velocity, EKE, and off-shelf transport is needed to establish a trend that can be linked to GIS meltwater.

Acknowledgments

T.J. Morrison, J.L. McClean and S.T. Gille were funded by DOE Office of Science grants: DE-SC0014440 and DE-SC0020073. The simulations were supported by an Advanced Scientific Computing Research (ASCR) Leadership Computing Challenge (ALCC) grant and standard Energy Research Computing Allocations Process (ERCAP) Allocations on Cori at the National Energy Research Scientific Computing (NERSC). Data from the AR07W repeat hydrography line used in this chapter publicly available online at https://doi.org/10.3334/cdiac/otg.carina_18hu19930617 by the NOAA National Centers for Environmental Information. We would like to thank Elizabeth Hunke (LANL), John Ritchie, Anthony Craig, and Judy Gaukel for their contributions to configuring the UH8to2 simulations.

Chapter 2, in part is currently being prepared for submission for publication of the material. Morrison, Theresa; McClean, Julie; Gille, Sarah; Maltrud, Mathew; Ivanova, Detelina. The dissertation author was the primary investigator and author of this paper.

Chapter 3

A Glacial Fjord Box Model: Derivation and Representation of Glacially Modified Water

3.1 Introduction

The Greenland Ice Sheet (GIS) has lost an estimated 3,902±342 GT of ice between 1992 and 2018; roughly half of this mass loss is attributed to liquid runoff and half to dynamic mass loss (The IMBIE Team, 2020). The influx of freshwater from the GIS to the ocean has the potential to disrupt the local circulation and Atlantic Meridional Overturning Circulation (Böning et al., 2016; Bamber et al., 2018; Weijer et al., 2019). In a warming climate, mass loss from the GIS is projected to continue, increasing the volume of anomalous freshwater entering the ocean (Pattyn et al., 2018). Therefore, including realistic boundary conditions for this freshwater forcing in Earth System Models (ESMs) is important for long-term projections of the climate state (Straneo et al., 2019). However, the horizontal resolution of ESMs used in long-term climate projections (such as those used in the Climate Model Intercomparison Project 6 (Griffies et al., 2016)) is insufficient to resolve the narrow fjords that surround Greenland and consequently, the meltwater pathways through the fjords from the ice termini to the continental shelves. Observations show that within fjords, ice sheet runoff is substantially modified (Beaird et al., 2015, 2017, 2018a; Jackson and Straneo, 2016), and icebergs melt (Enderlin et al., 2016).

These processes are often unaccounted for in ESMs, and instead freshwater fluxes from the GIS are added to the surface layer of the ocean as a zero-salinity forcing adjacent to the coast (e.g., Böning et al., 2016; Dukhovskoy et al., 2016b; Gillard et al., 2016, and others).

This methodology used for ice sheet meltwater is not dissimilar to the historic treatment of riverine freshwater inputs in ESMs. The implementation of a parameterization for the mixing of terrestrial freshwater fluxes in riverine estuaries improved stratification and sea surface salinity in an ESM (Sun et al., 2019). Within estuaries, both tides and winds drive shear-induced mixing and internal waves entrain saltwater (MacCready et al., 2010). This mixing and entrainment drives an exchange flow at the mouth of the estuary that is much greater than the freshwater volume flux entering the estuary. The glacial fjords of Greenland are long (50-100 km), narrow (5-10 km), and deep (100s m) estuaries with exchange circulation that is much greater than the freshwater inputs (Straneo and Cenedese, 2015a; Carroll et al., 2016; Zhao et al., 2021). For the entire GIS, freshwater fluxes into the ocean are roughly evenly split between solid discharge and liquid runoff, but the ratio varies for each fjord. Mapping the subglacial hydrology of the GIS is challenging (Morlighem et al., 2017), but a portion of the runoff enters the ocean at the base of tidewater glaciers as subglacial discharge (Chu, 2014). From 2010-2020, subglacial discharge accounted for an estimated 13% of total freshwater flux entering the ocean (Slater et al., 2022).

As subglacial discharge enters the ocean, it forms buoyant plumes that rise while entraining the denser surrounding water. The high velocity of the buoyant plume ($\sim$2 m/s) also drives high rates of submarine melting near the plume (Xu et al., 2013; Slater et al., 2015, 2018). Subglacial discharge plumes are critical to driving the renewal of deep waters within fjords, which can further enhance heat transport toward the ice (Carroll et al., 2017). The water exported from fjords as a part of this exchange circulation is known as Glacially Modified Water (GMW) and is a mixture of the inflowing ambient waters, subglacial discharge, and submarine meltwater. Observations have shown that this water mass is exported from fjords over the upper 100-200 m and is primarily comprised of ambient waters (Beaird et al., 2018a; Muilwijk et al., 2022). In Sermilik Fjord, East Greenland, observed GMW was comprised of 88% Atlantic Water

(Beaird et al., 2018a); similarly, at Upernavik Fjord, West Greenland, GMW consisted of only 1% subglacial discharge (Muilwijk et al., 2022). As with the transformation that occurs within riverine estuaries, this process is not resolved in ocean models and needs to be parameterized. Muilwijk et al. (2022) use buoyant plume theory to approximate the dilution of meltwater within Upernavik Fjord. Using a high-resolution realistic geometry simulation of Kangerlussuaq Fjord, East Greenland, Cowton et al. (2016) derived a relationship between subglacial discharge and exchange flow. The goal of this study is to build on a parameterization developed for improving the representations of riverine estuaries in ESMs to provide a more realistic freshwater input from the GIS into the ocean. We combine buoyant plume theory and a two-layer energy balance box model of estuarine exchange to represent the mixing and entrainment within glacial fjords.

The energy balance Estuary Box Model (EBM) developed by Sun et al. (2017) is a steady state two-layer model that parameterizes the mixing within a river plume. The conservation of volume, salinity, and potential energy are used to find the exchange circulation strength and salt flux out of the river plume. Tidal mixing is represented in the model in the time-varying length of the river plume. The EBM was able to represent the seasonal salt flux out of riverine estuaries. The implementation of this EBM in an ocean model improved modeled surface salinity and stratification in the upper 40 m of the water column (Sun et al., 2019). This improvement was greatest near the largest rivers that the parameters of the EBM were tuned to match. The improvements to stratification are particularly important in the case of GIS freshwater fluxes because questions remain about the potential impact of GIS meltwater on deep convection in the Subpolar North Atlantic.

In this chapter, we present a Fjord Box Model (FBM) that modifies the EBM by replacing the riverine boundary conditions with a subglacial discharge plume. In section 3.2, the FBM is derived from conservation equations and the buoyant plume model. The key parameters in the FBM are identified, and the idealized simulations used for comparison are described. In section 3 we compare to both idealized simulations and observations from Beaird et al. (2018a) and Muilwijk et al. (2022). Finally, in section 4 we discuss the strengths and weaknesses of the FBM.

3.2 Fjord Box Model Development

The FBM represents the mixing of subglacial discharge and shelf water (or Atlantic Water, AW) in both a buoyant plume and in a two-layer estuary. This simple model does not include any additional water masses (such as Polar Water) or inputs from melting ice. The basis of both models is the conservation of volume, salt, heat, and potential energy within the fjord. We replace the boundary condition on the river end of the EBM with a buoyant plume. From the fjord mouth to the plume boundary, the fjord circulation is represented with two layers. In this section, the EBM, FBM, and line plume models are described. An outline of the derivation of the equations in the FBM is given; see Appendix A for the full details. We show the equations for the buoyant plume model and the solutions for a line plume. Finally, the FBM is tested to identify the most important parameters.

The FBM is based on the well-established EBM of Sun et al. (2017), a two-layer model with adjusting length L, uniform depth H, and constant width W. Figure 3.1A is a schematic of the EBM (after Sun et al., 2017, their Figure 1). The adjusting length is based on the salt intrusion into the river (MacCready et al., 2010). As a result, the lower-layer boundary condition at the head of the estuary is $S = 0$. The EBM is steady state, laterally averaged, and tidally averaged. The salinity in the layers is vertically uniform but varies linearly and horizontally.

The FBM is a steady-state laterally averaged model that expands on the EBM with the addition of a box representing a subglacial discharge plume. The domain is defined similarly to Sun et al. (2017); the FBM is shown in Figure 3.1B. As with the EBM, the domain is $-L < x < 0$ with $x = -L$ at the plume box, and $x = 0$ at the shelf. However, a constant L is assumed that represents the length of the fjord. The surface is a rigid lid at $z = H$ and the interface is at $z = h$, with the bottom at $z = 0$. As in the EBM, properties in the layers are vertically uniform but vary linearly horizontally.

In addition, we test the Line Plume Model (LPM) separately from the FBM, shown in Figure 3.1C. Direct observations of subglacial discharge plumes are challenging to obtain

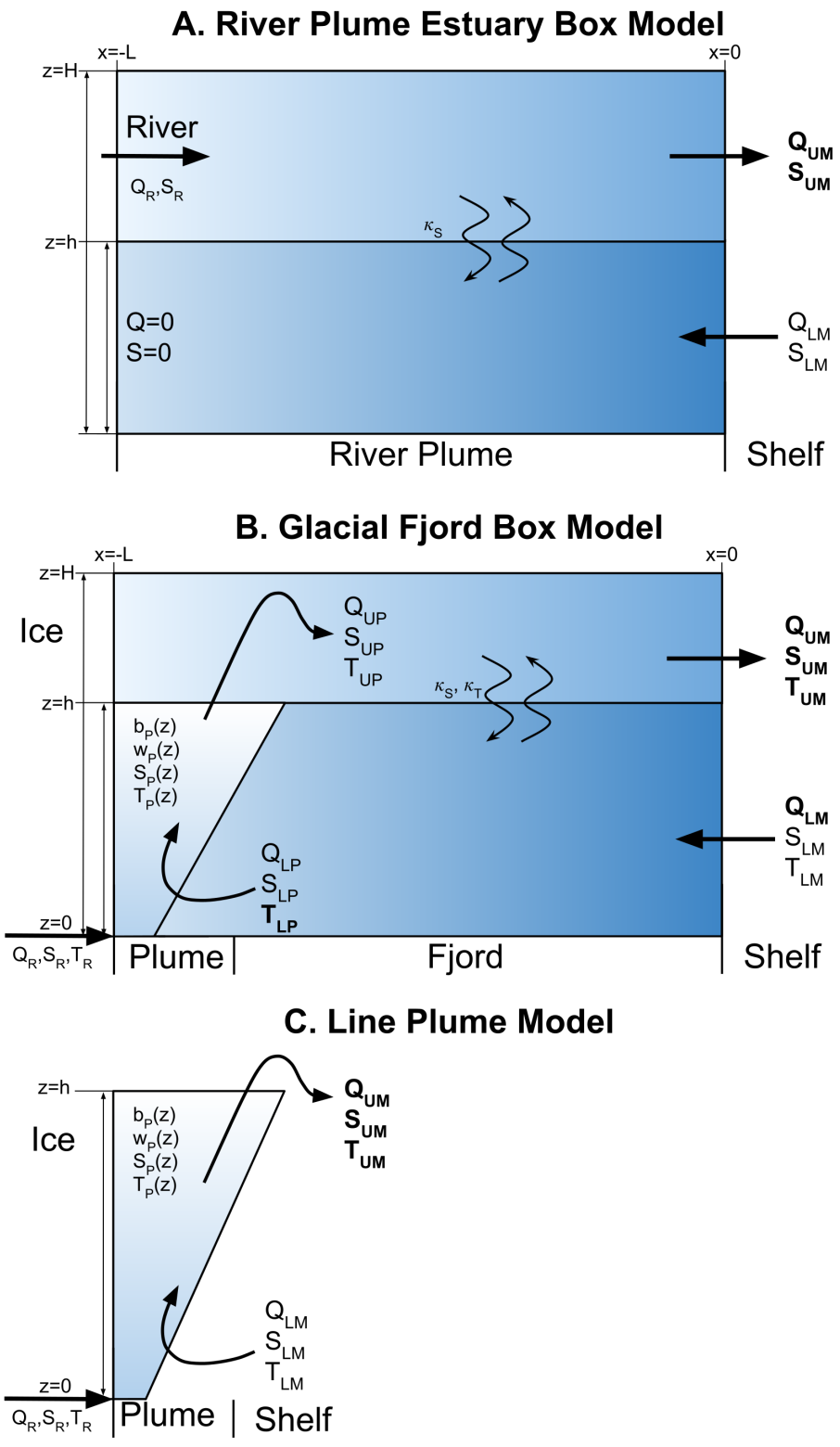

Figure 3.1. Schematics of (A) the Estuary Box Model from Sun et al. (2017), (B) the Fjord Box Model described in this work, and (C) the Line Plume Model from Slater et al. (2016). The description of the variables is in Table 3.1 and parameters in Table 3.2.

but suggest that a line plume is more representative of subglacial discharge plumes than other geometries (Jackson et al., 2017; Fried et al., 2019). The LPM has a width W_p, which is its extent in the across-fjord direction and a thickness b which is its extent into the fjord. The height h is determined by the depth where the plume reaches neutral buoyancy. A line plume with a width of 50 m entrains the same volume of water as two line plumes of 25 m.

The variables of the FBM, temperature, salinity, and volume fluxes between the three boxes of the FBM, are listed in Table 3.1. The subscripts are: lower mouth (LM), lower plume (LP), upper plume (UP), and upper mouth (UM). The subglacial discharge, Q_R, is assumed to have zero temperature and salinity. The FBM uses the shelf temperature and salinity (T_{LM} and S_{LM}) to calculate the exchange flow and the salt and temperature flux out of the fjord. The FBM also finds the flux of heat toward the glacier face, which is important for ocean-driven melting of ice. The goal of this work is to improve the GIS meltwater forcing boundary conditions in ocean models. Thus we primarily focus on the resulting S_{UM} and Q_{UM} from the FBM.

Table 3.1. Variables used in the FBM separated into input variables, internal variables, and output variables.

Variable	Name		Units
S_{LM}	Lower Layer Salinity at Mouth	input	PSU
T_{LM}	Lower Layer Temperature at Mouth	input	°C
Q_R	Subglacial Discharge	input	m^3/s
S_{LP}	Lower Layer Salinity at Plume		PSU
Q_{LP}	Lower Layer Volume Flux at Plume		m^3/s
S_{UP}	Upper Layer Salinity at Plume		PSU
T_{UP}	Upper Layer Temperature at Plume		°C
Q_{UP}	Upper Layer Volume Flux at Plume		m^3/s
Q_{LM}	Lower Layer Volume Flux at Mouth	output	m^3/s
T_{LP}	Lower Layer Temperature at Plume	output	°C
S_{UM}	Upper Layer Salinity at Mouth	output	PSU
T_{UM}	Upper Layer Temperature at Mouth	output	°C
Q_{UM}	Upper Layer Volume Flux at Mouth	output	m^3/s

3.2.1 Fjord Governing Equations

The laterally-averaged steady-state conservation equations are

$$\frac{\partial u}{\partial x}+\frac{\partial w}{\partial z}=0, \tag{3.1}$$

$$\frac{\partial uS}{\partial x}+\frac{\partial wS}{\partial z}=\frac{\partial}{\partial x}\Big(k_H\frac{\partial S}{\partial x}\Big)+\frac{\partial}{\partial z}\Big(k_v\frac{\partial S}{\partial z}\Big), \tag{3.2}$$

$$\frac{\partial uT}{\partial x}+\frac{\partial wT}{\partial z}=\frac{\partial}{\partial x}\Big(k_H\frac{\partial T}{\partial x}\Big)+\frac{\partial}{\partial z}\Big(k_v\frac{\partial T}{\partial z}\Big), \tag{3.3}$$

where u and w are the along-fjord and vertical velocity, respectively, and κ_H and κ_V are the horizontal and vertical eddy diffusivities, respectively. The conservation of potential energy ($\mathrm{PE}=\rho gz$) equation comes from combining the conservation of salt and temperature equations using the equation of state: $\rho=\rho_0(1+\beta_S S-\beta_T T)$,

$$\frac{\partial u\mathrm{PE}}{\partial x}+\frac{\partial w\mathrm{PE}}{\partial z}=\frac{\partial}{\partial x}\Big(k_H\frac{\partial \mathrm{PE}}{\partial x}\Big)+\frac{\partial}{\partial z}\Big(k_v\frac{\partial \mathrm{PE}}{\partial z}\Big)-k_v g\frac{\partial \rho}{\partial z}-g\frac{\partial k_v\rho}{\partial z}+wg\rho, \tag{3.4}$$

where $\beta_S=7.4$ (g/kg)$^{-1}$, $\beta_T=2.0$ K^{-1}, and $\rho_0=1000$ kg/m^3. For the entire fjord, volume is conserved:

$$Q_{LM}+Q_{UM}-Q_R=0. \tag{3.5}$$

The conservation of salt in the lower layer is used to constrain the salinity entering the plume S_{LP}. We assume a linear along-fjord salinity gradient. Thus in the lower layer, the along-fjord salinity is: $S_L(x)=(S_{LM}-S_{LP})x/L+S_{LM}$, and an analogous expression represents the upper layer. The vertical velocity within the fjord is uniform in the along-fjord direction and piecewise linear in the vertical, with the maximum velocity at the interface $z=h$, where $w(z=h)=w_I$.

Therefore integrating (A.15) term by term for $-L < x < 0$ and $0 < z < h$ we have:

$$\int_0^h dz \int_{-L}^0 dx \frac{\partial uS}{\partial x} = hu_{LM}S_{LM} - hu_{LP}S_{LP}, \tag{3.6}$$

$$\int_0^h dz \int_{-L}^0 dx \frac{\partial wS}{\partial z} = \int_{-L}^0 dx w_I S_L(x) = \frac{w_I L}{2}(S_{LM} - S_{LP}), \tag{3.7}$$

$$\int_0^h dz \int_{-L}^0 dx \frac{\partial}{\partial x}\Big(k_H \frac{\partial S}{\partial x}\Big) = \kappa_v \int_0^h dz \Big(\frac{\partial S_{LM}}{\partial x} - \frac{\partial S_{LP}}{\partial x}\Big) = 0, \tag{3.8}$$

which are the horizontal advection, vertical advection, and horizontal diffusion terms, respectively. For the vertical diffusion term, we need to define $\partial S/\partial z = (S_U - S_L)\delta(h-z)$, where δ is the Dirac Delta function. Given: $S(x,z) = S_L(x) + (S_U(x) - S_L(x))H(h-z)$, and H is the Heaviside function. Thus we can derive the diffusion across the interface of the upper and lower fjord boxes as

$$\int_0^h dz \int_{-L}^0 dx \frac{\partial}{\partial z}\Big(k_v \frac{\partial S}{\partial z}\Big) = \kappa_v \int_{-L}^0 dx \Big(\frac{\partial S}{\partial z}\Big)\Big|_0^h \tag{3.9}$$

$$= \kappa_v \int_{-L}^0 dx \Big((S_U - S_L)\delta(h-z)\Big)\Big|_0^h \tag{3.10}$$

$$= \frac{\kappa_v}{dz} \int_{-L}^0 dx (S_U(x) - S_L(x)) \tag{3.11}$$

$$= \frac{\kappa_v L}{2dz}\Big(S_{LM} - S_{UM} + S_{LP} - S_{UP}\Big). \tag{3.12}$$

Multiplying each term by the width of the fjord W the lower-layer salt conservation equation in flux form is

$$Q_{LM}S_{LM} - Q_{LP}S_{LP} + \frac{(Q_{LM} - Q_{LP})}{2}(S_{LM} - S_{LP}) = \frac{\kappa_v A}{2dz}\Big(S_{LM} - S_{UM} + S_{LP} - S_{UP}\Big). \tag{3.13}$$

where $Q_{LM} = Whu_{LM}$, the volume flux into the fjord lower layer at the mouth. See Table 3.1 for all term definitions. The vertical volume flux between the upper and lower layers is $Q_V = w_I LW$, which is the same as the difference in the volume flux into the lower layer and the volume flux

into the plume: $Q_V = Q_{LM} - Q_{LP}$. The area of the interface between the two layers is $A = WL$.

We assume no horizontal diffusion of salt into the plume or at the mouth of the upper layer. This assumption is that $\partial S/\partial x = 0$ at $x = -L, 0$ for both layers. In addition, for the upper layer conservation of salinity, there is no salt flux at the surface $\partial S/\partial z = 0$ at $z = H$. Salt fluxes across the rigid lid could be added to the FBM to represent the freshwater flux into the upper layer from icebergs or sea ice. These assumptions are true for the temperature conservation equations and carry over to the boundary conditions for the PE equations.

In the next section, the buoyant plume component of the FBM is defined. For the full derivation of the FBM see Appendix A. The FBM for temperature and salinity is a set of nine coupled non-linear equations. A solution to these equations is found using Newton's method as described in Appendix B.

3.2.2 Buoyant Plume Governing Equations

For the buoyant plume we assume a geometry where subglacial discharge is distributed in a line along the front of the glacier. Observations suggest this plume geometry is realistic (Slater et al., 2022; Fried et al., 2019; Jackson et al., 2017). However, the FBM solution could be modified to include other plume geometries, which affect the entrainment and plume dynamics (Jackson et al., 2017). The equations describing the plume entrainment, velocity, temperature, and salinity are:

$$\frac{\partial(bu)}{\partial z} = \alpha u, \tag{3.14}$$

$$\frac{\partial(bu^2)}{\partial z} = bg', \tag{3.15}$$

$$\frac{\partial(buT)}{\partial z} = \alpha u T_{LP}, \tag{3.16}$$

$$\frac{\partial(buS)}{\partial z} = \alpha u S_{LP}, \tag{3.17}$$

where b is the plume thickness (i.e, distance from ice), u is the vertical velocity of the plume, T is the temperature of the plume, and S is the salinity of the plume (Morton et al., 1956; Jenkins, 2011; Cowton et al., 2015). The entrainment coefficient is α which is generally assumed to be 0.1 (Morton et al., 1956; Jackson et al., 2017; Cowton et al., 2015).

These equations can be solved analytically within an unstratified system without any melting from the ice sheet. The solutions are

$$b(z) = \alpha(z + z_0), \tag{3.18}$$

$$u(z) = (Q_R g_0' / \alpha)^{1/3}, \tag{3.19}$$

$$T(z) = T_{LP}[1 - z_0/(z + z_0)], \tag{3.20}$$

$$S(z) = S_{LP}[1 - z_0/(z + z_0)], \tag{3.21}$$

where

$$z_0 = (Q_R^2 / \alpha^2 g_0')^{1/3}, \tag{3.22}$$

$$g_0' = g(\beta_S S_{LP} - \beta_T T_{LP}). \tag{3.23}$$

The subglacial discharge volume flux is Q_R. These analytic solutions are referred to as the LPM (Slater et al., 2016).

From these equations we can calculate the volume flux from the lower layer into the plume

$$Q_{LP} = -W_p \int_0^h \alpha u(z) dz, \tag{3.24}$$

$$Q_{LP} = -hW_p \alpha^{2/3} [g Q_R (\beta_S S_{LP} - \beta_T T_{LP})]^{1/3}, \tag{3.25}$$

and the volume flux into the upper layer from the plume is $Q_{UP} = Q_{LP} + Q_R$. The salinity and temperature from the plume entering the upper layer (S_{UP} and T_{UP}) are the temperature and

salinity of the plume when it reaches neutral buoyancy.

3.2.3 Fjord Box Model Parameters

The parameters within the FBM and LMP can be broadly separated into three categories: known geometric parameters, unknown geometric parameters, and entrainment and mixing parameters. We test different ranges of the parameters to identify the parameters that most strongly influence S_{UM} and Q_{UM}. All of the parameters and their default values are given in Table 3.2. We find that the model is not sensitive to changes in fjord geometry (length and width). The most important parameters are those that control the balance of vertical mixing within the fjord and entrainment into the plume. We assume the entrainment coefficient has a set value $\alpha = 0.1$ as in other studies (Slater et al., 2022; Jackson et al., 2017; Cowton et al., 2016) and based on laboratory experiments (Morton et al., 1956; Ellison and Turner, 1959).

Table 3.2. Parameters of the FBM and LPM.

Parameter	Name	Default Value	Units
L	Fjord Length	50,000	m
W	Fjord Width	5,000	m
H	Total Depth	900	m
h	Interface Depth	800	m
W_p	Plume Width	25	m
dz	Vertical Diffusivity length scale	1	m
κ_v	Vertical Diffusivity	10^{-5}	m^2/s
α	Plume entrainment	0.1	

The bathymetry of glacial fjords of Greenland is challenging to measure (Morlighem et al., 2017). Fjord length, width, and depth are measurable but vary along the fjord. In the FBM, as L approaches zero the results converge to the LPM solution. The FBM is not sensitive to changes in L and W because the area of the two-layer interface in the fjord is multiplied by the vertical eddy diffusivity, κ_v, which is small.

The FBM represents the mixing between two water masses in two stages: in the fjord and in the plume. If we consider the flux out of the plume to be pure GMW, then the upper layer

represents mixing between pure GMW and shelf water. As runoff increases, GMW becomes fresher. Because the FBM is solved in steady state, a fresher upper layer and vertical mixing within the fjord mean the ambient water that is entrained into the plume is fresher, resulting in fresher GMW. This feedback can converge to a stable solution for a broad range of parameters. However, there is a limit where the ambient water entrained into the plume has zero salinity, which results in there being no stable solution for the EBM. This limit is controlled by the balance between mixing within the plume and within the fjord. For the FBM with the default parameters listed in Table 3.2, when $\kappa_v/dz > 1.2 \times 10^{-3}$, the FBM is overmixed and no solution exists. The default value of κ_v/dz used in the FBM is 1×10^{-5}. Besides the limit for real solutions, the GMW properties and exchange circulation strength are not sensitive to changes in κ_v/dz.

Given a constant value of α, the width of the buoyant plume and its height are key parameters that determine overall entrainment (see Equation 3.25). The geometry of glacial plumes is challenging to observe and may not be constant in time. The interface depth h is related to the depth of the neutral buoyancy of the plume. In our two-layer model, where the entire upper layer of the fjord is filled with glacially modified water, the best choice of h may differ from the depth where the plume reaches neutral density. This depends both on the stratification of the fjord, or in the simple unstratified case, the ambient salinity, and the subglacial discharge. Because h is not an independent variable in the FBM, h must be prescribed. The LPM solution can be computed using the shelf water properties to find the depth where the plume reaches neutral buoyancy. This does not take into account the along-fjord salinity gradient, but the buoyancy difference between the subglacial discharge and shelf water is much larger than the change in buoyancy from S_{LM} to S_{LP} so the plume height is well estimated. Unless otherwise stated, this LPM based approach is used to set the value for h in the FBM.

The FBM and LPM represent mixing between subglacial discharge and shelf water. Therefore, when plotted in Temperature-Salinity space the properties of the GMW fall along the runoff mixing line. In Figure 3.2 the shelf water and GMW properties are plotted. In

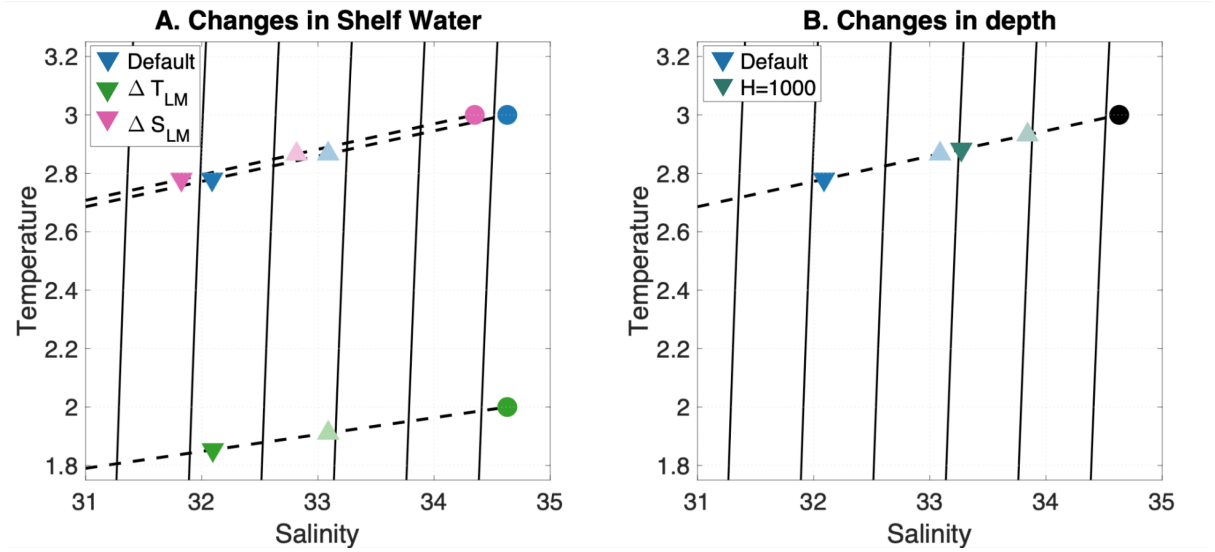

Figure 3.2. Comparison of the T (°C) and S properties of the input (S_{LM} and T_{LM}) and output (S_{UM} and T_{UM}) of the FBM and LPM. The circles are the lower mouth properties. The lighter colored upward pointing triangles are the output from the LPM, and the darker colored downward pointing triangles are the output from the FBM. The dashed line is the subglacial discharge mixing line that connects the lower mouth properties to the $S_R = 0$, $T_R = 0$. In all cases $Q_R = 1500\text{m}^3/\text{s}$ and other parameters used are those listed in Table 3.2. In panel (A) the three experiments are for different shelf water properties: (Blue) $S_{LM} = 34.63$ and $T_{LM} = 3$, (Pink) $S_{LM} = 34.35$ and $T_{LM} = 3$, and (Green) $S_{LM} = 34.63$ and $T_{LM} = 2$. In Panel (B), the Blue markers are the same as in (A), and the Teal are for the same shelf properties but $H = 1000$ m.

the FBM (downward pointing triangles in Figure 3.2A), the GMW has a greater fraction of subglacial discharge, and thus is colder and fresher than the GMW from the LPM (upward pointing triangles). When the shelf water temperature or salinity is changed, the GMW properties change by the same amount. With a deeper fjord, $H = 1000$ m compared to the default case of $H = 500$ m, the solution has more shelf water (teal markers in Figure 3.2B). The GMW properties from the FBM in a 1000-m deep fjord are similar to the GMW properties from the LPM in a 500-m fjord. In both cases the plume reaches the surface and $h/H \sim 0.95$. Without a less buoyant upper layer, such as a polar water layer, the subglacial discharge plume tends to reach the surface. The mid-depth equilibration is a common feature in observations of subglacial discharge plumes and is not represented in the FBM.

3.3 Idealized Geometry Fjord Simulations

The FBM is a simplified representation of the physics governing fjord circulation. The comparison to idealized MITgcm simulations with a rectangular geometry shows how well the FBM represents the circulation within the fjord without the complex geometry or surface forcings of a realistic fjords. We configure the MITgcm (Marshall et al., 1997a,b) for an idealized fjord with a rectangular fjord and shelf region. The model has a flat bottom in both the fjord and shelf and has no sill. The fjord is oriented east-to-west, with the plume on the west end of the fjord and a region on the east side of the domain that is restored to the initial shelf conditions. The horizontal grid spacing is 250 m and the vertical spacing is 50 m. The buoyant plume parameterization from Cowton et al. (2015) is used to represent a one grid cell wide sheet plume (Jenkins, 2011) in the center of the fjord. Our primary focus is on salt fluxes out of the fjord. The initial conditions are designed to represent the two-layer structure with salinity $S = 33$ for 0-150 m and $S = 34$ for 150-500 m. To minimize the impact of temperature we set it to zero everywhere. With the subglacial discharge, a dye tracer is added. The fjord is 50 km long and 500 m deep and is connected to a 22 km by 32 km shelf region.

We configure two versions of this simulation, one where the fjord width is roughly one Rossby radius wide ($W = 2000$ m) and second using a quasi-two-dimensional simulation where the fjord is one grid point wide. Many Greenlandic fjords fall in the one Rossby radius width range (Jackson et al., 2018). The one grid point wide configuration is meant to be a quasi-2D setup to test the impact of cross-fjord variability in the fjord circulation. We integrate both cases for 12 days to allow the fjord to reach a steady state which is determined by the time evolution of the exchange circulation strength. For each configuration, we run the model with four subglacial discharge levels Q_R = 100, 500, 900, and 1,300 m^3/s.

The equilibrated structure of the fjord properties is plotted in Figure 3.3. The surface layer salinity shows both the cross- and along-shelf variations in salinity (Figure 3.3A). The contours of dye tracer show the wedge of subglacial discharge in the fjord which follows the right side of the fjord. In the along fjord direction, Figure 3.3B, there is only a weak gradient in salinity. In Figure 3.3C-E the across fjord structure of along-fjord velocity, salinity, and dye tracer at the mouth of the fjord are shown. The typical estuarine circulation is apparent with the upper layer flowing out of the fjord and inflow at depth. The outflow is generally confined to the upper 2 layers (0-100 m) of the simulation. The out-flowing layer is fresh and contains a high concentration of subglacial discharge dye tracer. The exchange circulation at the fjord mouth is not symmetric, with greater volume transport out of the fjord on the south side (Figure 3.3C). The circulation is qualitatively similar to observations (Beaird et al., 2018a) and simulations with realistic geometry (Cowton et al., 2016)

3.4 Results

To assess the skill of the FBM in predicting GMW salinity and exchange circulation strength, we compare these quantities to those from the MITgcm idealized simulations and observations. The LPM is also used to provide estimates of exchange flow strength and GMW salinity. Using a high-resolution realistic model of an East Greenland fjord, Cowton et al. (2016)

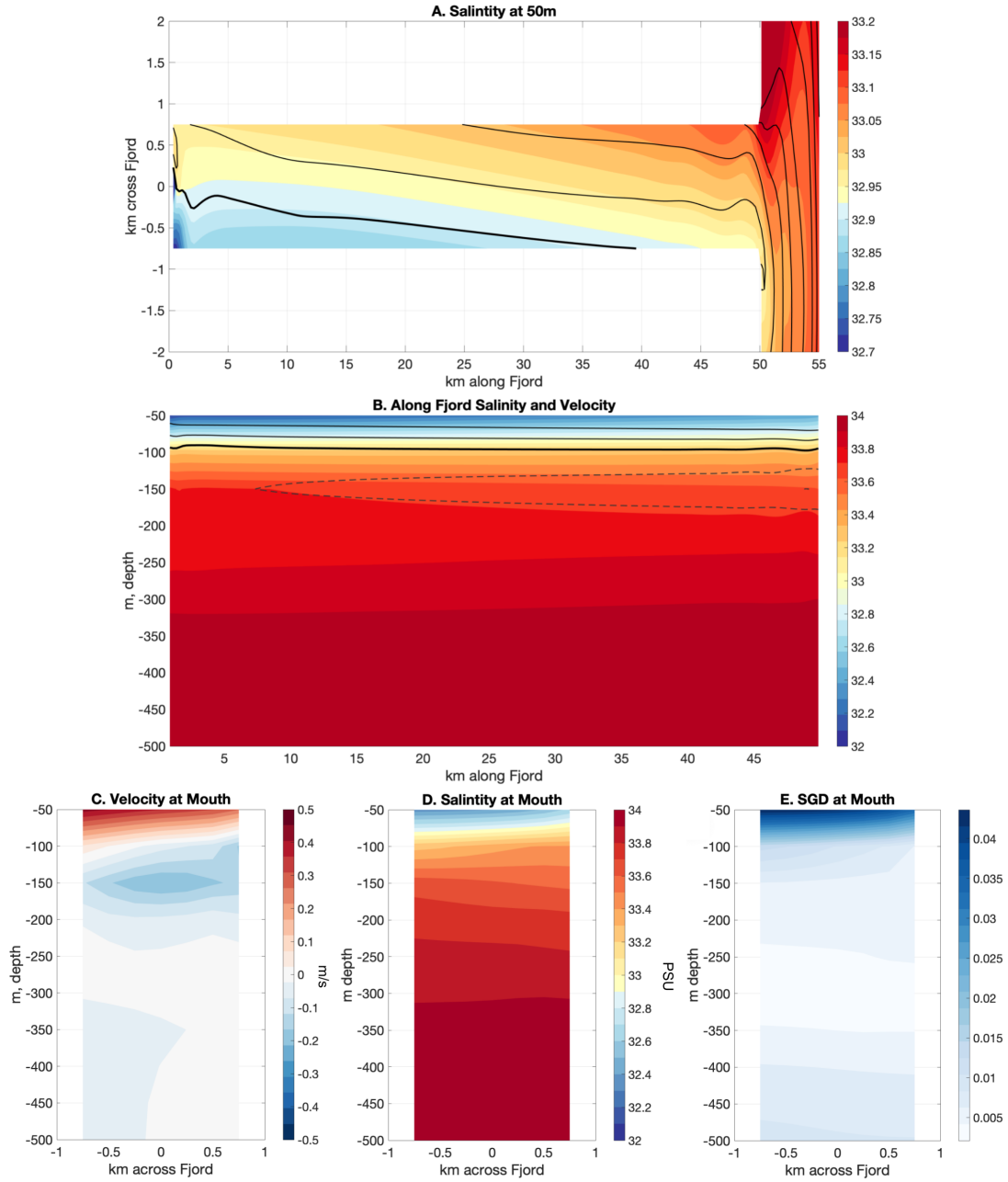

Figure 3.3. MITgcm simulation output for the one-Rossby-Radius-wide Case after 12 days. (A) salinity in top layer of the model with contours of dye tracer. (B) Along-fjord average salinity with contours of along fjord velocity; solid lines $u = 0.1$ and 0.2 m/s, dashed line $u = -0.1$ m/s, and thick line $u = 0$ m/s. Cross-fjord sections at the fjord mouth of (C) along-fjord velocity, (D) salinity, and (E) subglacial discharge tracer (g/kg).

Table 3.3. Comparison of idealized fjord simulations and various estimates of GMW salinity and volume transport. The root-mean-square error (RMSE) for the four subglacial discharge levels Q_R = 100, 500, 900, and 1,300 m^3/s is listed for S_{UM} and Q_{UM}. The coefficients of the relationship $Q_{UM} = aQ_R^b$ are given for each setup; this fit type is based on the results of Cowton et al. (2016).

Model	W	RMSE(S_{UM})	RMSE(Q_{UM}/W), m^3/s/m	a	b
MITgcm Rossby 1	2000 m			299	0.65
Cowton et al. (2016)	2000 m	0.25	3.05	1,134	0.49
FBM (dynamic h)	2000 m	0.30	3.98	2,743	0.36
FBM $h = 400$ m	2000 m	0.31	2.30	2,452	0.35
LPM	2000 m	0.32	8.15		
MITgcm 2D	250 m			670	0.45
Cowton et al. (2016)	250 m	0.73	59.5		
FBM (dynamic h)	250 m	0.19	7.65	1,271	0.38
FBM $h = 400$ m	250 m	0.41	4.34	1,118	0.37
LPM	250 m	0.58	36.9		

derived an empirical relationship between subglacial discharge and exchange circulation strength, which is also included in our comparison. First, we compare to the idealized MITgcm simulations which are simpler than a real fjord. Next we tune (e.g., adjust input values) the FBM and LPM to optimally represent two fjords where there are observations of GMW properties.

3.4.1 Idealized Simulations

The comparison between the idealized simulations and parameterizations is shown in Figure 3.4 and summarized in Table 3.3. The root-mean-square error (RMSE) of S_{UM} and Q_{UM} relative to the MITgcm simulations for the four subglacial discharge levels Q_R = 100, 500, 900, and 1,300 m^3/s is listed. In Figure 3.4, the relationships between S_{UM} (A,C) and Q_{UM} (B,D) versus Q_R are plotted for the two cases. The Cowton Empirical Relationship (CER; Cowton et al., 2016) can be used to find the salinity of exported water using the Knudsen relationship based on salt conservation in the fjord (MacCready et al., 2010). The LPM and CER parameterizations do not depend on the fjord width directly. However, the CER was based on exchange from a one-Rossby radius wide fjord.

The quasi-two-dimensional idealized fjord simulation is most similar to the FBM, and

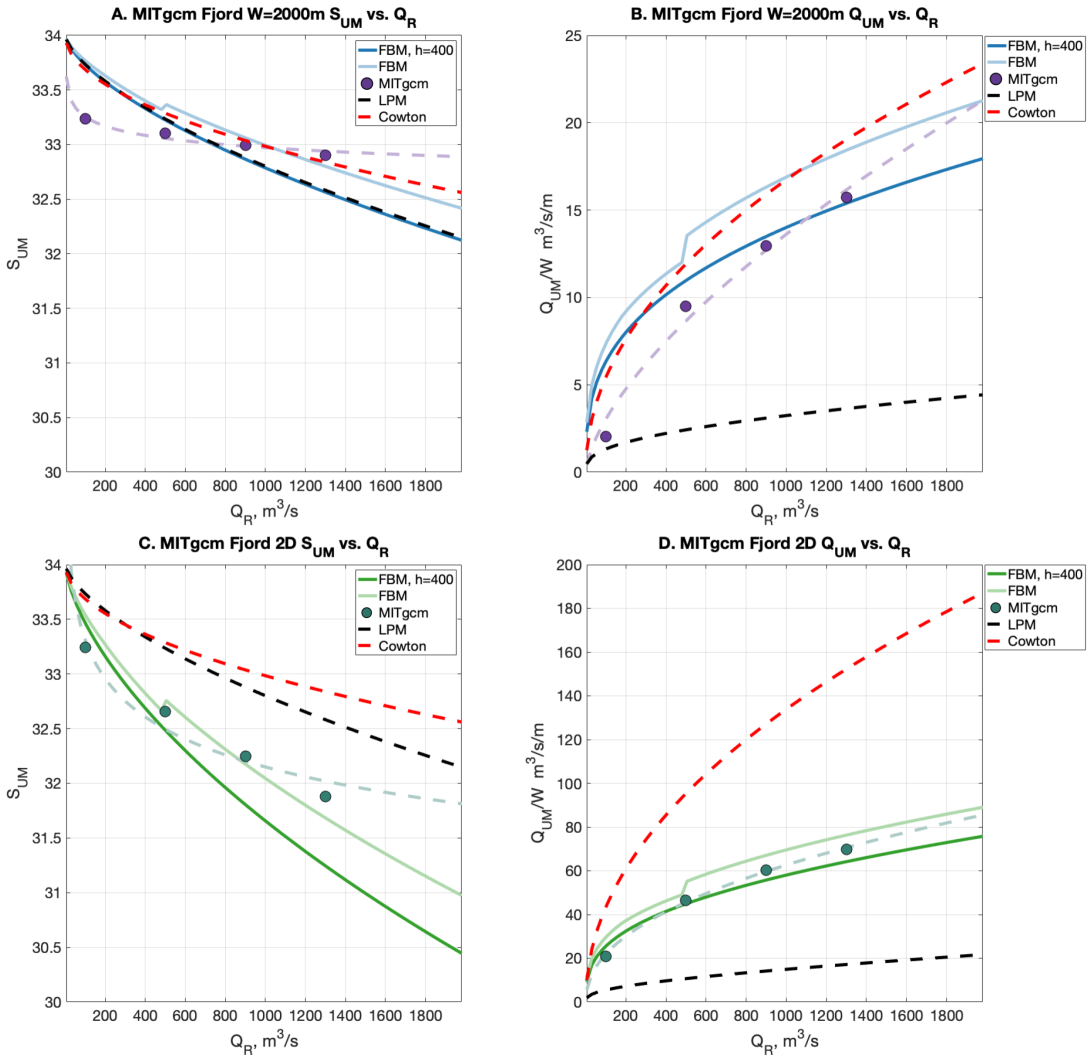

Figure 3.4. Comparison of the MITgcm simulations to FBM, LPM, and an exchange estimate from Cowton et al. (2016). Panels (A-B) are for the W=2,000 m fjord and (C-D) are for the quasi-2D W=250 m fjord. The circles are the results of the MITgcm simulations with a purple (A-B) or teal (C-D) dashed line that represents a fit of the form $Q_{UM} = aQ_R^b$. The FBM with set $h = 400$ m is the dark blue (A-B) and dark green (C-D) lines. The FBM with a dynamic h based on the LPM is the light blue (A-B) and light green (C-D). The LPM is the black dashed line. The red dashed line is exchange relationship from Cowton et al. (2016) in (B and D) and the salinity out of the fjord based on Knudsen relationship and the exchange relationship.

the predicted GMW salinity has the smallest error (0.19 PSU, see lower portion of Table 3.3) for the FBM with dynamic h. The RMSE in the volume flux out of the fjord is smallest for the FBM with $h = 400$ m; the RMSE error is small relative to the volume flux out of the fjord in both versions of the FBM. The relationship between Q_R and Q_{UM} is similar for both the dynamic plume height FBM and the FBM with a prescribed plume height value. The LPM significantly underestimates the volume flux out of the fjord. While the CER significantly overestimates the exchange flux for the quasi-2D idealized simulations, the value of b in the CER is similar to the fit to the idealized simulation. The FBM (dynamic or prescribed h) is able to estimate the GMW salinity and exchange circulation strength for an idealized quasi-2D fjord across a range of subglacial discharge values.

When the fjord is wide enough to allow for across-fjord structure (upper portion of Table 3.3), the skill of the FBM decreases. The RMSE error of the FBM compared to the one-Rossby radius wide simulation is ~ 0.30 PSU for both dynamic and prescribed plume height. The FBM does a particularly poor job of estimating the GMW salinity when Q_R=100 m^3/s. The GMW salinity in the FBM with $h = 400$ m is nearly identical to the LPM, indicating little vertical mixing in the fjord. The volume flux out of the fjord in the FBM is similar to the CER. Both the FBMs and the CER overestimate the volume flux compared to the idealized simulation. The LPM volume flux is much weaker than the idealized simulations; a wider plume would be needed to achieve similar levels of volume exchange.

3.4.2 Observations

In both Sermilik Fjord and Upernavik Fjord, there are observations of shelf water and GMW properties (Beaird et al., 2018a; Muilwijk et al., 2022). We configure the FBM for each fjord and compare to the available data. There is considerable uncertainty in the observed properties and the volume of subglacial discharge entering each system.

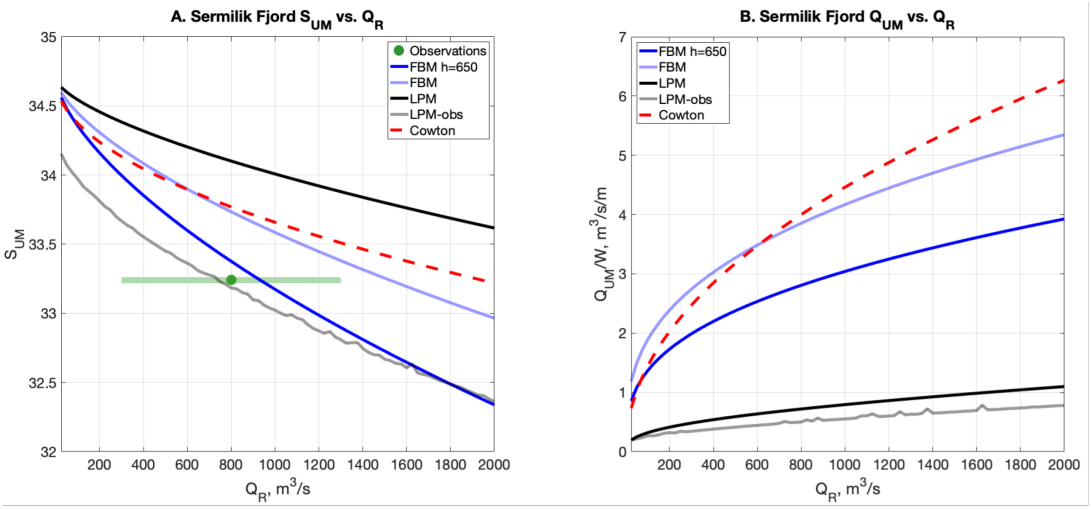

Figure 3.5. Comparison to observations from Beaird et al. (2018a). In panel A the observed transport weighted average salinity is the green circle, the light green bar indicates the uncertainty in the subglacial discharge. The blue lines are the results of the FBM; dark blue is $h = 650$ m, light blue is dynamic h. The analytic solution to the LPM using the shelf properties is plotted in black, a numerically integrated solution to the buoyant plume equations using the observed T (°C) and S profiles is in gray. The CER is the red dashed line.

Sermilik Fjord, East Greenland

Sermilik Fjord is a well observed fjord in Southeast Greenland. Within the fjord, there is a deep layer (below 200 m) of warm Atlantic origin water that drives melting of the ice sheet (see Straneo et al., 2010, 2016; Sanchez et al., 2021, and others). For the FBM, we consider the fjord to be 90 km long, 7.5 km wide and 900 m deep. Observations of noble gasses were collected in Sermilik Fjord in 2018 and used as additional tracers to constrain water masses in the fjord (Beaird et al., 2018a). The resulting GMW was observed over the upper 200 m of the fjord. The transport weighted average salinity was 33.24 and the exchange flow was 74,000 m^3/s. The estimated subglacial discharge exported from Sermilik fjord was 800±500 m^3/s (Beaird et al., 2018a).

We compare the observed values of GMW salinity and volume flux to the FBM case with $h = 650$ m, a dynamic h based on the LPM, the LPM using the shelf water properties, the buoyant plume model using the observed fjord-averaged T and S profiles, and the CER. The

results of the parameterizations are plotted in Figure 3.5. For the FBM, $\kappa_v/dz = 10^{-5}$ m/s and $W_p = 25$. The choice of S_{LM}=34.69 and T_{LM}=3.3°C are from observations of shelf properties below 200 m, also from Beaird et al. (2018a).

The FBM (dynamic or prescribed h) overestimates the salt flux out of the fjord. The dynamic height plume has a 0.49 PSU error while the FBM with $h = 650$ m has an error of just 0.13 PSU for Q_R=800 m^3/s. The LPM alone has an even greater error of 0.86 PSU, while the buoyant plume model run using the observed stratification has an error of 0.06 PSU. The salinity predicted by the CER is similar to the dynamic h FBM; Sermilik Fjord is roughly one Rossby radius wide (Jackson et al., 2018) like the fjord on which the CER is based. The observed volume flux out of the fjord is much greater than any of the models; with the observed volume flux per unit width of $\sim$10 m^3/s/m. The LPM and the buoyant plume model have the weakest exchange flows, showing how much the estuarine circulation amplifies the plume dynamics. The dynamic height FBM and the Cowton et al. (2016) study agree for the Sermilik configuration. One reason the models may be underestimating the exchange flow is that they do not include any submarine melting. Sermilik Fjord has many icebergs, which melt as they drift in the fjord (Moon et al., 2018). The presence of icebergs and the buoyancy associated with their melt has been shown to increase fjord exchange circulation (Davison et al., 2020). The estimated submarine melting in Sermilik Fjord (both icebergs and the glacier face) was 1,300$\pm$100 m^3/s (Beaird et al., 2018a).

Upernavik Fjord, West Greenland

Upernavik Fjord is connected to Baffin Bay, and five glaciers feed into it. Muilwijk et al. (2022) used observations from six years between 2013-2019 (no data for 2014) to estimate the components of GMW in the fjord. In their analysis, the GMW layer was defined using differences in the shelf and fjord properties as the layer with the maximum temperature and salinity anomalies. The average composition of the GMW was 57.8%$\pm$8.1% Atlantic, 41.0%$\pm$8.3% polar water, 1.0%$\pm$0.1% subglacial discharge, and 0.2%$\pm$0.2% submarine meltwater (Muilwijk et al., 2022). With limited data, the relative importance of polar water or Atlantic water in setting GMW

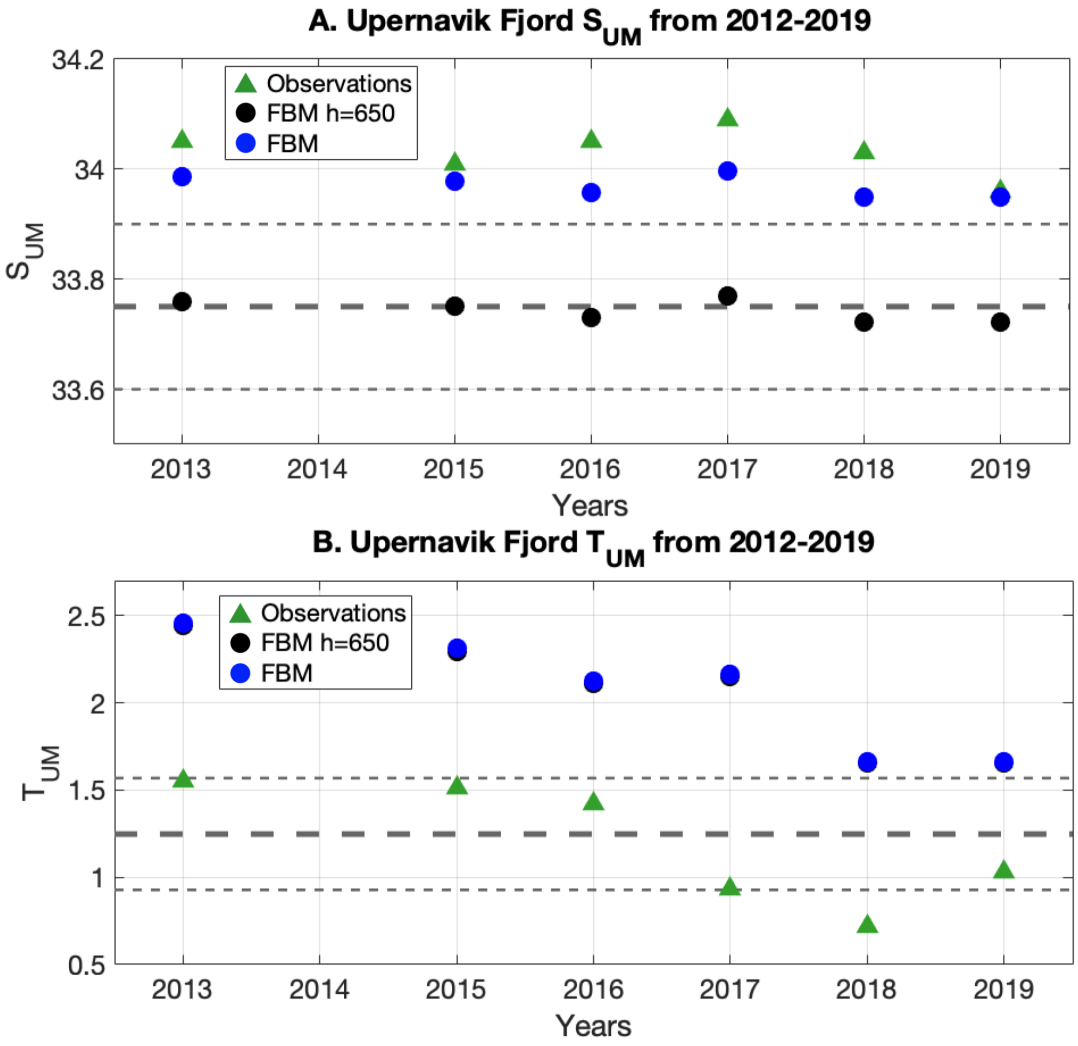

Figure 3.6. Salinity (A) and temperature (°C) (B) of GMW layer in Upernavik Fjord for 2013-2019 (no data for 2014). Observations from Muilwijk et al. (2022) are the green triangles. The blue circles are the FBM with a dynamic h, and black circles are the FBM with $h = 650$ m (GMW layer is 0-250 m). The thick dashed line is the average (A) salinity or (B) temperature of the upper 250 m from observations in all years; the thin dashes lines are one standard deviation. The GMW layer is a subset of the upper 250 m, see text for definition of the GMW used by Muilwijk et al. (2022). Note, in (B) the FBM GMW temperature values are nearly identical, thus the black and blue circles are hard to distinguish.

properties was undetermined (Muilwijk et al., 2022). The average temperature and salinities from the upper 250 m of the fjord were also reported by Muilwijk et al. (2022). Averaging the upper 250 m is similar to how GMW is defined in the FBM and therefore are also presented here for comparison.

For Upernavik Fjord, we use a length of 60 km, width of 6 km, and depth of $H =$ 900 m. For the FBM, $\kappa_v/dz = 10^{-5}$ m/s and W_p=25 m. For each year, the observed Atlantic water temperature and salinity values are used, the average of the six years is S_{LM}=34.71 and T_{LM}=2.1°C. We compare the observations to two configurations of the FBM, one with a static $h = 650$ m and one with a dynamic h. The properties of the observed FBM-modeled GMW are plotted in Figure 3.6. Despite the large fraction of polar water, the FBM is a good predictor of GMW salinity. With a dynamic h, the FBM RMSE(S_{UM})=0.07 across the six years. With static h, we compare to the properties in the upper 250 m of the fjord (dashed line in Figure 3.6) and find that the FBM predicts the salinity within one standard deviation and with an RMSE(S_{UM})=0.02. While the water mass components of the GMW in Upernavik Fjord make it clear that the FBM is missing key components of GMW, the resulting salinities are very similar to observations. The RMSE(S_{UM}) in the FBM with $h = 650$ is 0.29 PSU which decreases to 0.07 PSU when a dynamic h is used. The FBM temperature is too high with both a dynamic and static h. This is likely because both polar water and submarine meltwater are absent in the FBM. However, the importance of polar water in setting the properties of GMW in Upernavik Fjord is unclear from the available observations (Muilwijk et al., 2022).

3.5 Discussion and Conclusion

We have developed a two-layer Fjord Box Model that includes a subglacial discharge plume to parameterize the mixing of meltwater from the GIS that occurs within glacial fjords. The FBM is a modified version of the Sun et al. (2017) EBM, where the riverine boundary conditions are replaced by a buoyant plume (Slater et al., 2016). The resulting FBM produces

more dilution of meltwater and a greater exchange circulation than the buoyant plume model alone. This suggests that calculating fjord exchange based only on plume entrainment may underestimate the strength of circulation within fjords (Slater et al., 2022).

We find that the FBM is most sensitive to changes in parameters that impact plume entrainment, and we focus in particular on plume height. We estimate plume height using either the Line Plume Model or fixed values informed by observations. Because the FBM only has two layers, the buoyant plume reaches the surface rather than achieving neutral buoyancy at some depth. We find that using a fixed plume height informed by observations can provide a better representation of glacially modified water properties than by using dynamic height. The vertical mixing within the fjord must be sufficiently small for the FBM to have a solution.

Overall the FBM is able to approximate the salinity of GMW and the strength of the exchange circulation in idealized models and when compared to available observations. The salinity of GMW in an idealized fjord was best reproduced by the FBM with a dynamic plume height. The FBM with specified plume height did the best at reproducing observed GMW salinity; the observed depth of the GMW layer was used to inform the plume height. The FBM is not able to match the observed temperature of exported GMW, likely because of the importance of polar water and submarine melting, which are not represented in the FBM, in setting the temperature. The FBM provides a reasonable estimate of the exchange circulation in the idealized fjord simulations. However, the FBM outgoing volume flux is roughly half of that observed in Sermilik Fjord. This suggests that the error results from processes that are not included in either the FBM or the idealized models.

The goal of the FBM is to provide a parameterization of the within-fjord mixing of zero-salinity runoff from the GIS and the ambient shelf water for use in an ESM. However, the FBM lacks any representation of submarine melting, which results in GMW that is too warm. The FBM could be improved by adding an additional box to represent polar water or including heat fluxes associated with submarine melting. The FBM could also be modified to represent more of the complex bathymetry within fjords, such as sills. We have shown that the

FBM can produce GMW salinity similar to observations, and suggest that is would offer an improvement over adding zero-salinity runoff to the surface layer of the ocean. Future work includes implementing the FBM and assessing the impacts on stratification and sea surface salinity in the Subpolar North Atlantic.

Acknowledgments

T.J. Morrison, J.L. McClean and S.T. Gille were funded by DOE Office of Science grants: DE-SC0014440 and DE-SC0020073. T.J. Morrison was supported by the National Center for Atmospheric Research's Advanced Study Program's Graduate Student (GVP) Fellowship to collaborate with F. Bryan and G. Marques. Data from Upernavik Fjord referenced in this study (2013–19) is publicly available at the online Arctic Data Center repository: doi:10.18739/A2SJ19S1Q. Data from Sermilik Fjord referenced in this study is accessible online at the NOAA National Centers for Environmental Information: http://accession.nodc.noaa.gov/0171277. We would like to thank Scott Bachman and Alex Hager for guidance when configuring the MITgcm Simulations. We thank Donald Slater for numerical model of the subglacial discharge plume. We thank Fiammetta Straneo for her insights into fjord dynamics.

Chapter 3, is coauthored with Bryan, Frank; McClean, Julie; Gille, Sarah; Marques, Gustavo. The dissertation author was the primary author of this chapter.

Chapter 4

Conclusions and Future Work

This thesis explores the connection between the Subpolar North Atlantic Ocean and the Greenland Ice Sheet (GIS) using high resolution ocean models. In the first chapter, we focused on the transport of heat onto the continental shelf. We found in two eddy-permitting coupled ocean/sea-ice simulations that eddies generated by the Denmark Strait Overflow modified this cross-isobath heat transport. In one simulation, the eddies contributed to on-shelf heat flux, while in the other simulation the eddies opposed the mean on-shelf heat flux. Further study is needed, likely with higher resolution to improved the representation of the Denmark Strait Overflow eddies, to understand their contribution to on-shelf heat fluxes.

In the next chapter, we presented a comparison of mesoscale eddy resolving ocean simulations with different representations of meltwater fluxes from the GIS. In one simulation, meltwater was added to the upper 10 m of the ocean, consistent with previous studies. In the other simulation, meltwater is vertically distributed over the upper 200 m to represent the dilution of meltwater within glacial fjords. We found that vertically distributing meltwater increases the transport of freshwater into the Labrador Sea. These simulations were compared over a relatively short period (two years), but the vertically distributed simulation will be run for a total of 20 years from 1990-2009. With a longer record, this simulation can be used to explore the impact of meltwater on deep water formation in the Subpolar North Atlantic. Using a dye tracer added with the meltwater, the pathways of meltwater over 20 years can be found. The period

from 1990-2009 includes a shift in the phase of the North Atlantic Oscillation and the increase in GIS runoff. This 20 year long global mesoscale eddy resolving simulation can also be used to study the connection between the freshwater budgets of the Arctic and Subpolar North Atlantic Oceans.

The simple vertical distribution used in the simulations presented in the second chapter did not take into account any spatial variability around Greenland. To improve the representation of mixing within glacial fjords we modified a riverine estuary box model to include a subglacial discharge plume. By comparing to both observations and idealized simulations, we found the Fjord Box Model was able to predict the salinity of glacially modified water within 1 PSU. However, the Fjord Box Model under-predicts exchange circulation strength and glacially modified water temperature. The Fjord Box Model could be improved by including a representation of submarine melting, Polar Water, or complex bathymetry. The Fjord Box Model could be implemented in an Earth System Model to better represent the buoyancy forcing from ice sheet runoff.

Many challenges remain in long-term projections of the mass loss of the GIS. This thesis has explored how the ocean contributes to that melting, the subsequent impact of that meltwater on the ocean, and an improvement to representing meltwater in Earth System Models. This work also emphasizes the importance of mesoscale eddy processes in the transport of ocean heat and freshwater at the Greenland continental shelf break. Resolving or accurate parameterization of these processes is essential for realistic models of ice sheet and ocean interactions in this region.

Appendix A

Fjord Box Model: Derivation

Th Fjord box model (FBM) has 3 boxes: the plume, the upper fjord, and the lower fjord. The domain is $-L < x < 0$ with $x = -L$ at the plume box and $x = 0$ at the shelf. The surface is a rigid lid at $z = H$ and the interface is at $z = h$, with the bottom at $z = 0$. The fjord is uniform in the y-direction, $\partial/\partial y = 0$ and the fjord has width W.

A.1 Along Fjord Gradients

The density within the fjord is given by a linear equation of state: $\rho = \rho_0(1 + \beta_S S - \beta_T T)$. In each layer, the properties varies linearly along the fjord:

$$\rho(x,z) = \begin{cases} \frac{\rho_{UM}-\rho_{UP}}{L}x + \rho_{UM} & \text{for } H > z > h, \\ \\ \frac{\rho_{LM}-\rho_{LP}}{L}x + \rho_{LM} & \text{for } h > z > 0. \end{cases} \tag{A.1}$$

Similarly

$$S(x,z) = \begin{cases} \frac{S_{UM}-S_{UP}}{L}x + S_{UM} & \text{for } H > z > h, \\ \\ \frac{S_{LM}-S_{LP}}{L}x + S_{LM} & \text{for } h > z > 0, \end{cases} \tag{A.2}$$

and

$$T(x,z) = \begin{cases} \frac{T_{UM}-T_{UP}}{L}x + T_{UM} & \text{for } H > z > h, \\ \\ \frac{T_{LM}-T_{LP}}{L}x + T_{LM} & \text{for } h > z > 0. \end{cases} \tag{A.3}$$

The vertical velocity is linear defined to be zero at the bottom and the surface, and maximum at the interface:

$$w(z) = \begin{cases} \frac{H-z}{H-h}w_I & \text{for } H > z > h \\ \\ \frac{z}{h}w_I & \text{for } h > z > 0 \end{cases} \tag{A.4}$$

and from the conservation of volume, we can define $w_I = (Q_{LM} - Q_{LP})/LW$.

The fluxes in and out of the plume box come from the four equation 1-D plume equations. The volume flux out comes from the volume conservation within the plume and the associated temperature and salinity are the average of the plume properties shallower than the layer interface $z = h$.

A.2 Conservation of Volume

Integrating the continuity equation

$$\frac{\partial u}{\partial x} + \frac{\partial w}{\partial z} = 0 \tag{A.5}$$

from $-L < x < 0$ and $0 < z < H$, and multiplying by W we can write a conservation of volume for the entire system:

$$Q_{LM} - Q_{LP} + Q_{UM} - Q_{UP} = 0 \tag{A.6}$$

Note, by definition the volume fluxes of the FBM have prescribed signs: $Q_{LM} < 0$, $Q_{LP} < 0$, $Q_{UM} > 0$, and $Q_{UP} > 0$.

We can integrate (A.5) for the lower layer from $-L < x < 0$ and $h < z < H$:

$$\int_0^h u|_{-L}^0 dz + \int_{-L}^0 w|_0^h dx = \tag{A.7}$$

$$\int_0^h (u_{LM} - u_{LP}) dz + \int_{-L}^0 w_I dx = \tag{A.8}$$

$$h(u_{LM} - u_{LP}) - L w_I = 0. \tag{A.9}$$

Multiplying by W

$$Wh(u_{LM} - u_{LP}) - WLw_I = 0, \tag{A.10}$$

$$Q_{LM} - Q_{LP} - WLw_I = 0, \tag{A.11}$$

$$w_I = \frac{(Q_{LM} - Q_{LP})}{LW} \tag{A.12}$$

thus showing our definition of w_I. We can also define $Q_V = w_I LW$ which is the vertical volume flux between the upper and lower layers. Similarly, $Q_V = Q_{UM} - Q_{UP}$.

For the plume box, the volume conservation equation is

$$Q_R - Q_{LP} = Q_{UP}. \tag{A.13}$$

Therefore

$$Q_{LM} + Q_{UM} - Q_R = 0. \tag{A.14}$$

A.3 Conservation of Salt

Integrating the steady state advection diffusion equation

$$\frac{\partial uS}{\partial x} + \frac{\partial wS}{\partial z} = \frac{\partial}{\partial x}\left(k_H \frac{\partial S}{\partial x}\right) + \frac{\partial}{\partial z}\left(k_v \frac{\partial S}{\partial z}\right) \tag{A.15}$$

from $-L < x < 0$ and $0 < z < H$, and multiplying by W we can write a conservation of salt for the entire system:

$$S_{LM}Q_{LM} - S_{LP}Q_{LP} + S_{UM}Q_{UM} - S_{UP}Q_{UP} = 0. \tag{A.16}$$

and for the subglacial discharge plume

$$S_{LP}Q_{LP} + S_{UP}Q_{UP} = 0. \tag{A.17}$$

So we can say more simply:

$$S_{LM}Q_{LM} + S_{UM}Q_{UM} = 0. \tag{A.18}$$

Conservation of Salt in the lower layer

We use the conservation of salt in the lower layer to constrain the salinity entering the plume S_{LP}. Therefore integrating A.15 term by term for $-L < x < 0$ and $0 < z < h$ we have:

$$\int_0^h dz \int_{-L}^0 dx \frac{\partial uS}{\partial x} = hu_{LM}S_{LM} - hu_{LP}S_{LP}, \tag{A.19}$$

$$\int_0^h dz \int_{-L}^0 dx \frac{\partial wS}{\partial z} = \int_{-L}^0 dx w_I S_L(x) = \frac{w_I L}{2}(S_{LM} - S_{LP}), \tag{A.20}$$

$$\int_0^h dz \int_{-L}^0 dx \frac{\partial}{\partial x}\Big(k_H \frac{\partial S}{\partial x}\Big) = \kappa_v \int_0^h dz \Big(\frac{\partial S_{LM}}{\partial x} - \frac{\partial S_{LP}}{\partial x}\Big) = 0, \tag{A.21}$$

which are the horizontal advection, vertical advection, and horizontal diffusion terms, respectively. For the vertical diffusion term, we need to define $\partial S/\partial z = (S_U - S_L)\delta(h-z)$ where δ is the Dirac Delta function. Given: $S(x,z) = S_L(x) + (S_U(x) - S_L(x))H(h-z)$ and H is the heavy side function.

$$\int_0^h dz \int_{-L}^0 dx \frac{\partial}{\partial z}\Big(k_v \frac{\partial S}{\partial z}\Big) = \kappa_v \int_{-L}^0 dx \Big(\frac{\partial S}{\partial z}\Big)\Big|_0^h \tag{A.22}$$

$$= \kappa_v \int_{-L}^0 dx \Big((S_U - S_L)\delta(h-z)\Big)\Big|_0^h \tag{A.23}$$

$$= \frac{\kappa_v}{dz} \int_{-L}^0 dx (S_U(x) - S_L(x)) \tag{A.24}$$

$$= \frac{\kappa_v L}{2dz}\Big(S_{LM} - S_{UM} + S_{LP} - S_{UP}\Big). \tag{A.25}$$

Multiplying each term by W and combining these terms we have:

$$Q_{LM}S_{LM} - Q_{LP}S_{LP} + \frac{(Q_{LM} - Q_{LP})}{2}(S_{LM} - S_{LP}) = \frac{\kappa_v A}{2dz}\Big(S_{LM} - S_{UM} + S_{LP} - S_{UP}\Big). \tag{A.26}$$

A.4 Conservation of Heat

There are no sources or sinks of heat in the FBM, thus heat is conserved.

A.5 Conservation of PE

The Potential Energy (PE) equation comes from applying the equation of state to the temperature and salinity advection diffusion equations

$$\frac{\partial u\mathrm{PE}}{\partial x} + \frac{\partial w\mathrm{PE}}{\partial z} = \frac{\partial}{\partial x}\Big(k_H \frac{\partial \mathrm{PE}}{\partial x}\Big) + \frac{\partial}{\partial z}\Big(k_v \frac{\partial \mathrm{PE}}{\partial z}\Big) - k_v g \frac{\partial \rho}{\partial z} - g\frac{\partial k_v \rho}{\partial z} + wg\rho. \tag{A.27}$$

Each term is integrated from $-L < x < 0$ and $0 < z < H$ in the following sections. Note: $\mathrm{PE} = \rho g z$.

A.5.1 x-Advection

$$\int_{-L}^{0} dx \int_{0}^{H} dz \Big(\frac{\partial u \mathrm{PE}}{\partial x} \Big) = \int_{0}^{H} dz (ugz\rho)|_{-L}^{0} \tag{A.28}$$

$$= g \int_{0}^{h} dz (u_{LM}\rho_{LM} - u_{LP}\rho_{LP}) + g \int_{h}^{H} dz (u_{UM}\rho_{UM} - u_{UP}\rho_{UP}) \tag{A.29}$$

$$= (g/2) \Big[h^2 (u_{LM}\rho_{LM} - u_{LP}\rho_{LP}) + (H^2 - h^2)(u_{UM}\rho_{UM} - u_{UP}\rho_{UP}) \Big] \tag{A.30}$$

A.5.2 z-Advection

$$\int_{-L}^{0} dx \int_{0}^{H} dz \Big(\frac{\partial w \mathrm{PE}}{\partial z} \Big) = 0 \tag{A.31}$$

A.5.3 x-diffusion

$$\int_{-L}^{0} dx \int_{0}^{H} dz \frac{\partial}{\partial x} \Big(\kappa_v \frac{\partial \mathrm{PE}}{\partial x} \Big) = \kappa_v \int_{0}^{H} dz \left(\frac{\partial \rho g z}{\partial x} \right) \Bigg|_{-L}^{0} = \kappa_v g \int_{0}^{H} z \left(\frac{\partial \rho}{\partial x} \right) \Bigg|_{-L}^{0} dz \tag{A.32}$$

$$= \kappa_v g \left(\int_{0}^{h} z \Big(\frac{\partial \rho_{LM}}{\partial x} - \frac{\partial \rho_{LP}}{\partial x} \Big) dz + \int_{h}^{H} z \Big(\frac{\partial \rho_{UM}}{\partial x} - \frac{\partial \rho_{UP}}{\partial x} \Big) dz \right) \tag{A.33}$$

$$= 0 \tag{A.34}$$

This is because there are no step changes in salinity (in x) at the mouth or plume.

A.5.4 z-diffusion

$$\int_{-L}^{0} dx \int_{0}^{H} dz \frac{\partial}{\partial z}\Big(\kappa_v \frac{\partial \mathrm{PE}}{\partial z}\Big) \tag{A.35}$$

$$= g\kappa_v \int_{-L}^{0} dx \Big(\frac{\partial z\rho}{\partial z}\Big)\Big|_0^H \tag{A.36}$$

$$= g\kappa_v \int_{-L}^{0} dx \Big(\rho \frac{\partial z}{\partial z} + z\frac{\partial \rho}{\partial z}\Big)\Big|_0^H \tag{A.37}$$

$$= g\kappa_v \left(\int_{-L}^{0} dx \Big(\rho + z\frac{\partial \rho}{\partial z}\Big)\Big|_0^h + \int_{-L}^{0} dx \Big(\rho + z\frac{\partial \rho}{\partial z}\Big)\Big|_h^H \right) \tag{A.38}$$

$$= g\kappa_v \left(\int_{-L}^{0} dx \Big(\rho_L + z(\rho_U - \rho_L)\delta(h-z)\Big)\Big|_0^h + \int_{-L}^{0} dx \Big(\rho_U + z(\rho_U - \rho_L)\delta(h-z)\Big)\Big|_h^H \right) \tag{A.39}$$

$$= g\kappa_v \int_{-L}^{0} dx \left(\Big(\rho_L + h(\rho_U - \rho_L) - \rho_L\Big) + \Big(\rho_U - (\rho_U + h(\rho_U - \rho_L))\Big) \right) \tag{A.40}$$

$$= g\kappa_v \int_{-L}^{0} dx \Big(h(\rho_U - \rho_L) - h(\rho_U - \rho_L) \Big) \tag{A.41}$$

$$= 0. \tag{A.42}$$

A.5.5 Term 5 and 6

We can combine these terms if $\partial \kappa_v / \partial z = 0$.

$$-2\kappa_v g \int_{-L}^{0} dx \int_{0}^{H} dz \frac{\partial \rho}{\partial z} = -2\kappa_v g \int_{-L}^{0} dx \int_{0}^{H} dz (\rho_U - \rho_L)\delta(h-z) \tag{A.43}$$

$$= -2\kappa_v g \int_{-L}^{0} dx (\rho_U - \rho_L) \tag{A.44}$$

$$= -2\kappa_v g \int_{-L}^{0} dx \left(\frac{\rho_{UM} - \rho_{UP}}{L} x + \rho_{UM} \right) - \left(\frac{\rho_{LM} - \rho_{LP}}{L} x + \rho_{LM} \right) \tag{A.45}$$

$$= -2\kappa_v g \int_{-L}^{0} dx \left(\frac{\rho_{UM} - \rho_{UP} - \rho_{LM} + \rho_{LP}}{L} x + (\rho_{UM} - \rho_{LM}) \right) \tag{A.46}$$

$$= -2\kappa_v g \left(\frac{\rho_{UM} - \rho_{UP} - \rho_{LM} + \rho_{LP}}{L} \frac{x^2}{2} + (\rho_{UM} - \rho_{LM}) x \right) \Bigg|_{-L}^{0} \tag{A.47}$$

$$= 2\kappa_v g \left(\frac{\rho_{UM} - \rho_{UP} - \rho_{LM} + \rho_{LP}}{L} \frac{L^2}{2} - L(\rho_{UM} - \rho_{LM}) \right) \tag{A.48}$$

$$= \kappa_v g L \Big(\rho_{UM} - \rho_{UP} - \rho_{LM} + \rho_{LP} - 2(\rho_{UM} - \rho_{LM}) \Big) \tag{A.49}$$

$$= \kappa_v g L \Big(\rho_{LM} - \rho_{UM} + \rho_{LP} - \rho_{UP}) \Big) \tag{A.50}$$

Important in this is the definition of $\partial \rho / \partial z = (\rho_U - \rho_L)\delta(h-z)$ where δ is the Dirac Delta function. Given: $\rho(x,z) = \rho_L(x) + (\rho_U(x) - \rho_L(x))H(h-z)$ and H is the heavy side function.

A.5.6 Term 7

$$\int_{-L}^{0} dx \int_{0}^{H} dz w g \rho = g \int_{-L}^{0} \int_{0}^{H} w(z) \rho(x,z) dz dx = \tag{A.51}$$

$$g \int_{-L}^{0} dx \Big[\rho_L(x) \int_{0}^{h} dz w_I \frac{z}{h} + \rho_U(x) \int_{h}^{H} dz w_I \frac{H-z}{H-h} \Big] = \tag{A.52}$$

$$g \int_{-L}^{0} dx \Big[\rho_L(x) \frac{w_I}{h} \int_{0}^{h} z dz + \rho_U(x) \frac{w_I}{H-h} \int_{h}^{H} (H-z) dz \Big] = \tag{A.53}$$

$$g \int_{-L}^{0} dx \Big[\rho_L(x) \frac{w_I}{h} \frac{z^2}{2} \Big|_0^h + \rho_U(x) \frac{w_I}{H-h} \Big(Hz - \frac{z^2}{2} \Big) \Big|_0^h \Big] = \tag{A.54}$$

$$g \int_{-L}^{0} dx \Big[\rho_L(x) \frac{w_I h}{2} + \rho_U(x) \frac{w_I}{2} (H-h) \Big] = \tag{A.55}$$

$$g \Big[\frac{w_I h}{2} \int_{-L}^{0} dx \rho_L(x) + \frac{w_I}{2} (H-h) \int_{-L}^{0} dx \rho_U(x) \Big] = \tag{A.56}$$

$$\frac{g w_I L}{4} \Big[h(\rho_{LM} + \rho_{LP}) + (H-h)(\rho_{UM} + \rho_{UP}) \Big]. \tag{A.57}$$

Therefor we can combine full integration of (A.27) as

$$(g/2) \Big[h^2 (u_{LM} \rho_{LM} - u_{LP} \rho_{LP}) + (H^2 - h^2)(u_{UM} \rho_{UM} - u_{UP} \rho_{UP}) = \tag{A.58}$$

$$\frac{g \kappa_v L}{2} \Big[(\rho_{LM} - \rho_{UM}) + (\rho_{LP} - \rho_{UP}) \Big] +$$

$$\frac{g w_I L}{4} \Big[h(\rho_{LP} + \rho_{LM}) + (H-h)(\rho_{UP} + \rho_{UM}) \Big].$$

We can multiply by W to convert the left hand side to fluxes,

$$(g/2)\Big[h(Q_{LM}\rho_{LM} - Q_{LP}\rho_{LP}) + (H+h)(Q_{UM}\rho_{UM} - Q_{UP}\rho_{UP}) = \tag{A.59}$$

$$\frac{g\kappa_v A}{dz2}\Big[\rho_{LM} - \rho_{UM} + \rho_{LP} - \rho_{UP}\Big] +$$

$$\frac{gQ_V}{4}\Big[h(\rho_{LP}+\rho_{LM}) + (H-h)(\rho_{UP}+\rho_{UM})\Big].$$

A.6 Plume equations

The equations for the plume are:

$$\frac{\partial(bu)}{\partial z} = \alpha u \tag{A.60}$$

$$\frac{\partial(bu^2)}{\partial z} = bg' \tag{A.61}$$

$$\frac{\partial(buT)}{\partial z} = \alpha u T_{LP} \tag{A.62}$$

$$\frac{\partial(buS)}{\partial z} = \alpha u S_{LP} \tag{A.63}$$

where b is the plume width, u is the vertical velocity of the plume, T is the temperature of the plume, and S is the salinity of the plume.

These equations can be solved for an unstratified fjord without considering any melting from the ice sheet as:

$$b(z) = \alpha(z+z_0) \tag{A.64}$$

$$u(z) = (Qg_0'/\alpha)^{1/3} \tag{A.65}$$

$$T(z) = T_{LP}[1 - z_0/(z+z_0)] \tag{A.66}$$

$$S(z) = S_{LP}[1 - z_0/(z+z_0)] \tag{A.67}$$

where

$$z_0 = (Q^2/\alpha^2 g_0')^{1/3} \tag{A.68}$$

$$g_0' = g(\beta_S S_{LP} - \beta_T T_{LP}). \tag{A.69}$$

From these equations we can calculate the entrainment of the plume:

$$Q_{LP} = -\int_0^h W_p \alpha u(z) dz = -W_p \alpha \int_0^h (Q g_0'/\alpha)^{1/3} dz \tag{A.70}$$

$$= W_p \alpha \int_0^h \left[\frac{g Q_R (\beta_S S_{LP} - \beta_T T_{LP})}{\alpha} \right]^{1/3} dz \tag{A.71}$$

$$= -h W_p \alpha^{2/3} \left(g Q_R (\beta_S S_{LP} - \beta_T T_{LP}) \right)^{1/3} \tag{A.72}$$

A.7 Simplifying FBM Equations

Because of the coupling of the plume, entrainment, and stratification of this system, we must solve for many of the variables simultaneously. To do this, we first eliminate redundant variables from the equations, then use Newton's method to find the roots of the system of equations.

The variables directly solved for are: $Q_{LM}, Q_{UM}, S_{UM}, T_{UM}, Q_{LP}, S_{LP}, T_{LP}, \rho_{LP}$, and ρ_{UM}. To do this, eliminate the variables: $Q_V, Q_{UP}, S_{UP}, T_{UP}$ and ρ_{UP}. The set of variables used in Newton's Method could be simplified further, but to keep the functions and their derivatives simple we chose to use these variables. In addition, the Jacobian Matrix, which needs to be inverted, will be sparse and small.

The main equations to eliminate upper-plume variables are:

$$Q_V = Q_{LM} - Q_{LP} \tag{A.73}$$

$$Q_{UP} = Q_R - Q_{LP} \tag{A.74}$$

$$S_{UP} = \frac{-S_{LP}Q_{LP}}{Q_R - Q_{LP}} \tag{A.75}$$

$$T_{UP} = \frac{-T_{LP}Q_{LP}}{Q_R - Q_{LP}} \tag{A.76}$$

$$\rho_{UP} = \frac{\rho_R Q_R - \rho_{LP}Q_{LP}}{Q_R - Q_{LP}} \tag{A.77}$$

Appendix B

Fjord Box Model: Newton's Method

B.1 Netwon's Method

Newton's Method is a standard way of finding the roots of a system of non-linear equations ($\vec{G}$). The method is iterative, and depends on an initial guess at the solution. The Jacobian (J) of $\vec{G}$ must be calculated and be able to be inverted. An initial guess is made, $\vec{x}_0$, then the system of equations and the Jacobian are evaluated at $\vec{x}_0$: $G_0 = \vec{G}(\vec{x}_0)$ and $J_0 = J(\vec{x}_0)$. Then we calculate $y_0 = J_0^{-1} G_0$, to find a new $\vec{x}_1 = \vec{x}_0 + y_0$. In general

$$\vec{x}_{i+1} = \vec{x}_i + J^{-1}(\vec{x}_i) G(\vec{x}_i). \tag{B.1}$$

This iteration is continued until $G(\vec{x}_i)$ is close to $\vec{0}$. The primary drawback of Newton's method is that if the initial guess is not sufficiently close to the root, then the iteration will diverge. For the FBM it is feasible to make a "good enough" first guess based on our physical understanding of the system. However, we cannot address another problem with root finding; there may be multiple roots of the system of equations. This is hard to assess in a system with

this many dimensions. Our initial guess is:

$$Q_{LM} = -1000 Q_R^3 \tag{B.2}$$

$$Q_{UM} = Q_R - Q_{LM} \tag{B.3}$$

$$S_{UM} = -S_{LM} Q_{LM} / Q_{UM} \tag{B.4}$$

$$T_{UM} = -T_{LM} Q_{LM} / Q_{UM} \tag{B.5}$$

$$Q_{LP} = -hW_p \Big(\frac{Q_R g(\beta_S S_{LP} - \beta_T T_{LP})}{\alpha} \Big)^{1/3} \tag{B.6}$$

$$S_{LP} = 0.9 S_{LM} \tag{B.7}$$

$$T_{LP} = 0.9 T_{LM} \tag{B.8}$$

$$\rho_{LP} = \rho_0 (1 + \beta_S S_{LP} - \beta_T T_{LP}) \tag{B.9}$$

$$\rho_{UM} = \rho_0 (1 + \beta_S S_{UM} - \beta_T T_{UM}) \tag{B.10}$$

B.2 Fjord Box Model: System of Equations

We now have seven equations, for the seven unknowns. To use Newton's method, we must first calculate the Jacobian for this system of equations. Defining

$$G_1(\vec{x}) = Q_{LM} + Q_{UM} - Q_R, \tag{B.11}$$

$$G_2(\vec{x}) = S_{LM}Q_{LM} + S_{UM}Q_{UM}, \tag{B.12}$$

$$G_3(\vec{x}) = T_{LM}Q_{LM} + T_{UM}Q_{UM}, \tag{B.13}$$

$$G_4(\vec{x}) = Q_{LM}S_{LM} - Q_{LP}S_{LP} + \frac{Q_{LM} - Q_{LP}}{2}(S_{LM} - S_{LP}) \tag{B.14}$$

$$+ \frac{\kappa_v A}{2dz}\Big(S_{LM} - S_{UM} + S_{LP} + \frac{S_{LP}Q_{LP}}{Q_R - Q_{LP}}\Big), \tag{B.15}$$

$$G_5(\vec{x}) = Q_{LM}T_{LM} - Q_{LP}T_{LP} + \frac{Q_{LM} - Q_{LP}}{2}(T_{LM} - T_{LP})$$

$$+ \frac{\kappa_v A}{2dz}\Big(T_{LM} - T_{UM} + T_{LP} + \frac{T_{LP}Q_{LP}}{Q_R - Q_{LP}}\Big), \tag{B.16}$$

$$G_6(\vec{x}) = Q_{LP} + hW_p\Big(\frac{Q_R g(\beta_S S_{LP} - \beta_T T_{LP})}{\alpha}\Big)^{1/3},$$

$$G_7(\vec{x}) = h(Q_{LM}\rho_{LM} - Q_{LP}\rho_{LP}) + (H+h)(Q_{UM}\rho_{UM} - Q_R\rho_R + Q_{LP}\rho_{LP}) - \tag{B.17}$$

$$- 2\kappa_v A\Big(\rho_{LM} - \rho_{UM} + \rho_{LP} - \frac{Q_R\rho_R - Q_{LP} * \rho_{LP}}{Q_R - Q_{LP}}\Big) \tag{B.18}$$

$$- \frac{Q_{LM} - Q_{LP}}{2}\Big(h(\rho_{LP} + \rho_{LM}) + (H-h)(\rho_{UM} + \frac{Q_R\rho_R - Q_{LP} * \rho_{LP}}{Q_R - Q_{LP}}\Big),$$

$$G_8(\vec{x}) = \rho_{LP} - \rho_0(1 + \beta_S S_{LP} - \beta_T T_{LP}), \tag{B.19}$$

$$G_9(\vec{x}) = \rho_{UM} - \rho_0(1 + \beta_S S_{UM} - \beta_T T_{LP}). \tag{B.20}$$

Where $\vec{x}$ is the vector of unknowns: $\vec{x} = (Q_{LM}, Q_{UM}, S_{UM}, T_{UM}, Q_{LP}, S_{LP}, T_{LP}, \rho_{LP}, \rho_{UM})$. The goal is to find $\vec{G}(\vec{x}) = \vec{0}$.

B.3 Fjord Box Model: Jacobian

The Jacobian of the FBM is

$$J = \begin{bmatrix} 1 & 1 & 0 & 0 & 0 & 0 & 0 & 0 & 0 \\ \frac{\partial G_1}{\partial x_1} & \frac{\partial G_2}{\partial x_2} & \frac{\partial G_2}{\partial x_3} & 0 & 0 & 0 & 0 & 0 & 0 \\ \frac{\partial G_3}{\partial x_1} & \frac{\partial G_3}{\partial x_2} & 0 & \frac{\partial G_3}{\partial x_4} & 0 & 0 & 0 & 0 & 0 \\ \frac{\partial G_4}{\partial x_1} & 0 & \frac{-\kappa_v * A}{2 * dz} & 0 & \frac{\partial G_4}{\partial x_5} & \frac{\partial G_4}{\partial x_6} & 0 & 0 & 0 \\ \frac{\partial G_5}{\partial x_1} & 0 & 0 & \frac{-\kappa_v * A}{2 * dz} & \frac{\partial G_5}{\partial x_5} & 0 & \frac{\partial G_5}{\partial x_7} & 0 & 0 \\ 0 & 0 & 0 & 0 & 1 & \frac{\partial G_6}{\partial x_6} & \frac{\partial G_6}{\partial x_7} & 0 & 0 \\ \frac{\partial G_7}{\partial x_1} & \frac{\partial G_7}{\partial x_2} & 0 & 0 & \frac{\partial G_7}{\partial x_5} & 0 & 0 & \frac{\partial G_7}{\partial x_8} & \frac{\partial G_7}{\partial x_9} \\ 0 & 0 & 0 & 0 & 0 & -\rho_0 \beta_S & \rho_0 \beta_T & 1 & 0 \\ 0 & 0 & -\rho_0 \beta_S & \rho_0 \beta_T & 0 & 0 & 0 & 0 & 1 \end{bmatrix}.$$

The non-constant derivatives are below. For G_2:

$$\frac{\partial G_2}{\partial x_1} = S_{LM}, \tag{B.21}$$

$$\frac{\partial G_2}{\partial x_2} = S_{UM}, \tag{B.22}$$

$$\frac{\partial G_2}{\partial x_3} = Q_{UM}. \tag{B.23}$$

For G_3:

$$\frac{\partial G_3}{\partial x_1} = T_{LM}, \tag{B.24}$$

$$\frac{\partial G_3}{\partial x_2} = T_{UM}, \tag{B.25}$$

$$\frac{\partial G_3}{\partial x_4} = Q_{UM}. \tag{B.26}$$

For G_4:

$$\frac{\partial G_4}{\partial x_1} = S_{LM} + 1/2(S_{LM} - S_{LP}) = 1/2(S_{LM} - S_{LP}), \tag{B.27}$$

$$\frac{\partial G_4}{\partial x_5} = -S_{LP} - 1/2(S_{LM} + S_{LP}) + \frac{\kappa_v A}{2dz}\frac{S_{LP}Q_R}{(Q_R - Q_{LP})^2}, \tag{B.28}$$

$$\frac{\partial G_4}{\partial x_6} = -Q_{LP} - 1/2(Q_{LP} - Q_{LM}) + \frac{\kappa_v A}{2dz}(1 + Q_{LP}/(Q_R - Q_{LP})). \tag{B.29}$$

For G_5:

$$\frac{\partial G_5}{\partial x_1} = T_{LM} + 1/2(T_{LM} - T_{LP}) = 1/2(T_{LM} - T_{LP}), \tag{B.30}$$

$$\frac{\partial G_5}{\partial x_5} = -T_{LP} - 1/2(T_{LM} + T_{LP}) + \frac{\kappa_v A}{2dz}\frac{T_{LP}Q_R}{(Q_R - Q_{LP})^2}, \tag{B.31}$$

$$\frac{\partial G_5}{\partial x_7} = -Q_{LP} - 1/2(Q_{LP} - Q_{LM}) + \frac{\kappa_v A}{2dz}(1 + Q_{LP}/(Q_R - Q_{LP})). \tag{B.32}$$

For G_6:

$$\frac{\partial G_6}{\partial x_6} = \frac{W_p h \alpha^{2/3} g Q_R \beta_S}{3}\Big(gQ_R(\beta_S S_{LP} - \beta_T T_{LP})\Big)^{-2/3} \tag{B.33}$$

$$\frac{\partial G_6}{\partial x_7} = \frac{-W_p h \alpha^{2/3} g Q_R \beta_T}{3}\Big(gQ_R(\beta_S S_{LP} - \beta_T T_{LP})\Big)^{-2/3} \tag{B.34}$$

For G_7:

$$\frac{\partial G_7}{\partial x_1} = h\rho_{LM} - 1/2[h(\rho_{LP}+\rho_{LM}) + (H-h)(\rho_{UM} + (Q_R\rho_R - Q_{LP}\rho_{LP})/(Q_R - Q_{LP}))], \tag{B.35}$$

$$\frac{\partial G_7}{\partial x_2} = (H+h)\rho_{UM}, \tag{B.36}$$

$$\begin{aligned}\frac{\partial G_7}{\partial x_5} &= H\rho_{LP} + 2\kappa_v A(Q_R * (\rho_R - \rho_{LP})/(Q_R - Q_{LP})^2) \\ &\quad - 1/2\frac{(H-h)Q_R(Q_{LM}-Q_{LP})(\rho_R - \rho_{LP})}{(Q_R - Q_{LP})^2} \\ &\quad + 1/2(h(\rho_{LP}+\rho_{UM}) + (H-h)(\rho_{UM} + (Q_R\rho_R - Q_{LP}\rho_{LP})/(Q_R - Q_{LP}))),\end{aligned} \tag{B.37}$$

$$\begin{aligned}\frac{\partial G_7}{\partial x_8} &= HQ_{LP} + 2\kappa_v A(1 + Q_{LP}/(Q_R - Q_{LP})) \\ &\quad - 1/2(Q_{LM} - Q_{LP}) * (h - (H-h)Q_{LP}/(Q_R - Q_{LP})),\end{aligned} \tag{B.38}$$

$$\frac{\partial G_7}{\partial x_9} = (H+h)Q_{UM} + 2\kappa_v A - 1/2(H-h)(Q_{LM} - Q_{LP}). \tag{B.39}$$

Bibliography

Almansi, M., Haine, T., Gelderloos, R., and Pickart, R. (2020). Evolution of Denmark Strait overflow cyclones and their relationship to overflow surges. *Geophysical Research Letters*, 47(4):e2019GL086759.

Almansi, M., Haine, T. W., Pickart, R. S., Magaldi, M. G., Gelderloos, R., and Mastropole, D. (2017). High-frequency variability in the circulation and hydrography of the Denmark Strait overflow from a high-resolution numerical model. *Journal of Physical Oceanography*, 47(12):2999–3013.

Appen, W.-J. v., Mastropole, D., Pickart, R. S., Valdimarsson, H., Jónsson, S., and Girton, J. B. (2017). On the nature of the mesoscale variability in Denmark Strait. *Journal of Physical Oceanography*, 47(3):567–582.

Appen, W.-J. v., Pickart, R. S., Brink, K. H., and Haine, T. W. (2014). Water column structure and statistics of Denmark Strait Overflow Water cyclones. *Deep Sea Research Part I: Oceanographic Research Papers*, 84:110–126.

Arzeno-Soltero, I. B., Giddings, S. N., Pawlak, G., McClean, J. L., Wang, H., Rainville, L., and Lee, C. M. (2021). Generation of low-latitude seamount-trapped waves: A case study of the Seychelles Plateau. *Journal of Geophysical Research: Oceans*, 126(8):e2021JC017234.

Bacon, S. and Fofonoff, N. (1996). Oceanic heat flux calculation. *J. Atmos. Ocean. Tech.*, 13:1327–1329.

Bacon, S., Marshall, A., Holliday, N. P., Aksenov, Y., and Dye, S. R. (2014). Seasonal variability of the East Greenland coastal current. *Journal of Geophysical Research: Oceans*, 119(6):3967–3987.

Bakker, P., Schmittner, A., Lenaerts, J., Abe-Ouchi, A., Bi, D., van den Broeke, M., Chan, W.-L., Hu, A., Beadling, R., Marsland, S., et al. (2016). Fate of the atlantic meridional overturning circulation: Strong decline under continued warming and greenland melting. *Geophysical Research Letters*, 43(23):12–252.

Bamber, J., Tedstone, A., King, M., Howat, I., Enderlin, E., Van Den Broeke, M., and Noel, B.

(2018). Land ice freshwater budget of the arctic and north atlantic oceans: 1. data, methods, and results. *Journal of Geophysical Research: Oceans*, 123(3):1827–1837.

Beaird, N., Straneo, F., and Jenkins, W. (2015). Spreading of greenland meltwaters in the ocean revealed by noble gases. *Geophysical Research Letters*, 42(18):7705–7713.

Beaird, N., Straneo, F., and Jenkins, W. (2017). Characteristics of meltwater export from jakobshavn isbræ and ilulissat icefjord. *Annals of Glaciology*, 58(74):107–117.

Beaird, N. L., Straneo, F., and Jenkins, W. (2018a). Export of strongly diluted greenland meltwater from a major glacial fjord. *Geophysical Research Letters*, 45(9):4163–4170.

Beaird, N. L., Straneo, F., and Jenkins, W. (2018b). Export of strongly diluted greenland meltwater from a major glacial fjord. *Geophysical Research Letters*, 45(9):4163–4170.

Benn, D. I., Cowton, T., Todd, J., and Luckman, A. (2017). Glacier calving in Greenland. *Current Climate Change Reports*, 3(4):282–290.

Berk, J., Drijfhout, S., and Hazeleger, W. (2021). Circulation adjustment in the arctic and atlantic in response to greenland and antarctic mass loss. *Climate Dynamics*, 57(7):1689–1707.

Bleck, R. (2002). An oceanic general circulation model framed in hybrid isopycnic-Cartesian coordinates. *Ocean modelling*, 4(1):55–88.

Böning, C. W., Behrens, E., Biastoch, A., Getzlaff, K., and Bamber, J. L. (2016). Emerging impact of Greenland meltwater on deepwater formation in the North Atlantic Ocean. *Nature Geoscience*, 9(7):523–527.

Böning, C. W. and Budich, R. G. (1992). Eddy dynamics in a primitive equation model: Sensitivity to horizontal resolution and friction. *Journal of Physical Oceanography*, 22(4):361–381.

Bracco, A., Pedlosky, J., and Pickart, R. S. (2008). Eddy formation near the west coast of greenland. *Journal of Physical Oceanography*, 38(9):1992–2002.

Brandt, P., Schott, F. A., Funk, A., and Martins, C. S. (2004). Seasonal to interannual variability of the eddy field in the Labrador Sea from satellite altimetry. *Journal of Geophysical Research: Oceans*, 109(C2).

Brunnabend, S.-E. and Dijkstra, H. A. (2017). Asymmetric response of the atlantic meridional ocean circulation to freshwater anomalies in a strongly-eddying global ocean model. *Tellus A: Dynamic Meteorology and Oceanography*, 69(1):1299283.

Carroll, D., Sutherland, D. A., Hudson, B., Moon, T., Catania, G. A., Shroyer, E. L., Nash, J. D.,

Bartholomaus, T. C., Felikson, D., Stearns, L. A., et al. (2016). The impact of glacier geometry on meltwater plume structure and submarine melt in greenland fjords. *Geophysical Research Letters*, 43(18):9739–9748.

Carroll, D., Sutherland, D. A., Shroyer, E. L., Nash, J. D., Catania, G. A., and Stearns, L. A. (2017). Subglacial discharge-driven renewal of tidewater glacier fjords. *Journal of Geophysical Research: Oceans*, 122(8):6611–6629.

Castelao, R. M., Luo, H., Oliver, H., Rennermalm, A. K., Tedesco, M., Bracco, A., Yager, P. L., Mote, T. L., and Medeiros, P. M. (2019). Controls on the transport of meltwater from the southern greenland ice sheet in the labrador sea. *Journal of Geophysical Research: Oceans*, 124(6):3551–3560.

Castillo-Trujillo, A. C., Arzeno-Soltero, I. B., Giddings, S. N., Pawlak, G., McClean, J., and Rainville, L. (2021). Observations and modeling of ocean circulation in the Seychelles Plateau Region. *Journal of Geophysical Research: Oceans*, 126(2):e2020JC016593.

Castro de la Guardia, L., Hu, X., and Myers, P. G. (2015). Potential positive feedback between Greenland Ice Sheet melt and Baffin Bay heat content on the west Greenland shelf. *Geophysical Research Letters*, 42(12):4922–4930.

Chafik, L. and Rossby, T. (2019). Volume, heat, and freshwater divergences in the subpolar north atlantic suggest the nordic seas as key to the state of the meridional overturning circulation. *Geophysical Research Letters*, 46(9):4799–4808.

Chanut, J., Barnier, B., Large, W., Debreu, L., Penduff, T., Molines, J. M., and Mathiot, P. (2008). Mesoscale eddies in the labrador sea and their contribution to convection and restratification. *Journal of Physical Oceanography*, 38(8):1617–1643.

Chassignet, E., Lee, C. M., Bamber, J. L., Curry, B., Dukhovskoy, D. S., Timmermans, M.-L., Platov, G., Myers, P. G., Proshutinsky, A., Hu, X., et al. (2016). Greenland freshwater pathways in the sub-arctic seas from model experiments with passive tracers.

Chassignet, E. P., Hurlburt, H. E., Metzger, E. J., Smedstad, O. M., Cummings, J., Halliwell, G. R., Bleck, R., Baraille, R., , Wallcraft, A., Lozano, C., Tolman, H. L., Srinivasan, A., Hankin, S., Cornillon, P., Weisberg, R., BArth, A., He, R., Werner, F., and Wilkin, J. (2009). Global ocean prediction with the HYbrid Coordinate Ocean Model (HYCOM). *Oceanography*, 22(2):64–75.

Chassignet, E. P., Hurlburt, H. E., Smedstad, O. M., Halliwell, G. R., Hogan, P. J., Wallcraft, A. J., Baraille, R., and Bleck, R. (2007). The HYCOM (HYbrid Coordinate Ocean Model) data assimilative system. *Journal of Marine Systems*, 65(1-4):60–83.

Chassignet, E. P., Smith, L. T., Halliwell, G. R., and Bleck, R. (2003). North atlantic simulations

with the HYbrid Coordinate Ocean Model (HYCOM): Impact of the vertical coordinate choice, reference density, and thermobaricity. *Journal of Physical Oceanography*, 33:2504–2526.

Christoffersen, P., Mugford, R., Heywood, K., Joughin, I., Dowdeswell, J., Syvitski, J., Luckman, A., and Benham, T. (2011). Warming of waters in an East Greenland fjord prior to glacier retreat: mechanisms and connection to large-scale atmospheric conditions. *The Cryosphere*, 5(3):701–714.

Christoffersen, P., O'Leary, M., Van Angelen, J. H., and Van Den Broeke, M. (2012). Partitioning effects from ocean and atmosphere on the calving stability of Kangerdlugssuaq Glacier, East Greenland. *Annals of Glaciology*, 53(60):249–256.

Chu, V. W. (2014). Greenland ice sheet hydrology: A review. *Progress in Physical Geography*, 38(1):19–54.

Cowton, T., Slater, D., Sole, A., Goldberg, D., and Nienow, P. (2015). Modeling the impact of glacial runoff on fjord circulation and submarine melt rate using a new subgrid-scale parameterization for glacial plumes. *Journal of Geophysical Research: Oceans*, 120(2):796–812.

Cowton, T., Sole, A., Nienow, P., Slater, D., Wilton, D., and Hanna, E. (2016). Controls on the transport of oceanic heat to kangerdlugssuaq glacier, east greenland. *Journal of Glaciology*, 62(236):1167–1180.

Cuny, J., Rhines, P. B., Schott, F., and Lazier, J. (2005). Convection above the labrador continental slope. *Journal of Physical Oceanography*, 35(4):489–511.

Curry, B., Lee, C. M., Petrie, B., Moritz, R. E., and Kwok, R. (2014). Multiyear volume, liquid freshwater, and sea ice transports through Davis Strait, 2004–10. *Journal of Physical Oceanography*, 44(4):1244–1266.

Dai, A. and Trenberth, K. E. (2002). Estimates of freshwater discharge from continents: Latitudinal and seasonal variations. *Journal of hydrometeorology*, 3(6):660–687.

Davison, B., Cowton, T., Cottier, F. R., and Sole, A. (2020). Iceberg melting substantially modifies oceanic heat flux towards a major greenlandic tidewater glacier. *Nature communications*, 11(1):1–13.

De Jong, M., Bower, A., and Furey, H. (2014). Two years of observations of warm-core anticyclones in the labrador sea and their seasonal cycle in heat and salt stratification. *Journal of Physical Oceanography*, 44(2):427–444.

Desbruyères, D. G., Mercier, H., Maze, G., and Daniault, N. (2019). Surface predictor of overturning circulation and heat content change in the subpolar north atlantic. *Ocean Science*,

15(3):809–817.

Dukhovskoy, D. S., Chassignet, E. P., Hogan, P. J., Metzger, E. J., Posey, P., Smedstad, O. M., Stefanova, L. B., and Wallcraft, A. J. (2016a). Current state and recent changes in the Arctic Ocean from the HYCOM-NCODA global ocean and sea ice prediction system. In *AGU Fall Meeting Abstracts*, volume 2016, pages GC23H–07.

Dukhovskoy, D. S., Myers, P. G., Platov, G., Timmermans, M.-L., Curry, B., Proshutinsky, A., Bamber, J. L., Chassignet, E., Hu, X., Lee, C. M., et al. (2016b). Greenland freshwater pathways in the sub-Arctic seas from model experiments with passive tracers. *Journal of Geophysical Research: Oceans*, 121(1):877–907.

Dukhovskoy, D. S., Yashayaev, I., Chassignet, E. P., Meyers, P. G., Platov, G., and Proshutinsky, A. (2021). Time scales of the Greenland Freshwater Anomaly in the Subpolar North Atlantic. *Journal of Climate*.

Dukhovskoy, D. S., Yashayaev, I., Proshutinsky, A., Bamber, J., Bashmachnikov, I., Chassignet, E., Lee, C., and Tedstone, A. (2019). Role of Greenland freshwater anomaly in the recent freshening of the subpolar North Atlantic. *Journal of Geophysical Research: Oceans*, 124(5):3333–3360.

Dukowicz, J. K. and Smith, R. D. (1994). Implicit free-surface method for the Bryan-Cox-Semtner ocean model. *Journal of Geophysical Research: Oceans*, 99(C4):7991–8014.

Eden, C. and Böning, C. (2002). Sources of eddy kinetic energy in the labrador sea. *Journal of Physical Oceanography*, 32(12):3346–3363.

Ellison, T. and Turner, J. (1959). Turbulent entrainment in stratified flows. *Journal of Fluid Mechanics*, 6(3):423–448.

Enderlin, E. M., Hamilton, G. S., Straneo, F., and Sutherland, D. A. (2016). Iceberg meltwater fluxes dominate the freshwater budget in greenland's iceberg-congested glacial fjords. *Geophysical Research Letters*, 43(21):11–287.

Foukal, N. P., Gelderloos, R., and Pickart, R. S. (2020). A continuous pathway for fresh water along the East Greenland shelf. *Science advances*, 6(43):eabc4254.

Fraser, N. J. and Inall, M. E. (2018). Influence of barrier wind forcing on heat delivery toward the Greenland Ice Sheet. *Journal of Geophysical Research: Oceans*, 123(4):2513–2538.

Fratantoni, D. M. (2001). North Atlantic surface circulation during the 1990's observed with satellite-tracked drifters. *Journal of Geophysical Research: Oceans*, 106(C10):22067–22093.

Fried, M., Carroll, D., Catania, G., Sutherland, D., Stearns, L. A., Shroyer, E., and Nash, J. (2019).

Distinct frontal ablation processes drive heterogeneous submarine terminus morphology. *Geophysical Research Letters*, 46(21):12083–12091.

Funk, A., Brandt, P., and Fischer, T. (2009). Eddy diffusivities estimated from observations in the labrador sea. *Journal of Geophysical Research: Oceans*, 114(C4).

Furevik, T. and Nilsen, J. E. Ø. (2005). *Large-scale atmospheric circulation variability and its impacts on the Nordic Seas ocean climate—A review*, pages 105–136. American Geophysical Union (AGU).

Gaube, P., J. McGillicuddy Jr, D., and Moulin, A. J. (2019). Mesoscale eddies modulate mixed layer depth globally. *Geophysical Research Letters*, 46(3):1505–1512.

Gelderloos, R., Haine, T. W., and Almansi, M. (2021). Coastal trapped waves and other subinertial variability along the Southeast Greenland Coast in a realistic numerical simulation. *Journal of Physical Oceanography*, 51(3):861–877.

Gelderloos, R., Haine, T. W., Koszalka, I. M., and Magaldi, M. G. (2017). Seasonal variability in warm-water inflow toward Kangerdlugssuaq Fjord. *Journal of Physical Oceanography*, 47(7):1685–1699.

Gierz, P., Lohmann, G., and Wei, W. (2015). Response of atlantic overturning to future warming in a coupled atmosphere-ocean-ice sheet model. *Geophysical Research Letters*, 42(16):6811–6818.

Gill, A. E. (1982). *Atmosphere-ocean dynamics*, volume 30. Academic press.

Gillard, L. C., Hu, X., Myers, P. G., and Bamber, J. L. (2016). Meltwater pathways from marine terminating glaciers of the greenland ice sheet. *Geophysical Research Letters*, 43(20):10–873.

Gillard, L. C., Hu, X., Myers, P. G., Ribergaard, M. H., and Lee, C. M. (2020). Drivers for Atlantic-origin waters abutting Greenland. *The Cryosphere*, 14(8):2729–2753.

Gou, R., Feucher, C., Pennelly, C., and Myers, P. G. (2021). Seasonal cycle of the coastal west greenland current system between cape farewell and cape desolation from a very high-resolution numerical model. *Journal of Geophysical Research: Oceans*, 126(5):e2020JC017017.

Griffies, S. M., Danabasoglu, G., Durack, P. J., Adcroft, A. J., Balaji, V., Böning, C. W., Chassignet, E. P., Curchitser, E., Deshayes, J., Drange, H., et al. (2016). Omip contribution to cmip6: Experimental and diagnostic protocol for the physical component of the ocean model intercomparison project. *Geoscientific Model Development*, 9(9):3231–3296.

Grist, J. P., Josey, S. A., Boehme, L., Meredith, M. P., Laidre, K. L., Heide-Jørgensen, M. P.,

Kovacs, K. M., Lydersen, C., Davidson, F. J., Stenson, G. B., et al. (2014). Seasonal variability of the warm Atlantic water layer in the vicinity of the Greenland shelf break. *Geophysical Research Letters*, 41(23):8530–8537.

Grivault, N., Hu, X., and Myers, P. G. (2017). Evolution of Baffin Bay water masses and transports in a numerical sensitivity experiment under enhanced Greenland Melt. *Atmosphere-Ocean*, 55(3):169–194.

Hallberg, R. (2013). Using a resolution function to regulate parameterizations of oceanic mesoscale eddy effects. *Ocean Modelling*, 72:92–103.

Hammond, M. D. and Jones, D. C. (2016). Freshwater flux from ice sheet melting and iceberg calving in the southern ocean. *Geoscience Data Journal*, 3(2):60–62.

Hanna, E., Jones, J. M., Cappelen, J., Mernild, S. H., Wood, L., Steffen, K., and Huybrechts, P. (2013). The influence of North Atlantic atmospheric and oceanic forcing effects on 1900–2010 Greenland summer climate and ice melt/runoff. *International Journal of Climatology*, 33(4):862–880.

Hátún, H., Eriksen, C. C., and Rhines, P. B. (2007). Buoyant eddies entering the labrador sea observed with gliders and altimetry. *Journal of Physical Oceanography*, 37(12):2838–2854.

Håvik, L., Våge, K., Pickart, R. S., Harden, B., Appen, W.-J. v., Jónsson, S., and Østerhus, S. (2017). Structure and variability of the shelfbreak East Greenland Current north of Denmark Strait. *Journal of Physical Oceanography*, 47(10):2631–2646.

Hecht, M., Veneziani, M., Weijer, W., Kravitz, B., Burrows, S., Comeau, D., Hunke, E., Jeffery, N., Urrego-Blanco, J., Wang, H., et al. (2019). E3smv0-hilat: A modified climate system model targeted for the study of high-latitude processes. *Journal of Advances in Modeling Earth Systems*, 11(8):2814–2843.

Holland, D. M., Thomas, R. H., De Young, B., Ribergaard, M. H., and Lyberth, B. (2008). Acceleration of Jakobshavn Isbrae triggered by warm subsurface ocean waters. *Nature geoscience*, 1(10):659.

Holliday, N. P., Bacon, S., Cunningham, S. A., Gary, S. F., Karstensen, J., King, B. A., Li, F., and McDonagh, E. L. (2018). Subpolar North Atlantic overturning and gyre-scale circulation in the summers of 2014 and 2016. *Journal of Geophysical Research: Oceans*, 123(7):4538–4559.

Holte, J. and Talley, L. (2009). A new algorithm for finding mixed layer depths with applications to argo data and subantarctic mode water formation. *Journal of Atmospheric and Oceanic Technology*, 26(9):1920–1939.

Howat, I. M., Smith, B. E., Joughin, I., and Scambos, T. A. (2008). Rates of southeast Greenland

ice volume loss from combined ICESat and ASTER observations. *Geophysical Research Letters*, 35(17).

Hunke, E. C., Lipscomb, W. H., Turner, A. K., Jeffery, N., and Elliott, S. (2010). CICE: the Los Alamos Sea Ice Model Documentation and Software User's Manual Version 4.1 LA-CC-06-012. *T-3 Fluid Dynamics Group, Los Alamos National Laboratory*, 675.

Hurrell, J. W., Holland, M. M., Gent, P. R., Ghan, S., Kay, J. E., Kushner, P. J., Lamarque, J.-F., Large, W. G., Lawrence, D., Lindsay, K., et al. (2013). The Community Earth System Model: A framework for collaborative research. *Bulletin of the American Meteorological Society*, 94(9):1339–1360.

Jackson, L. C. and Wood, R. A. (2018). Timescales of amoc decline in response to fresh water forcing. *Climate Dynamics*, 51(4):1333–1350.

Jackson, R., Shroyer, E., Nash, J., Sutherland, D., Carroll, D., Fried, M., Catania, G., Bartholomaus, T., and Stearns, L. (2017). Near-glacier surveying of a subglacial discharge plume: Implications for plume parameterizations. *Geophysical Research Letters*, 44(13):6886–6894.

Jackson, R. H., Lentz, S. J., and Straneo, F. (2018). The dynamics of shelf forcing in Greenlandic fjords. *Journal of Physical Oceanography*, (2018).

Jackson, R. H. and Straneo, F. (2016). Heat, salt, and freshwater budgets for a glacial fjord in Greenland. *Journal of Physical Oceanography*, 46(9):2735–2768.

Jackson, R. H., Straneo, F., and Sutherland, D. A. (2014). Externally forced fluctuations in ocean temperature at Greenland glaciers in non-summer months. *Nature Geoscience*, 7(7):503.

Jenkins, A. (2011). Convection-driven melting near the grounding lines of ice shelves and tidewater glaciers. *Journal of Physical Oceanography*, 41(12):2279–2294.

Jones, H. and Marshall, J. (1997). Restratification after deep convection. *Journal of Physical Oceanography*, 27(10):2276–2287.

Jones, P. and Lazier, J. (2007). Hudson 18HU19930617 cruise data from the 1993 cruises, CARINA Data Set. http://cdiac.ornl.gov/ftp/oceans/CARINA/Hudson/18HU93019/. Carbon Dioxide Information Analysis Center, Oak Ridge National Laboratory, US Department of Energy, Oak Ridge, Tennessee. doi: 10.3334/CDIAC/otg.CARINA$_1$8*HU*19930617.

Katsman, C. A., Spall, M. A., and Pickart, R. S. (2004). Boundary current eddies and their role in the restratification of the labrador sea. *Journal of Physical Oceanography*, 34(9):1967–1983.

Large, W. G., Danabasoglu, G., Doney, S. C., and McWilliams, J. C. (1997). Sensitivity to surface forcing and boundary layer mixing in a global ocean model: Annual-mean climatology.

Journal of Physical Oceanography, 27(11):2418–2447.

Large, W. G. and Yeager, S. (2009). The global climatology of an interannually varying air–sea flux data set. *Climate dynamics*, 33(2-3):341–364.

Le Bras, I. A.-A., Straneo, F., Holte, J., and Holliday, N. P. (2018). Seasonality of freshwater in the east Greenland current system from 2014 to 2016. *Journal of Geophysical Research: Oceans*, 123(12):8828–8848.

Lenaerts, J. T., Le Bars, D., Van Kampenhout, L., Vizcaino, M., Enderlin, E. M., and Van Den Broeke, M. R. (2015). Representing greenland ice sheet freshwater fluxes in climate models. *Geophysical Research Letters*, 42(15):6373–6381.

Lilly, J. M., Rhines, P. B., Schott, F., Lavender, K., Lazier, J., Send, U., and D'Asaro, E. (2003). Observations of the labrador sea eddy field. *Progress in Oceanography*, 59(1):75–176.

Lohmann, K., Jungclaus, J. H., Matei, D., Mignot, J., Menary, M., Langehaug, H., Ba, J., Gao, Y., Otterå, O. H., Park, W., et al. (2014). The role of subpolar deep water formation and nordic seas overflows in simulated multidecadal variability of the atlantic meridional overturning circulation. *Ocean Science*, 10(2):227–241.

Lozier, M. S., Li, F., Bacon, S., Bahr, F., Bower, A. S., Cunningham, S., de Jong, M. F., de Steur, L., deYoung, B., Fischer, J., et al. (2019). A sea change in our view of overturning in the subpolar north atlantic. *Science*, 363(6426):516–521.

Luo, H., Castelao, R. M., Rennermalm, A. K., Tedesco, M., Bracco, A., Yager, P. L., and Mote, T. L. (2016). Oceanic transport of surface meltwater from the southern greenland ice sheet. *Nature Geoscience*, 9(7):528–532.

Luthcke, S. B., Zwally, H. J., Abdalati, W., Rowlands, D. D., Ray, R. D., Nerem, R. S., Lemoine, F. G., McCarthy, J. J., and Chinn, D. S. (2006). Recent Greenland ice mass loss by drainage system from satellite gravity observations. *Science*, 314(5803):1286–1289.

MacCready, P., Geyer, W. R., et al. (2010). Advances in estuarine physics. *Annual Review of Marine Science*, 2(1):35–58.

Majumder, S., Castelao, R. M., and Amos, C. M. (2021). Freshwater variability and transport in the labrador sea from in situ and satellite observations. *Journal of Geophysical Research: Oceans*, 126(4):e2020JC016751.

Marshall, J., Adcroft, A., Hill, C., Perelman, L., and Heisey, C. (1997a). A finite-volume, incompressible navier stokes model for studies of the ocean on parallel computers. *Journal of Geophysical Research: Oceans*, 102(C3):5753–5766.

Marshall, J., Hill, C., Perelman, L., and Adcroft, A. (1997b). Hydrostatic, quasi-hydrostatic, and nonhydrostatic ocean modeling. *Journal of Geophysical Research: Oceans*, 102(C3):5733–5752.

Marshall, J. and Schott, F. (1999). Open-ocean convection: Observations, theory, and models. *Reviews of geophysics*, 37(1):1–64.

Martínez-Moreno, J., Hogg, A. M., England, M. H., Constantinou, N. C., Kiss, A. E., and Morrison, A. K. (2021). Global changes in oceanic mesoscale currents over the satellite altimetry record. *Nature Climate Change*, 11(5):397–403.

McClean, J. L., Bader, D. C., Bryan, F. O., Maltrud, M. E., Dennis, J. M., Mirin, A. A., Jones, P. W., Kim, Y. Y., Ivanova, D. P., Vertenstein, M., Boyle, J. S., Jacob, R. L., Norton, N., Craig, A., and Worley, P. H. (2011). A prototype two-decade fully-coupled fine-resolution CCSM simulation. *Ocean Modelling*, 39(1-2):10–30.

McClean, J. L., Bader, D. C., Maltrud, M. E., Evans, K. J., Taylor, M., Tang, Q., Ivanova, D., Veneziani, C., Ritchie, J., Branstetter, M. L., and Mahajan, S. (2018). High-resolution fully-coupled ACME v0.1 approximate present day transient climate simulations. Ocean Sciences Meeting 2018, 12-16/February, Portland/OR. Abstract ID: OM44C-2143.

Meehl, G. A., Stocker, T. F., Collins, W. D., Friedlingstein, P., Gaye, T., Gregory, J. M., Kitoh, A., Knutti, R., Murphy, J. M., Noda, A., Raper, S. C. B., Watterson, I. G., Weaver, A. J., and Zhao, Z. C. (2007). Global climate projections. In Solomon, S., Qin, D., Manning, M., Chen, Z., Marquis, M., Averyt, K., Tignor, M., and Miller, H. L., editors, *Climate Change 2007: The Physical Science Basis. Contribution of Working Group I to the Fourth Assessment Report of the Intergovernmental Panel on Climate Change*. Cambridge University Press, Cambridge, United Kingdom and New York, NY, USA.

Metzger, E. J., Smedstad, O. M., Thoppil, P. G., Hurlburt, H. E., Cummings, J. A., Wallcraft, A. J., Zamudio, L., Franklin, D. S., Posey, P. G., Phelps, M. W., et al. (2014). US Navy operational global ocean and Arctic ice prediction systems. *Oceanography*, 27(3):32–43.

Millan, R., Rignot, E., Mouginot, J., Wood, M., Bjørk, A. A., and Morlighem, M. (2018). Vulnerability of Southeast Greenland glaciers to warm Atlantic water from Operation IceBridge and Ocean Melting Greenland data. *Geophysical Research Letters*.

Moon, T., Sutherland, D., Carroll, D., Felikson, D., Kehrl, L., and Straneo, F. (2018). Subsurface iceberg melt key to greenland fjord freshwater budget. *Nature Geoscience*, 11(1):49.

Moritz, M., Jochumsen, K., North, R. P., Quadfasel, D., and Valdimarsson, H. (2019). Mesoscale eddies observed at the Denmark Strait sill. *Journal of Geophysical Research: Oceans*, 124(11):7947–7961.

Morlighem, M., Williams, C. N., Rignot, E., An, L., Arndt, J. E., Bamber, J. L., Catania, G., Chauché, N., Dowdeswell, J. A., Dorschel, B., et al. (2017). BedMachine v3: Complete bed topography and ocean bathymetry mapping of Greenland from multibeam echo sounding combined with mass conservation. *Geophysical research letters*, 44(21).

Morton, B., Taylor, G. I., and Turner, J. S. (1956). Turbulent gravitational convection from maintained and instantaneous sources. *Proceedings of the Royal Society of London. Series A. Mathematical and Physical Sciences*, 234(1196):1–23.

Mouginot, J., Rignot, E., Bjørk, A. A., van den Broeke, M., Millan, R., Morlighem, M., Noël, B., Scheuchl, B., and Wood, M. (2019). Forty-six years of Greenland Ice Sheet mass balance from 1972 to 2018. *Proceedings of the National Academy of Sciences*, page 201904242.

Muilwijk, M., Straneo, F., Slater, D. A., Smedsrud, L. H., Holte, J., Wood, M., Andresen, C. S., and Harden, B. (2022). Export of ice sheet meltwater from Upernavik Fjord, West Greenland. *Journal of Physical Oceanography*, 52(3):363–382.

Münchow, A., Schaffer, J., and Kanzow, T. (2020). Ocean circulation connecting Fram Strait to glaciers off Northeast Greenland: Mean flows, topographic Rossby waves, and their forcing. *Journal of Physical Oceanography*, 50(2):509–530.

Murray, R. J. (1996). Explicit generation of orthogonal grids for ocean models. *Journal of Computational Physics*, 126(2):251–273.

Myers, P. G., Donnelly, C., and Ribergaard, M. H. (2009). Structure and variability of the West Greenland Current in summer derived from 6 repeat standard sections. *Progress in Oceanography*, 80(1-2):93–112.

Nurser, A. and Bacon, S. (2014). The Rossby radius in the Arctic Ocean. *Ocean Science*, 10(6):967–975.

Okubo, A. (1970). Horizontal dispersion of floatable particles in the vicinity of velocity singularities such as convergences. In *Deep sea research and oceanographic abstracts*, volume 17, pages 445–454. Elsevier.

Østerhus, S., Woodgate, R., Valdimarsson, H., Turrell, B., De Steur, L., Quadfasel, D., Olsen, S. M., Moritz, M., Lee, C. M., Larsen, K. M. H., et al. (2019). Arctic Mediterranean exchanges: A consistent volume budget and trends in transports from two decades of observations. *Ocean Science*, 15(2):379–399.

Pacini, A. and Pickart, R. S. (2022). Meanders of the west greenland current near cape farewell. *Deep Sea Research Part I: Oceanographic Research Papers*, 179:103664.

Pacini, A., Pickart, R. S., Bahr, F., Torres, D. J., Ramsey, A. L., Holte, J., Karstensen, J.,

Oltmanns, M., Straneo, F., Le Bras, I. A., et al. (2020). Mean conditions and seasonality of the west greenland boundary current system near cape farewell. *Journal of Physical Oceanography*, 50(10):2849–2871.

Palóczy, A., Gille, S. T., and McClean, J. L. (2018). Oceanic heat delivery to the Antarctic Continental Shelf: Large-scale, low-frequency variability. *Journal of Geophysical Research: Oceans*, 123(11):7678–7701.

Palóczy, A., McClean, J. L., Gille, S. T., and Wang, H. (2020). The large-scale vorticity balance of the Antarctic continental margin in a fine-resolution global simulation. *Journal of Physical Oceanography*, 50(8):2173–2188.

Pattyn, F., Ritz, C., Hanna, E., Asay-Davis, X., DeConto, R., Durand, G., Favier, L., Fettweis, X., Goelzer, H., Golledge, N. R., et al. (2018). The greenland and antarctic ice sheets under 1.5 c global warming. *Nature climate change*, 8(12):1053–1061.

Peng, Q., Xie, S.-P., Wang, D., Huang, R. X., Chen, G., Shu, Y., Shi, J.-R., and Liu, W. (2022). Surface warming–induced global acceleration of upper ocean currents. *Science advances*, 8(16):eabj8394.

Pennelly, C., Hu, X., and Myers, P. G. (2019). Cross-isobath freshwater exchange within the North Atlantic subpolar gyre. *Journal of Geophysical Research: Oceans*, 124(10):6831–6853.

Pennelly, C. and Myers, P. G. (2020). Introducing LAB60: A 1/ 60° NEMO 3.6 numerical simulation of the Labrador Sea. *Geoscientific Model Development*, 13(10):4959–4975.

Petit, T., Lozier, M. S., Josey, S. A., and Cunningham, S. A. (2020). Atlantic deep water formation occurs primarily in the iceland basin and irminger sea by local buoyancy forcing. *Geophysical Research Letters*, 47(22):e2020GL091028.

Pickart, R. S., Torres, D. J., and Clarke, R. A. (2002). Hydrography of the labrador sea during active convection. *Journal of Physical Oceanography*, 32(2):428–457.

Pickart, R. S. and Watts, D. R. (1990). Deep western boundary current variability at Cape Hatteras. *Journal of Marine Research*, 48(4):765–791.

Rahmstorf, S. (1995). Bifurcations of the atlantic thermohaline circulation in response to changes in the hydrological cycle. *Nature*, 378(6553):145–149.

Rhines, P. (1970). Edge-, bottom-, and Rossby waves in a rotating stratified fluid. *Geophysical and Astrophysical Fluid Dynamics*, 1(3-4):273–302.

Rieck, J. K., Böning, C. W., and Getzlaff, K. (2019). The nature of eddy kinetic energy in the labrador sea: Different types of mesoscale eddies, their temporal variability, and impact on

deep convection. *Journal of Physical Oceanography*, 49(8):2075–2094.

Rignot, E., Fenty, I., Menemenlis, D., and Xu, Y. (2012). Spreading of warm ocean waters around Greenland as a possible cause for glacier acceleration. *Annals of Glaciology*, 53(60):257–266.

Rossby, T., Flagg, C., Chafik, L., Harden, B., and Søiland, H. (2018). A direct estimate of volume, heat, and freshwater exchange across the Greenland-Iceland-Faroe-Scotland Ridge. *Journal of Geophysical Research: Oceans*, 123(10):7139–7153.

Saenko, O. A., Dupont, F., Yang, D., Myers, P. G., Yashayaev, I., and Smith, G. C. (2014). Role of resolved and parameterized eddies in the labrador sea balance of heat and buoyancy. *Journal of Physical Oceanography*, 44(12):3008–3032.

Saha, S., Moorthi, S., Pan, H.-L., Wu, X., Wang, J., Nadiga, S., Tripp, P., Kistler, R., Woollen, J., Behringer, D., et al. (2010). The NCEP climate forecast system reanalysis. *Bulletin of the American Meteorological Society*, 91(8):1015–1058.

Saha, S., Moorthi, S., Wu, X., Wang, J., Nadiga, S., Tripp, P., Behringer, D., Hou, Y.-T., Chuang, H.-y., Iredell, M., et al. (2014). The NCEP climate forecast system version 2. *Journal of climate*, 27(6):2185–2208.

Saini, J., Stein, R., Fahl, K., Weiser, J., Hebbeln, D., Hillaire-Marcel, C., and de Vernal, A. (2020). Holocene variability in sea ice and primary productivity in the northeastern Baffin Bay. *arktos*, 6(1):55–73.

Sanchez, R., Straneo, F., and Andres, M. (2021). Using acoustic travel time to monitor the heat variability of glacial fjords. *Journal of Atmospheric and Oceanic Technology*, 38(9):1535–1550.

Schauer, U. and Beszczynska-Möller, A. (2009). Problems with estimation and interpretation of oceanic heat transport–conceptual remarks for the case of Fram Strait in the Arctic Ocean. *Ocean Science*, 5(4):487–494.

Schulze Chretien, L. M. and Frajka-Williams, E. (2018). Wind-driven transport of fresh shelf water into the upper 30 m of the Labrador Sea. *Ocean Science*, 14(5):1247–1264.

Slater, D., Carroll, D., Oliver, H., Hopwood, M., Straneo, F., Wood, M., Willis, J., and Morlighem, M. (2022). Characteristic depths, fluxes and timescales for greenland's tidewater glacier fjords from subglacial discharge-driven upwelling during summer. *Geophysical Research Letters*, page e2021GL097081.

Slater, D., Nienow, P., Cowton, T., Goldberg, D., and Sole, A. (2015). Effect of near-terminus subglacial hydrology on tidewater glacier submarine melt rates. *Geophysical Research Letters*, 42(8):2861–2868.

Slater, D., Straneo, F., Das, S., Richards, C., Wagner, T., and Nienow, P. (2018). Localized plumes drive front-wide ocean melting of a greenlandic tidewater glacier. *Geophysical Research Letters*, 45(22):12–350.

Slater, D. A., Goldberg, D. N., Nienow, P. W., and Cowton, T. R. (2016). Scalings for submarine melting at tidewater glaciers from buoyant plume theory. *Journal of Physical Oceanography*, 46(6):1839–1855.

Smith, B., Fricker, H. A., Gardner, A. S., Medley, B., Nilsson, J., Paolo, F. S., Holschuh, N., Adusumilli, S., Brunt, K., Csatho, B., Harbeck, K., Markus, T., Neumann, T., Siegfried, M. R., and Zwally, H. J. (2020). Pervasive ice sheet mass loss reflects competing ocean and atmosphere processes. *Science*.

Smith, R. and Gent, P. (2002). Reference manual for the Parallel Ocean Program (POP). *Los Alamos unclassified report LA-UR-02-2484*.

Spall, M. A. and Price, J. F. (1998). Mesoscale variability in Denmark Strait: The PV outflow hypothesis. *Journal of physical oceanography*, 28(8):1598–1623.

Steele, M., Morley, R., and Ermold, W. (2001). Phc: A global ocean hydrography with a high-quality arctic ocean. *Journal of Climate*, 14(9):2079–2087.

Stewart, A. L., Klocker, A., and Menemenlis, D. (2019). Acceleration and overturning of the antarctic slope current by winds, eddies, and tides. *Journal of Physical Oceanography*, 49(8):2043–2074.

Stouffer, R. J., Yin, J., Gregory, J., Dixon, K., Spelman, M., Hurlin, W., Weaver, A., Eby, M., Flato, G., Hasumi, H., et al. (2006). Investigating the causes of the response of the thermohaline circulation to past and future climate changes. *Journal of climate*, 19(8):1365–1387.

Straneo, F. and Cenedese, C. (2015a). The dynamics of Greenland's glacial fjords and their role in climate. *Annual Review of Marine Science*, 7:89–112.

Straneo, F. and Cenedese, C. (2015b). The dynamics of Greenland's glacial fjords and their role in climate. *Annual review of marine science*, 7:89–112.

Straneo, F., Hamilton, G. S., Stearns, L. A., and Sutherland, D. A. (2016). Connecting the greenland ice sheet and the ocean: A case study of helheim glacier and sermilik fjord. *Oceanography*, 29(4):34–45.

Straneo, F., Hamilton, G. S., Sutherland, D. A., Stearns, L. A., Davidson, F., Hammill, M. O., Stenson, G. B., and Rosing-Asvid, A. (2010). Rapid circulation of warm subtropical waters in a major glacial fjord in east greenland. *Nature Geoscience*, 3(3):182–186.

Straneo, F. and Heimbach, P. (2013). North Atlantic warming and the retreat of Greenland's outlet glaciers. *Nature*, 504(7478):36–43.

Straneo, F., Heimbach, P., Sergienko, O., Hamilton, G., Catania, G., Griffies, S., Hallberg, R., Jenkins, A., Joughin, I., Motyka, R., et al. (2013). Challenges to understanding the dynamic response of Greenland's marine terminating glaciers to oceanic and atmospheric forcing. *Bulletin of the American Meteorological Society*, 94(8):1131–1144.

Straneo, F., Kawase, M., and Pickart, R. S. (2002). Effects of wind on convection in strongly and weakly baroclinic flows with application to the labrador sea. *Journal of physical oceanography*, 32(9):2603–2618.

Straneo, F., Sutherland, D. A., Holland, D., Gladish, C., Hamilton, G. S., Johnson, H. L., Rignot, E., Xu, Y., and Koppes, M. (2012). Characteristics of ocean waters reaching Greenland's glaciers. *Annals of Glaciology*, 53(60):202–210.

Straneo, F., Sutherland, D. A., Stearns, L., Catania, G., Heimbach, P., Moon, T., Cape, M. R., Laidre, K. L., Barber, D., Rysgaard, S., et al. (2019). The case for a sustained Greenland Ice Sheet-ocean observing system (GrIOOS). *Frontiers in Marine Science*, 6:138.

Sun, Q., Whitney, M. M., Bryan, F. O., and Tseng, Y.-h. (2017). A box model for representing estuarine physical processes in Earth system models. *Ocean Modelling*, 112:139–153.

Sun, Q., Whitney, M. M., Bryan, F. O., and Tseng, Y.-h. (2019). Assessing the skill of the improved treatment of riverine freshwater in the community earth system model (cesm) relative to a new salinity climatology. *Journal of Advances in Modeling Earth Systems*, 11(5):1189–1206.

Sutherland, D. A. and Pickart, R. S. (2008). The East Greenland coastal current: Structure, variability, and forcing. *Progress in Oceanography*, 78(1):58–77.

Sutherland, D. A., Straneo, F., Stenson, G. B., Davidson, F. J., Hammill, M. O., and Rosing-Asvid, A. (2013). Atlantic water variability on the SE Greenland continental shelf and its relationship to SST and bathymetry. *Journal of Geophysical Research: Oceans*, 118(2):847–855.

Tagklis, F., Bracco, A., Ito, T., and Castelao, R. (2020). Submesoscale modulation of deep water formation in the labrador sea. *Scientific reports*, 10(1):1–13.

The IMBIE Team (2020). Mass balance of the greenland ice sheet from 1992 to 2018. *Nature*, 579(7798):233–239.

Toom, M. d., Dijkstra, H. A., Weijer, W., Hecht, M. W., Maltrud, M. E., and Van Sebille, E. (2014). Response of a strongly eddying global ocean to north atlantic freshwater perturbations. *Journal of Physical Oceanography*, 44(2):464–481.

Treasure, A. M., Roquet, F., Ansorge, I. J., Bester, M. N., Boehme, L., Bornemann, H., Charrassin, J.-B., Chevallier, D., Costa, D. P., Fedak, M. A., et al. (2017). Marine mammals exploring the oceans pole to pole: a review of the MEOP consortium. *Oceanography*, 30(2):132–138.

Trodahl, M. and Isachsen, P. E. (2018). Topographic influence on baroclinic instability and the mesoscale eddy field in the northern North Atlantic Ocean and the Nordic Seas. *Journal of Physical Oceanography*, 48(11):2593–2607.

van den Broeke, M., Bamber, J., Ettema, J., Rignot, E., Schrama, E., van de Berg, W. J., van Meijgaard, E., Velicogna, I., and Wouters, B. (2009). Partitioning recent Greenland mass loss. *Science*, 326(5955):984–986.

Wang, H., McClean, J. L., and Talley, L. D. (2021). Full vorticity budget of the Arabian Sea from a 0.1 ocean model: Sverdrup dynamics, Rossby waves, and nonlinear eddy effects. *Journal of Physical Oceanography*, 51(12):3589–3607.

Wang, H., McClean, J. L., Talley, L. D., and Yeager, S. (2018). Seasonal cycle and annual reversal of the Somali Current in an eddy-resolving global ocean model. *Journal of Geophysical Research: Oceans*, 123(9):6562–6580.

Weatherall, P., Marks, K. M., Jakobsson, M., Schmitt, T., Tani, S., Arndt, J. E., Rovere, M., Chayes, D., Ferrini, V., and Wigley, R. (2015). A new digital bathymetric model of the world's oceans. *Earth and space Science*, 2(8):331–345.

Weijer, W., Cheng, W., Drijfhout, S. S., Fedorov, A. V., Hu, A., Jackson, L. C., Liu, W., McDonagh, E., Mecking, J., and Zhang, J. (2019). Stability of the atlantic meridional overturning circulation: A review and synthesis. *Journal of Geophysical Research: Oceans*, 124(8):5336–5375.

Weijer, W., Maltrud, M., Hecht, M., Dijkstra, H., and Kliphuis, M. (2012). Response of the atlantic ocean circulation to greenland ice sheet melting in a strongly-eddying ocean model. *Geophysical Research Letters*, 39(9).

Weiss, J. (1991). The dynamics of enstrophy transfer in two-dimensional hydrodynamics. *Physica D: Nonlinear Phenomena*, 48(2-3):273–294.

Wouters, B., Chambers, D., and Schrama, E. J. O. (2008). GRACE observes small-scale mass loss in Greenland. *Geophysical Research Letters*, 35(20). L20501.

Xu, Y., Rignot, E., Fenty, I., Menemenlis, D., and Flexas, M. M. (2013). Subaqueous melting of store glacier, west greenland from three-dimensional, high-resolution numerical modeling and ocean observations. *Geophysical Research Letters*, 40(17):4648–4653.

Yashayaev, I. and Loder, J. W. (2017). Further intensification of deep convection in the labrador

sea in 2016. *Geophysical Research Letters*, 44(3):1429–1438.

Yeager, S., Castruccio, F., Chang, P., Danabasoglu, G., Maroon, E., Small, J., Wang, H., Wu, L., and Zhang, S. (2021). An outsized role for the labrador sea in the multidecadal variability of the atlantic overturning circulation. *Science advances*, 7(41):eabh3592.

Yu, L., Gao, Y., and Otterå, O. H. (2016). The sensitivity of the atlantic meridional overturning circulation to enhanced freshwater discharge along the entire, eastern and western coast of greenland. *Climate Dynamics*, 46(5):1351–1369.

Zhao, K. X., Stewart, A. L., and McWilliams, J. C. (2021). Geometric constraints on glacial fjord–shelf exchange. *Journal of Physical Oceanography*, 51(4):1223–1246.

Zhu, J., Demirov, E., Zhang, Y., and Polomska-Harlick, A. (2014). Model simulations of mesoscale eddies and deep convection in the labrador sea. *Advances in Atmospheric Sciences*, 31(4):743–754.